Chapter 2
Properties of Sapphire

2.1 Physical Properties

2.1.1 Crystal Structure and Morphology of Sapphire

Corundum crystals belong to the ditrigonal-scalenohedral class of the trigonal symmetry $D^6_{3d} - R\,\overline{3}C(L_3 3L_2 3PC)$ with symmetry elements:

- Mirror-turn axis of the sixth order (ternary inversion axis)
- Three axes of the second order normal to it
- Three symmetry planes normal to the axes of the second order and intercrossing along the axis of the highest order
- Symmetry center

There are seven simple forms (facets) in this class of symmetry. According to Bravais classification they have the following symbols: pinacoid (0001), hexagonal prisms $\{10\overline{1}0\}$ and $\{11\overline{2}0\}$, dihexagonal prism $\{hki0\}$, rhombohedron $\{h0\overline{h}l\}$, hexagonal bipyramid $\{hh2\overline{h}l\}$, and ditrigonal scalenohedron. Depending on its position with respect to the hexagonal crystallographic axes, the rhombohedron may be "positive" $\{10\overline{1}1\}$ or "negative" $\{01\overline{1}1\}$[1].

The crystal lattice of α-Al_2O_3 is formed by Al^{3+} and O^{2-} ions. If the O^{2-} anions are depicted as balls, the crystal lattice takes the form of their closest hexagonal packing (Fig. 2.1). The Al^{3+} cations are located in a crystalline field that has no symmetry center (due to crystal lattice distortions). These cations lie in the octahedral hollows between the closely packed O^{2-} ions, filling two thirds of these hollows. The octahedron hollow is surrounded by six balls. If the radius of each is taken as a unit, then the hollow contains a ball with a relative radius of 0.41. Due to the ratio of the ionic radii of O^{2-} and Al^{3+} (equal to 1.40 and 0.57 Å, respectively), the cations are located within the hollows of the anion packing. They slightly distort the lattice, but do not fall outside the stability limits of the octahedron position.

The coordination numbers for Al^{3+} and O^{2-} are 6 and 4, respectively. The three upper O^{2-} ions in the octahedron are turned about 64.3° with respect to the three lower O^{2-} ions and lie in parallel planes (Fig. 2.2a) at a distance of 2.164 Å from each other. The closest packing distortion bound up with the discrepancy between
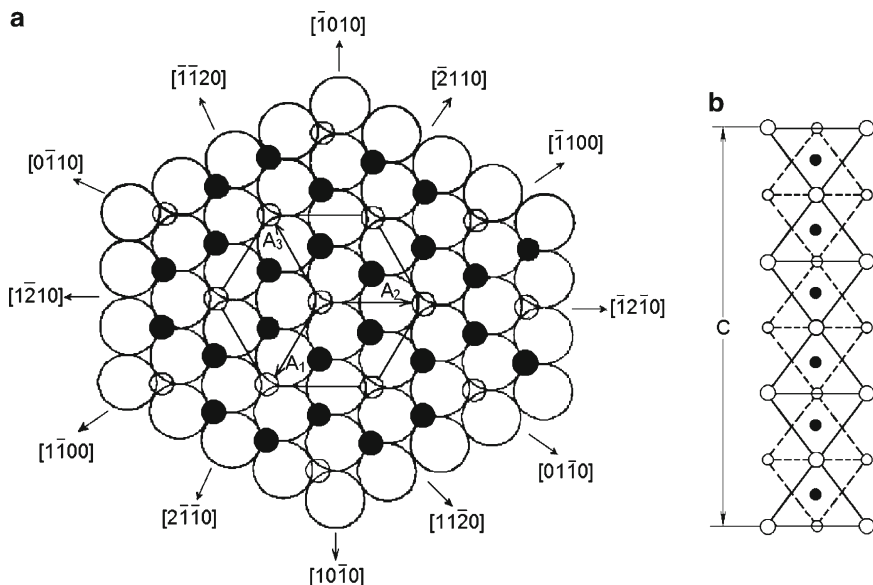
Fig. 2.1 (**a**) Schematic of the arrangement of Al³⁺ (*black circles*) and octahedral hollows (*small light circles*) between two layers of O²⁻ (*large light circles*) in the basal plane (the upper O²⁻ layer is not shown). A_1, A_2, and A_3 are $\langle 11\overline{2}0 \rangle$ translational vectors of the hexagonal sapphire cell for the basal plane.(**b**) Schematic of the packing of O²⁻ ions (*light circles*) and Al³⁺ in the direction of the axis C_3 [1]

the size of Al³⁺ and the octahedron position is manifested by the fact that the octahedron is formed by oxygen triangles of different size (Fig. 2.2c), and their rotation angle of 64.3° exceeds the value characteristic of ideal packing (60°).

The spatial arrangement of O²⁻ ions forms the so-called corundum motive. The interchanging octahedron positions of Al³⁺ are replicated in the structure in every three layers. The arrangement of the structural units along the third-order axis are replicated every 2.97 Å (the period of hexagonal lattice identity), i.e., the structure is completely replicated in six O²⁻ layers and six intermediate Al³⁺ layers (Fig. 2.2). The central pair of Al³⁺ ions (AB), three equivalent neighboring pairs (AC), three equivalent remote pairs (AD), and six equivalent most remote pairs (AE) are shown in this figure. In the direction of the *C*-axis, the three distances Al–O are equal to 1.97 Å and the other three distances are 1.87 Å (Fig. 2.2c). The Al–Al and O–O spacing are 2.65 Å and 2.52–2.87 Å, respectively.

As temperature increases, the lattice anisotropy and the bond length increase. In particular, at 2,265 K the length of the bonds Al–O increases from 1.966 to 2.024 Å and from 1.857 to 1.880 Å [2]. The coordinates of the aluminum atoms change to a greater extent in comparison with those of the oxygen atoms. The closest hexagonal packing becomes more regular [3]. The linear expansion coefficient is the highest for the bonds Al–Al ($17.5 \cdot 10^{-6}\,°C^{-1}$).

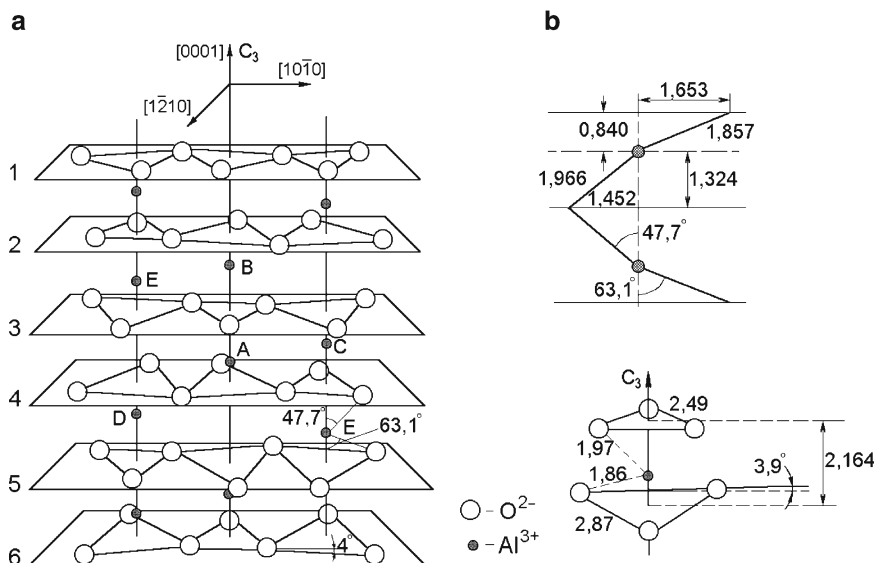**Fig. 2.2** (**a**) Schematic of the arrangement of Al^{3+} ions and O^{2-} layers (*black circles*); (**b**) the distance between Al^{3+} and O^{2-} ions; (**c**) the position of O^{2-} ions surrounding Al^{3+} ion. The planes of the triangle are perpendicular to the *C*-axis

For the ideal closest packing of rigid balls, the ratio of translation vectors is 1.63, while for sapphire it equals 1.58 (the distorted structure has a lower energy in comparison to the ideal).

If Al^{3+} is substituted by another trivalent ion, such as Cr^{3+}, structural variants are possible. In the configurations (Fig. 2.3a–c) chromium is incorporated in the lattice (a) by substituting Al^{3+} next to the anionic vacancy; (b) by substituting Al^{3+} in the regular lattice; and (c) by substituting Al^{3+} next to the cationic vacancy. In the configuration (Fig. 2.3d) Cr^{3+} occupies the position of the cationic vacancy. These configurations are not equivalent from the energetic viewpoint. In position (a) the bond of Cr^{3+} with the lattice is weaker than that of Al^{3+} in the regular lattice (b). The bond with the lattice of the ion Al^{3+} next to the cationic vacancy (c) is stronger than the one in position (b). The configuration (d) leads to diminution of the concentration of the vacancies present in the crystal for charge compensation. This configuration is preferable only at high chromium concentrations.

The structure with the spatial symmetry group $D_{3d}^6 - R3C$ can be considered to be a slightly distorted closest hexagonal packing of oxygen ions. In the crystal lattice of sapphire, two structural elementary cells — hexagonal (Fig. 2.4) and rhombohedral (Fig. 2.5) — can be distinguished. The bonding between them is shown in Fig. 2.6 [1]. The morphological and structural rhombohedral elementary cells are presented here. The morphological rhombohedral cell along C_3 axis is twice as small as the structural one. The rhombohedral angle of the morphological rhombohedral cell is 85°42 2/3′, whereas that of the structural rhombohedral cell is 55°17′. The rhombohedron vertices are located on the structural vacancies. The base of the
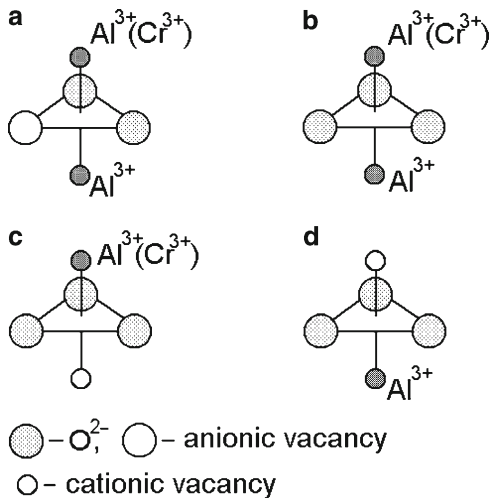
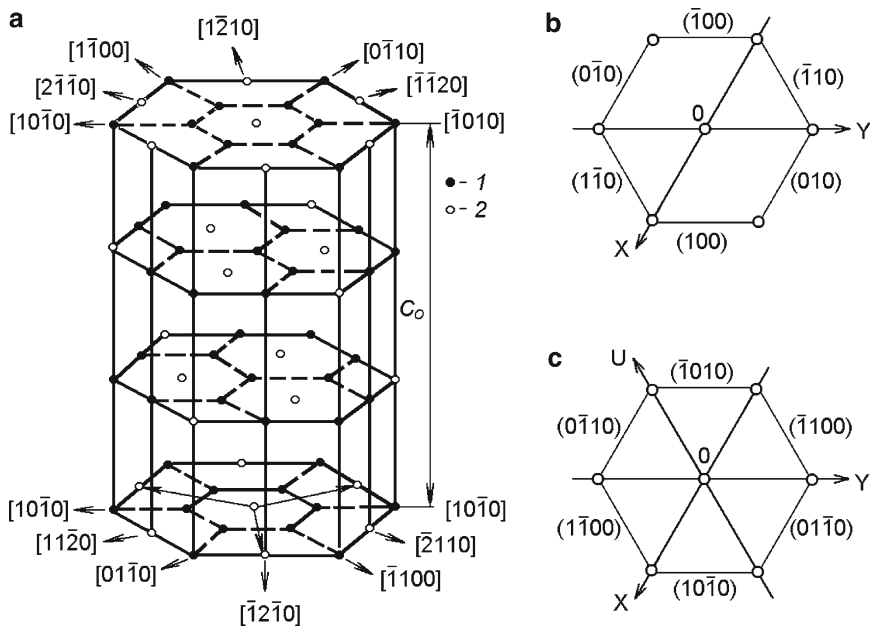**Fig. 2.3 a–d** Variants on the substitution of aluminum ions by chromium in the sapphire lattice

Fig. 2.4 (a) Hexagonal cell. (*1*) Aluminum ions; (*2*) octahedral hollows. Indexing of the hexagonal cell facets in a three-axis (**b**) and four-axis (**c**) coordinate system
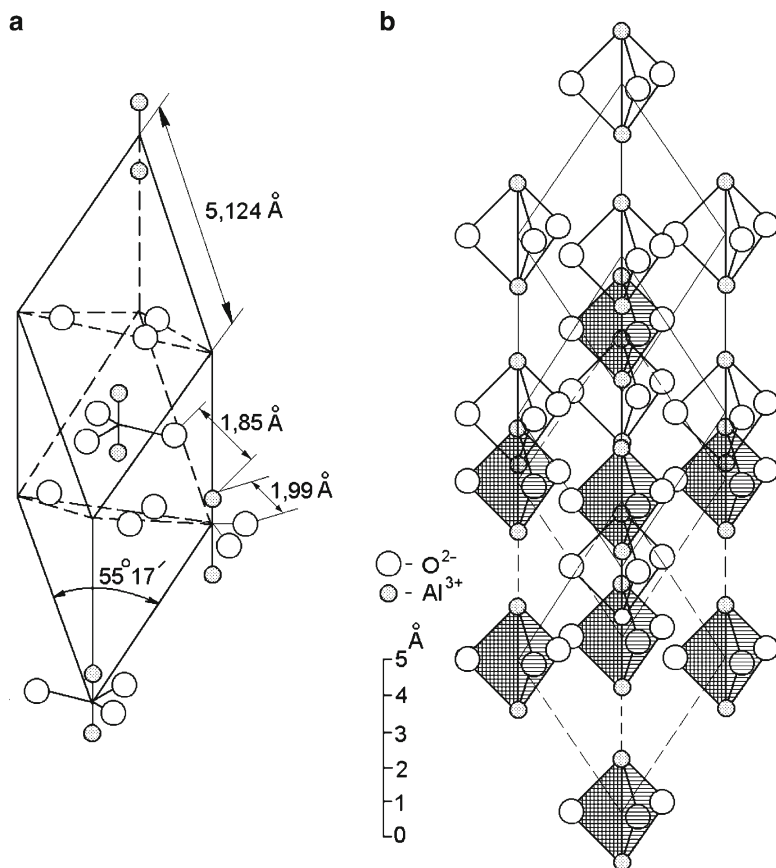
Fig. 2.5 (**a**) Scheme of the rhombohedral elementary cell $\alpha = 55°17'$; (**b**) structural and morphological (*shaded*) rhombohedral elementary cells

structural rhombohedral cell is a group of two molecules centered with respect to the vertex (Fig. 2.5). The coordinates of the ions of this cell are shown in Table 2.34 in the Appendix.

The structure of sapphire also can be depicted by means of coordination polyhedrons. In this scheme, the structural elements are shown not as balls but as polyhedrons formed by straight lines connecting the centers of the anions which surround the cations. The polyhedron vertices touch one another at the centers of the anions. The quantity of the vertices of such a polyhedron is equal to the coordination number of the cation, and the set of polyhedrons presents the mutual location of the cations. The layers formed by the oxygen octahedrons are superimposed one over another in such a way that in the octahedron columns extending along the C-axis two filled octahedrons interchange with the unfilled one [4]. The paired octahedrons make a screw axis, which characterizes the corundum motive of the packing along the axis C (Fig. 2.7b). The "pure view" of the corundum motive is shown in Fig. 2.7e.

Fig. 2.6 The bonding between the hexagonal and rhombohedral elementary cells: (*1*) octahedral hollows; (*2*) aluminum ions

$C_{str.}$

$\circ$ 1
$\bullet$ 2

$C_{morf.}$

A3
A2
A1

$[\bar{1}2\bar{1}0]$ y

$[2\bar{1}\bar{1}0]$ x
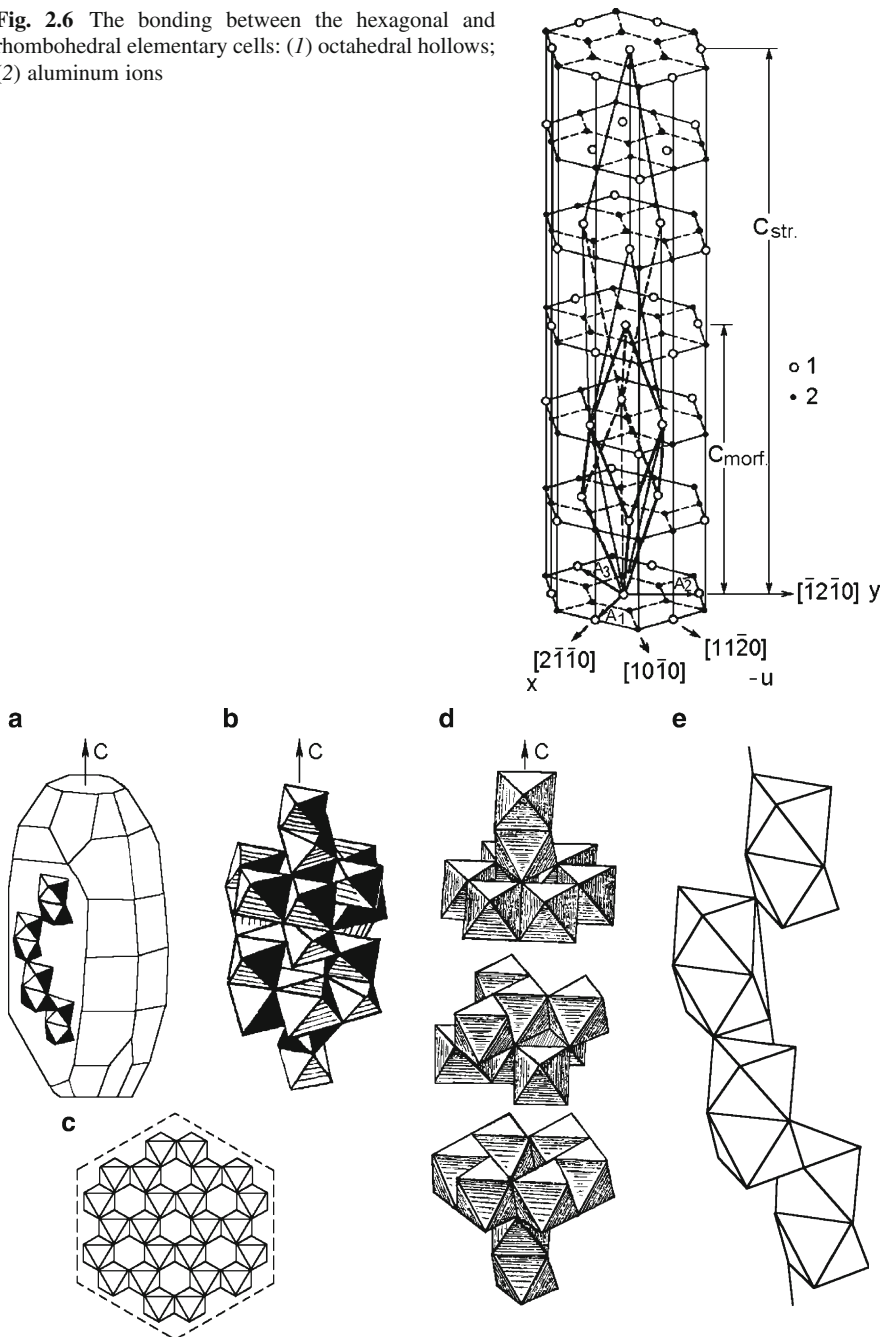$[10\bar{1}0]$
$[11\bar{2}0]$ -u

Fig. 2.7 Arrangement of octahedrons in the planes (**a**) parallel and (**c**) perpendicular to the axis *C*; (**b**) the motive of the sapphire structure: screw axis composed of paired octahedrons; (**c**) elementary rhombohedron composed of octahedrons; (**d**) the same rhombohedron in "disassembled" form; (**e**) the "pure view" of the corundum motive

Lattice parameters, or hexagonal lattice constants $a = b$ and c, the interplanar distances are given by the equation

$$d_{hkl} = 1/[(4/3\alpha^2)(h^2 + k^2 + hk) + (1 + 1/c^2)l^2]^{1/2} \qquad (2.1)$$

The values of the interplanar distances are presented in Table 2.35.

The lattice parameters increase with increasing temperature. At 295.65 K $a = 4.759213$ Å, $c = 12.991586$ Å [5], and the ratio $c/a = 2.729776$ far exceeds that of a crystal with ideal hexagonal packing $(\sqrt{8/3} \sim 1.633)$. Precise measurements of the temperature dependence of the lattice parameters within 4.5–374 K temperature range (Fig. 2.8, Table 2.36) were carried out using ^{57}Fe Mössbauer radiation [6]. The lattice parameters at high temperatures are presented in Table 2.37.

The parameters of the rhombohedral lattice are shown in Fig. 2.5. The rhombohedral angle equal to 55°17′ is larger than that in the ideal rhombohedron (53°17′) due to the electrostatic interaction of the cations with the anions, which decreases the distance between the oxygen layers. At the isomorphic substitution ^{16}O → ^{18}O the length of the bond Al–^{18}O diminishes. The unit cell parameters and the rhombohedron angle also decrease.

Influence of vacancies on the state of the lattice. Electrical neutrality of the lattice is provided by two Al^{3+} (V_{Al}^{3-}) and three O^{2-}(V_{O}^{2+}) stoichiometric vacancies. The energy of formation of Schottky defects (E_{Sh}) is $E_{\mathrm{Sh}} = 20.5$ or 4.1 eV per defect, as obtained from the expression characterizing the energy of activation for oxygen

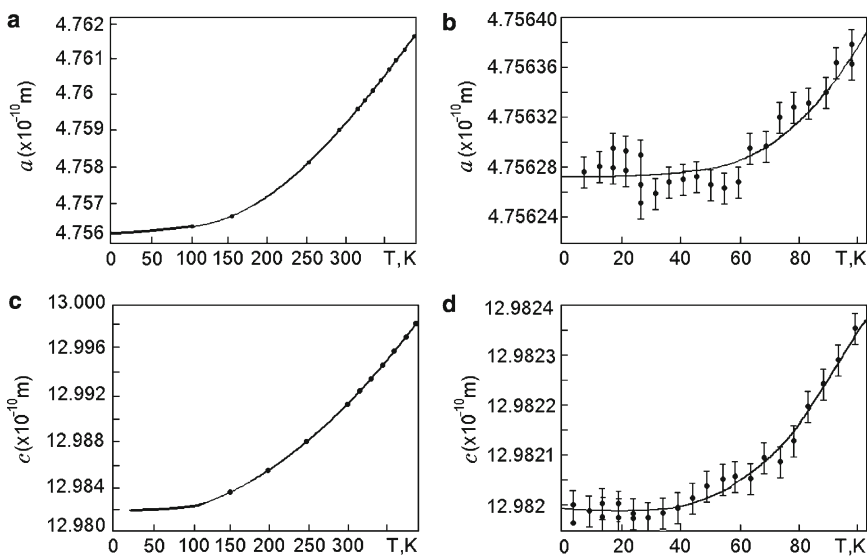**Fig. 2.8** Sapphire lattice parameters in the 4.5–374 K temperature range (**a,c**) and more detailed measurements at temperatures below 100 K (**b,d**)[5, 6]
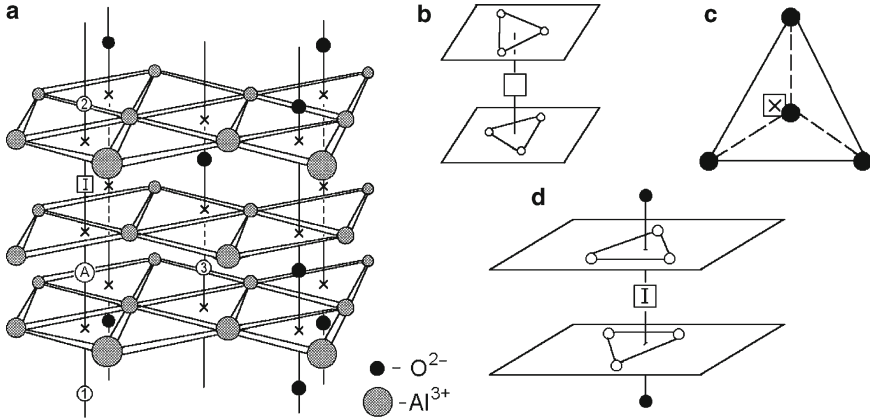
Fig. 2.9   (**a**) Positions of vacancies and interstitial ions (*I*) in the hexagonal α-Al$_2$O$_3$ lattice; (×) the places of intersection of the lines where the ions Al^{3+} are located, with the planes in which O^{2-} ions lie; (□) V_{Al}^{3-} position; (⊠) V_O^{2+} position; (⊡) the interstitial ion; (**b**) the surroundings of a V_{Al}^{3-} vacancy; (**c**) the closest surrounding of a V_O^{2+} vacancy; (**d**) the position of the interstitial ion (⊡) in the octahedral bend

diffusion $E_d = 1/5E_{Sh} + E_M$, where $E_M = 2.5$ eV is the energy of oxygen ion migration [7]. The most probable positions of point structure defects are shown in Fig. 2.9b. The vacancy V_{Al}^{3-} is situated between two groups composed of three O^{2-} ions, at a distance of 1.86 and 1.97 Å from the planes in which O^{2-} lie (Fig. 2.9). The vacancy V_O^{2+} is located within an approximately tetrahedral surrounding of Al^{3+} ions at a distance of 1.86 Å from two Al^{3+} ions and 1.97 Å from the other two Al^{3+} ions. The interstitial ion is located between the groups of Al^{3+} ions at a distance of 1.92 and 1.98 Å.

Simulation of sapphire lattice dynamics with vacancies in different charge states makes it possible to obtain data on the frequencies of resonant oscillations induced by the defects, the values of ion charges ($Z_O = -1.98|e|$, $Z_{Al} = 2.97|e|$), and the bonding constants ($k_O = 73.07$ eV/Å^2, $k_{Al} = 192.49$ eV/Å^2)[8]. Using the numerical parameters of interatomic potential and a cluster containing 1,000 atoms, the total density of the phonon states is calculated in theoretically perfect sapphire (Fig. 2.10), which is in good agreement with the corresponding experimental values [9].

Vacancies influence the oscillation spectra of sapphire (Table 2.1). Therefore, the local density of phonons in crystals containing vacancies differs from that of the perfect crystal. The localization of electron density in the center of a vacancy is of the order of 90% for (*F$^+$*) centers and 80% for *F* centers in the ground state [10, 11]. The appearance of vacancies in sapphire is accompanied by resonance oscillations at 5.7 and 22.5 THz (Fig. 2.11). The calculated total density of phonon states for all the atoms of a spherical region with a radius of 2.7 Å in the vicinity of oxygen atom (comprising four Al^{3+} and four O^{2-} ions) in nonstoichiometric sapphire is shown in Fig. 2.12.

G(ν), a.u.
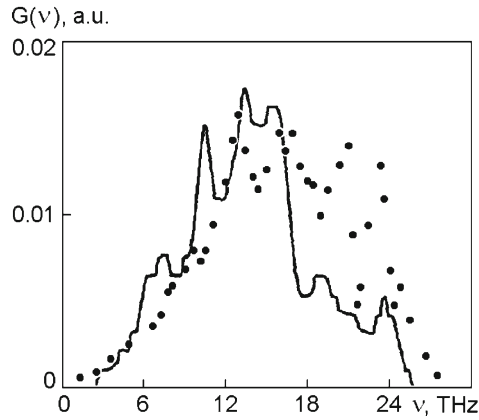
Fig. 2.10 Calculated total density of phonon states in theoretically perfect α-Al₂O₃ crystals. The points denote the experimental values

Table 2.1 Frequencies of localized oscillations induced by defects on the ions nearest to them in the sapphire lattice [8]

Defect	Ion	Distance from defect (Å)	Frequency (THz)		
			X	Y	Z
Anionic vacancy	Al(1)	2.12	5.7; 22.5	6.0; 22.5	5.7; 22.0
	Al(2)	2.24	5.4	8.4	6.6
F^+ center	Al(1)	1.97		3.0; 9.6	8.2
	Al(2)	2.07		2.0; 7.8; 14.0	3.3;11.7
F center	Al(1)	1.89		8.2; 12.0	14.7
	Al(2)	2.02	16.0	14.0	13.0

Fig. 2.11 Local density of phonons in the direction Z in the Al³⁺ ion position (*1*) nearest to the O²⁻ ion in the perfect sapphire crystal and (*2*) nearest to the anionic vacancy

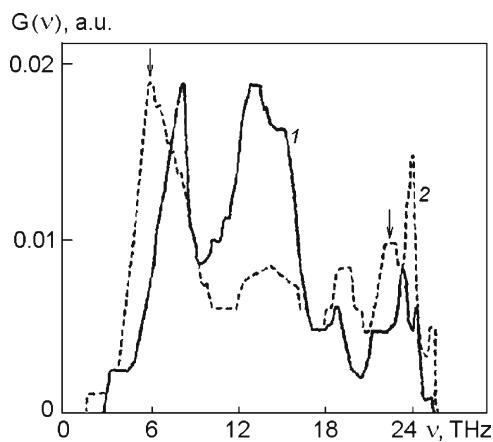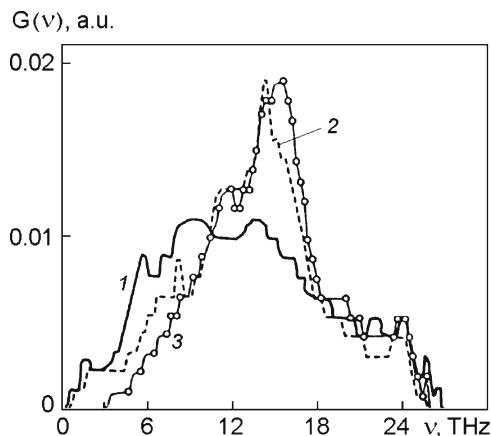**Fig. 2.12**   Total density of phonon states for the atoms located in (*1*) a spherical region of radius 2.7 Å surrounding the anionic vacancy, (*2*) F^+ center, and (*3*) F center

It has been noted [8] that the changes in the oscillation spectra are explained on the basis of effective interaction of a vacancy with its nearest surrounding, which increases the total density of phonon states in the low-frequency region of the spectrum. The coulomb interaction is partly compensated by F^+ centers and the effective interaction increases. When two electrons are captured by the center, the coulomb part is completely restored. This by far increases the effective interaction and shifts the density of states located in the region below 10 THz, to the high-frequency region of the spectrum.

Ionic bond energy influences a number of physiochemical properties of the crystal. For example, the quantity of free bonds per unit of surface area is an approximate measure of surface energy. Bonding in $\alpha\text{-}Al_2O_3$ is mainly ionic, with the share of covalent bonds at ~20%. The large quantity of partly covalent bonds that emanate from each atom of the lattice is a probable cause of the mechanical properties of sapphire. The contribution to the lattice bond energy is made by electrostatic interactions, polarization, repulsion, and Van der Waals forces, with the experimental value of total contributions from these forces at 156.7 eV [12]. Polarization energy arises in the lattice due to the appearance of electric fields bound to lattice defects. The largest contribution belongs to the forces of electrostatic interaction (the calculated value is 189.1 eV), the individual contributions of different forces to the potential ionic energy is presented in Table 2.38. Proceeding from these data, one can calculate the energy necessary for shifting an ion from a lattice site to an octahedron interstitial. Presented below are the calculated values of the energy of formation for vacancies and interstitial atoms in an inelastic, non-polarized lattice in [7]:

Al³⁺ vacancy	9.1 eV
Interstitial Al³⁺	10.8 eV
O²⁻ vacancy	3.5 eV
Interstitial O²⁻	10.5 eV
Five pairs of Schottky defects	5.7 eV
	4.1 eV (Experimental value)
Al-Frenkel pair	10.0 eV
O-Frenkel pair	7.0 eV

The calculated migration energy of V_{Al}^{3-} from the position A (Fig. 2.9a) to the position 1 (i.e., the place of localization of V_{Al}^{3-} displaced into the center of the triangle formed by O^{2-} ions) is 3.8 eV [7]. For the displacement to the positions 2 and 3 there are required energies of 6.6 and 3.8 eV, respectively. The vacancies V_O^{2+} are more mobile in comparison with V_{Al}^{3-} and the interstitial ions, and they can migrate in the planes of the O^{2-} ion locations. The calculated value of the migration energy of V_O^{2+} in the basal plane equal to 2.9 eV [7] is in good agreement with the experimental value (2.5 eV) obtained while measuring the coefficient of oxygen diffusion.

A layer with a content of V_O^{2+} higher than that in the crystal bulk (where V_{Al}^{3-} increases the value of energy per defect) may be formed near the crystal surface where the conditions of electrical neutrality are not so strict. At elevated temperatures, splitting of basal and prismatic dislocations in the process of skipping leads to the formation of packing defects. The energy of such defects (stacking fault energy) is essentially the same for different crystallographic planes at 0.15–0.35 J/m² [13].

The main parameters that characterize the lattice of sapphire are given in Table 2.39.

The electronic energy structure of sapphire is typical of that for ionic crystals. Its valence band is formed mainly by the 2p states of oxygen and has a width of 13 eV. The conduction band bottom is formed by the 3s states of aluminum. According to experimental data, the width of the forbidden band is 9.5 eV. It has been shown [14] that the plane (0001) has two unoccupied surface zones in the forbidden band that are located at 2 and 8 eV below the conduction band.

In addition to considering the lattice parameters and nature of the atomic bonds, in the process of epitaxial growth on sapphire one must take into account the electronic structure of the crystallographic planes, which is defined by the type of ions located on the crystal surface. Even parallel chips may end in different ions (Fig. 2.13a) [14].

The planes of the cross section A end in Al and O layers and of the cross section C end in two equivalent Al layers, etc. The densities of charges and their distribution in different cross sections have been calculated [14]. The distribution of charge density around the ions, with a minimum and a maximum of 0.005 and 0.050 e/a^3, respectively, is shown in Fig. 2.13b. The energy of chipping in different cross sections is estimated by studying the surface bonds of the last layer and several previous layers.

The electronic structure of sapphire is responsible for the existence of excitons with an absorption maximum in the region of 9.0–9.25 eV at 300 K.
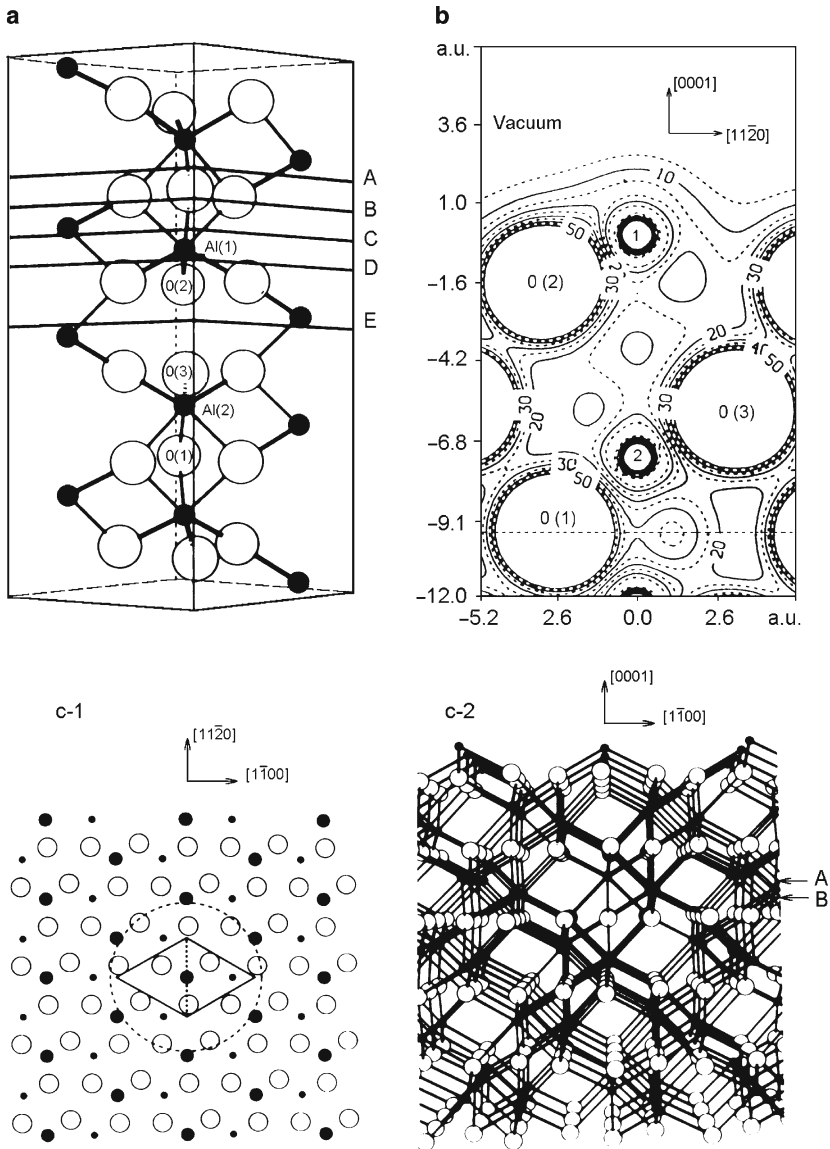
Fig. 2.13 (**a**) Cleavages in different (A–E) cross sections of the sapphire lattice parallel to the plane (0001); (**b**) distribution of the charge density around the ions shown in (**a**). (***c–1***), (***c–2***) the plane (0001), the top view of a block formed by three atomic layers Al–O–Al; O denotes oxygen ions; • and ● are aluminum ions of the upper and lower layers, respectively. Al_2O_3 cell is shown as a rhombohedron, the dashed circle marks the boundary of a cluster

Cleavage in sapphire arises at the intersections of a pair of parallel nets formed by anions. Nets with like charges reduce attractive forces. The larger the distance between the nets, the more vividly the cleavage manifests itself. In a perfect crystal

the plane of chipping must pass between these nets. In the basal plane with inter-changing O–Al–Al–O–Al–O layers there are no conditions for cleavage, whereas in the plane (10$\bar{1}$1)with interchanging O–O–Al–O–Al–O–O—O–Al–O–Al–O layers the bonds between the layers O–O located at a distance of 1.06 Å are weakened.

Sapphire does not have such a vivid cleavage as diamond and other crystals. For a long period of time, sapphire was considered to exhibit no cleavage at all. Theoretically, it has nine cleavage planes. Six planes are parallel to the facets {11$\bar{2}$0}and {10$\bar{1}$1}, and to the *C*-axis; three planes are parallel to the facets {10$\bar{1}$1} and inclined to the *C*-axis at an angle of 33°, the normal vectors to them make an angle of 57° with the *C*-axis. Crystals with a small quantity of dislocations and which do not contain blocks may have perfect cleavage in the plane of the morpho-logical rhombohedron {10$\bar{1}$1}. However, when block-containing and stressed crys-tals grown by the Verneuil method are chipped along the prismatic planes, mirror chips with steps of several atomic parameters are often observed (Fig. 2.14). To achieve more desirable chipping of these crystals, the direction of the *C*-axis is set at an angle 57° to the crystal growth axis at the location of the prism and rhombo-hedron planes, as shown in Fig. 2.14c [15].

The energy required for destruction along the plane {10$\bar{1}$1}is 6 J/m^2, whereas for the basal plane the corresponding value is more than 40 J/m^2 [16]. Shown by the estimation of the surface energy of the planes, considered to be defined by the quantity of free bonds per unit of surface, the minimum quantity of such bonds corresponds to the plane (10$\bar{1}$1)[17].

Slip systems. Nonlinearity of thermal fields leads to plastic deformation of the crystal realized mainly through slipping. Three active slip systems (Table 2.2) and their arrangement with respect to the growth direction make a contribution to the orientation dependence of tangential stresses [18].

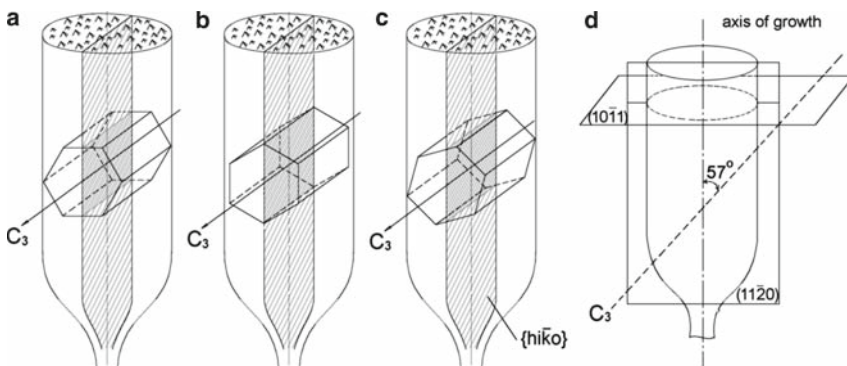**Fig. 2.14** Location of the symmetry elements and the plane of chipping in the crystals grown by the Verneuil method: (**a**) chip along the plane (11$\bar{2}$0); (**b**) chip along the plane (10$\bar{1}$0), (**c**) chip along the prism (*hik̄*0). The plane of chipping is shaded. (**d**) The location of the planes (11$\bar{2}$0) and (10$\bar{1}$1) with respect to the growth axis and to the *C*-axis for optimization of chipping

Table 2.2 Possible slip systems in sapphire

Type of slip system	Slip plane	Slip direction	Number of equivalent systems
Basal 1	c (0001)	$\langle 1\bar{2}10 \rangle$	3
Basal 2	c (0001)	$\langle 10\bar{1}0 \rangle$	3
Prismatic 1	$a(1\bar{2}10)$	$\langle 10\bar{1}0 \rangle$	3
Prismatic 2	$m(10\bar{1}0)$	$\langle 1\bar{2}10 \rangle$	3
Prismatic with inclined slip direction	$a(1\bar{2}10)$	$\langle 10\bar{1}2 \rangle$	6
Rhombohedral	$r\{10\bar{1}1\}$	$\langle 10\bar{1}2 \rangle$	3
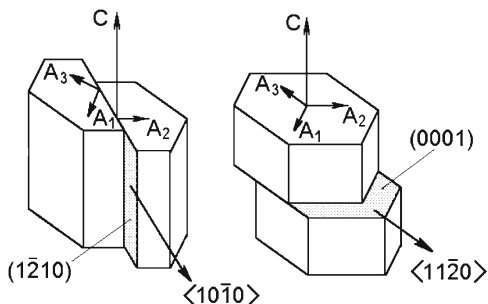
Fig. 2.15 Schematic of prismatic and basal slip systems in sapphire

In the 570–1,170 K range, only easy local slip along the prism planes is observed [19]. The plane of the easiest slip is (0001), with basal slip predominating in the direction (1120). This is observed in sapphire at $T > 970$–1,170 K, when basal dislocations become mobile. Prismatic slip occurs at $T > 1,470$ K (or, according to some data [20], at $T > 2,270$ K). At 1,470–1,670 K the activation energy is 3.8 ± 0.2 eV [21]. The value of basal slip depends on the temperature and the load. The theoretically estimated "ease" of possible slip systems was found to diminish in the following sequence: $(0001)\langle 11\bar{2}0 \rangle$, $(0001)\langle 10\bar{1}0 \rangle$, $\{10\bar{1}0\}\langle 11\bar{2}0 \rangle$, $\{11\bar{2}0\}\langle 10\bar{1}0 \rangle$, $\{10\bar{1}0\}\langle 01\bar{1}2 \rangle$, $\{11\bar{2}1\}\langle 10\bar{1}0 \rangle$, $\{22\bar{4}3\}\langle 10\bar{1}0 \rangle$.

The action of the first five systems was revealed experimentally [19, 20, 22]. The first two systems are shown schematically in Fig. 2.15. At extension of whiskers grown along the C-axis, slip on the planes $\{\bar{4}223\}$ in the direction (01$\bar{1}$0) was established from the orientation of slip traces [23].

Sapphire undergoes deformation under conditions of applied loads P. For plastic deformation, real shearing stresses, τ_c, which act in the given slip system, are important:

$$\tau_c = mP, \tag{2.2}$$

where m is the Schmid-factor (orientation factor); $m = \cos l \cdot \cos c$; l is the angle between the direction of slip and the direction of deformation, c is the angle between

the normal axis to the slip plane and the direction of deformation. At $c = l$ the factor m has its maximum value equal to 0.5. In this case the direction of slip lies in the plane which passes through the axis of deformation and the normal axis to the slip plane. Using four-point bend and indentation test data from $1.5 \times 3 \times 25$ mm³ plates (at 1,270 K, 0.5 h, 15 s), the Schmid factor was calculated for several planes and directions of slip (Table 2.3) [24].

The experimental values of shearing stresses at 2,270 K obtained during the growth of sapphire ribbons are $\tau_{cr} = 1$ MPa for the basal slip system and $\tau_{cr} = 10$ MPa for the prismatic [25]. The latter system works only in ribbons in which the deviation of the facet (0001) from the surface does not exceed 3°. At larger deviations the basal system — with the easiest slip (removal of stresses) — starts working. Therefore, in thin basal ribbons only the prismatic system acts; the basal system corresponds to thick ribbons (with a thickness exceeding 5 mm). Chromium impurities which strengthen the crystal increase the onset temperature of slip.

During the growth of sapphire by the Stepanov method in the direction of the C-axis, prismatic and rhombohedron slip systems manifest themselves. As calculations show [19], in these crystals basal slip takes place only during the growth in a direction different from $\langle 0001 \rangle$ (Fig. 2.16).

Anisotropy of thermoelastic stresses is bound to that of the lattice and with the acting slip systems. The relationship between temperature nonlinearity in sapphire tapes and the vertical component of thermoelastic stresses σ_{zz} is shown in Fig. 2.17 [22]. The first upper magnitudes correspond to σ_{zz} for the ribbon obtained upon the action of the $\{10\bar{1}0\}\langle 2\bar{1}\bar{1}0 \rangle$ slip system, the second upper magnitudes relate to the case of the action of the system $\{\bar{1}101\}\langle \bar{1}10\bar{2} \rangle$. These systems give the maximum and the minimum values of σ_{zz}. The lower magnitudes are the calculated values of σ_{zz} in the isotropic approximation. The factor of anisotropy for these orientations is 1.28 and 0.65, respectively.

Twinning may arise in sapphire upon cooling or deformation. Plastic deformation which causes twinning occurs at $T < 1,770$ K, a temperature lower in comparison with translational slip, and manifests itself to a temperature of 79 K. Twins in sapphire are defined as the regions limited by plane-parallel coherent boundaries or

Table 2.3 Schmid-factor for the plane (A) $(11\bar{2}3)$ and the loading direction $\langle \bar{2}111 \rangle$ and (B) $(11\bar{2}0)$ and the loading direction $\langle \bar{8}80\bar{5} \rangle$

Slip plane	Slip direction	Schmid-factor
(A)		
(0001)	$1/3\langle 2\bar{1}\bar{1}0 \rangle$	0.5
(0001)	$1/3\langle \bar{1}2\bar{1}0 \rangle$	0.25
(0001)	$1/3\langle \bar{1}\bar{1}20 \rangle$	0.25
(B)		
(0001)	$1/3\langle \bar{2}110 \rangle$	0.43
(0001)	$1/3\langle 1\bar{2}10 \rangle$	0.43
(0001)	$1/3\langle 11\bar{2}0 \rangle$	0.25
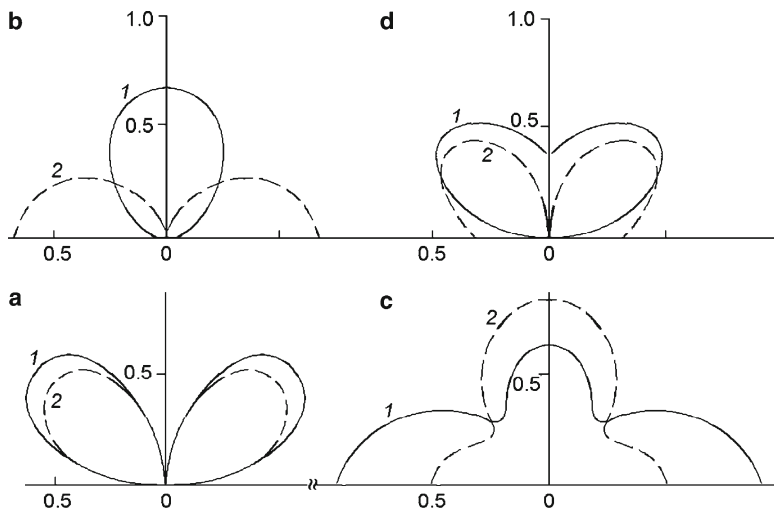
Fig. 2.16 Orientation dependences of tangential stresses (in rel. units) (*1*) in the middle part of a sapphire tube and (*2*) in the vicinity of the crystallization front. Slip systems: (**a**) (0001) $\langle 1\bar{2}10 \rangle$; (**b**) $\{1\bar{2}10\}\langle 10\bar{1}0 \rangle$; (**c**) $\{10\bar{1}1\}\langle 10\bar{1}2 \rangle$; (**d**) $\{1\bar{2}10\}\langle 10\bar{1}2 \rangle$

Fig. 2.17 The second derivative of temperature along the length of sapphire ribbon and the distribution of stresses at the action of different slip systems
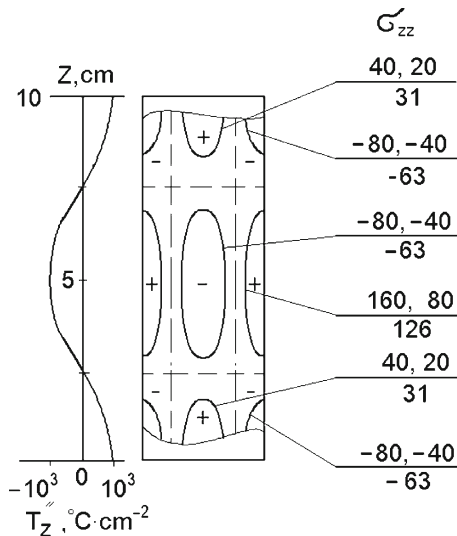
wedges with noncoherent boundaries. Geometric characteristics of a twin may be visualized proceeding from the scheme of twinning ellipsoids (Fig. 2.18) [26]. As a result of twinning along the plane passing through the center of the circle, the cross section of the circle above this plane transforms into an ellipse. The ellipse and the circle intersect at two points. In the planes K_1 and K_2 perpendicular to the circular

Fig. 2.18 Twinning ellipsoid
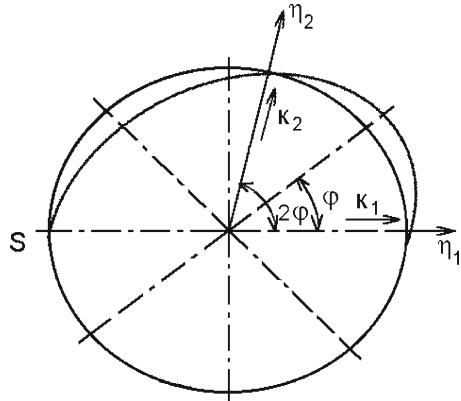
plane and passing through these points, the positions of the crystal structure units before and after twinning coincide. The plane K_1 coincides with the twinning plane and contains the direction of shearing (twinning) η_1. The plane K_2 contains the direction η_2 and makes the angle 2φ with the twinning plane. The value of the angle is defined by the specific shear $s = 2/tg\, 2\varphi$.

In sapphire there are mainly reflection twins and turn twins with the elements of twinning:

$K_1\, \{10\bar{1}1\};\ \eta_1;\ \langle 10\,\bar{1}2 \rangle;\ K_2\, \{10\bar{1}2\};\ \eta_2 < \{\bar{2}021\};\ s = 0{,}635a$

$K_1\, \{0001\};\ \eta_1;\ \langle 1\bar{2}10 \rangle;\ K_2\, \{\bar{2}021\};\ \eta_2 < \{\bar{2}021\};\ s = 0{,}202a$

Twinning in the planes $\{10\bar{1}1\}$ is characterized by a lesser specific shear and is observed even at cryogenic temperatures. The formation of a twin at compression along the C-axis (Fig. 2.19) shows shear along the rhombohedronal plane [27, 28]. The twin boundary is slightly terraced (Fig. 2.19b), with the interval between the individual terraces ~0.7 μm [29].

Joint twins are observed in crystals grown from the solution. The joints shown in Fig. 2.20 are reflection twins with a $\{10\bar{1}1\}$ twinning plane and 64°52′ twin disorientation.

Microtwins measuring 30–75 μm are formed in sapphire with abrasive treatment and indentation. The depth of deformation and the dimensions of twin interlayers depend on the crystallographic orientations and the loads applied.

Periodic bond chains (PBC). According to crystal morphology theory [30], the lattice of sapphire has facets parallel to two or more chains of strong bonds (the so-called *F*-type facets). Hartman found a number of chains with "intense bonds," denoted (in rhombohedral symbols) as $\langle 01\bar{1} \rangle$, $\langle 001 \rangle$, $\langle 11\bar{1} \rangle$, $\langle 11\bar{2} \rangle$, $\langle 01\bar{2} \rangle$, $\langle 12\bar{2} \rangle$, $\langle 11\bar{3} \rangle$.

The forms of *F*-type facets are $\{111\}$, $\{001\}$, $\{011\}$, $\{01\bar{1}\}$, $\{112\}$, $\{012\}$, and $\{022\}$ [30]. Other facets are of *S*-type (parallel to one chain of strong bonds) and *K*-type (parallel to no such chains). The gnomonic projection of corundum built by Hartman shows all the *F*-type facets and all the zones parallel to the chains with intense bonds (Fig. 2.108). According to Hartman, the basal plane has 6.6 free
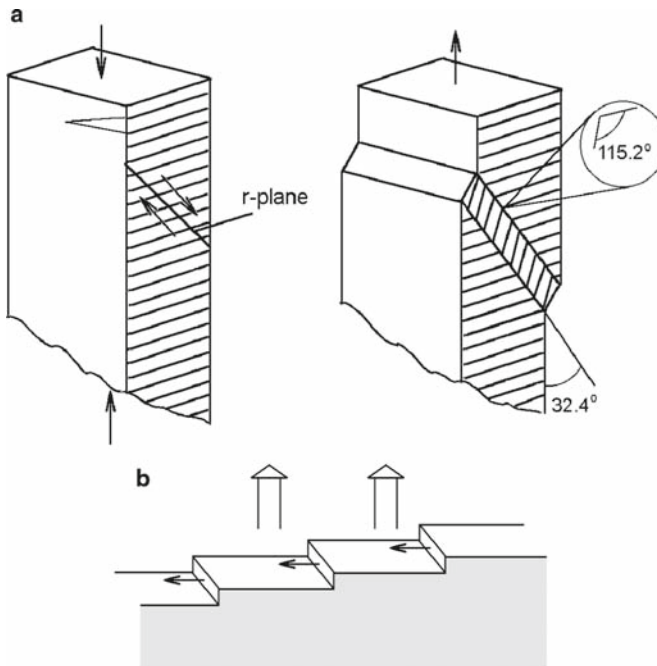
Fig. 2.19 (**a**) Scheme of sapphire twinning in the rhombohedronal plane upon compression. (**b**) Schematic of twin boundary
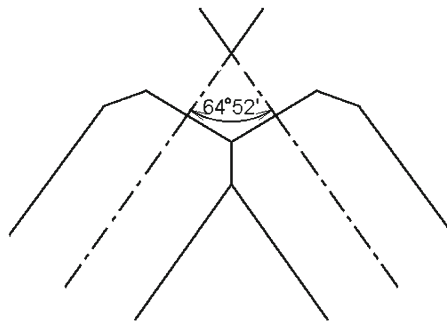
Fig. 2.20 Joint twin of corundum crystals

bonds per unit of plane; for the planes $(10\bar{1}0)$ and $(10\bar{1}1)$ the mentioned quantities are 5.2 and 3.5, respectively. Based on the analysis of chipping planes of crystals grown by the Verneuil method, the directions of $\langle 211 \rangle$, $\langle 210 \rangle$, $\langle \bar{4}\bar{2}1 \rangle$ bonds parallel to the *F*-type face $(1\bar{2}0)$ were established [31].

Morphology of sapphire is defined by the growth conditions and the peculiarities of the structure, including periodic bond chains. The direction of PBC chains defines the stable *F*-faces which will be the slowest growing, and hence of highest morphological importance in the crystal. In order to determine the relative importance of various *F*-faces it is assumed that the growth rate of a face (*hkl*) is directly proportional to its attachment energy, E_{hkl}^{att} [32]. This is the energy released when a layer of thickness d_{hkl} is added to the growing surface. The reverse process in which the energy E_{hkl}^{att} is consumed to produce a certain area of new surface by crystal cleavage suggests a relation between E_{hkl}^{att} and surface energy [33]:

$$\gamma \approx ZE^{att}\, d_{hkl}\, /2V, \tag{2.3}$$

in which *Z* is the number of formula units in a unit cell of volume *V* and d_{hkl} is the interplanar spacing of the lattice plane (*hkl*).

Based on the known γ and E^{att} values one can predict the crystal morphology. Relaxation of the lattice is illustrated in Fig. 2.21 [32]. There are two regions, of which the ions in the outermost region (I) are allowed to relax to equilibrium while the inner region (II) remains static. Writing the force and displacement of the *i*th ion per unit cell of the αth plane as $F_\alpha^{\,i}$ and $\varepsilon_\alpha^{\,i}$, respectively, the equilibrium condition is that
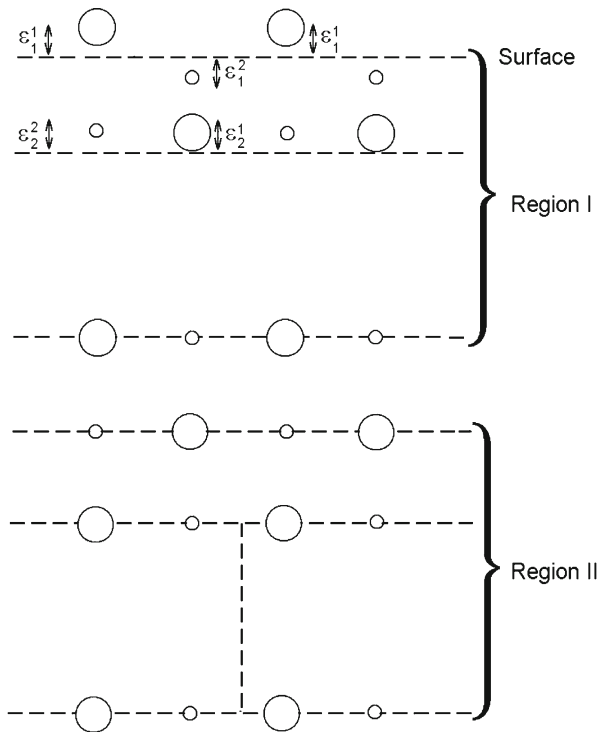

Fig. 2.21   Definition of surface lattice variables

$\partial F_\alpha{}^i / \partial \varepsilon_\alpha{}^i = 0$ for all i and α in region I

This can be shown to be equivalent to minimizing the energy of the outer region, E_{I}, with respect to the displacement, $\varepsilon_\alpha{}^i$, provided the inner region is at equilibrium.

Writing the energy per unit area of given plane (hkl) in the bulk as E_{hkl}^{B}, and that in the surface as E_{hkl}^{S}, γ_{hkl} is given by:

$$\gamma_{hkl} = 1/2(E_{hkl}^{B} - 2E_{hkl}^{S}) \tag{2.4}$$

Calculations have been reported [32] in which 20 surface planes were relaxed to equilibrium, while region II contained up to 60 planes of ions, also at equilibrium. The calculated energy of five lowest index surfaces of sapphire are given in Table 2.4, based on both unrelaxed and relaxed surface structures.

Four points emerge from these results. The first is that surface energies corresponding to relaxed structures are appreciably lower than those for unrelaxed surfaces. The second point is that relaxation energies vary from plane to plane. The basal plane energy is reduced by 3.92 J m^{-2}, or 66%, whereas the energy of the rhombohedral surface is reduced by only 1.34 J m^{-2} or 37%. The third point is that lattice relaxation changes the relative stability of the surfaces. The order of unrelaxed surface energies is

$$\{011\}<\{01\bar{1}\}<\{100\}<\{211\}$$

whereas lattice relaxation changes this to

$$\{111\} < \{211\} \approx \{011\} < \{01\bar{1}\}$$

while according to Hartman the predicted order of surface energies is

$$\{011\}<\{01\bar{1}\}<\{121\},\{100\},\{111\},\{021\}$$

Finally, lattice relaxation reduces the difference in energy between the various surfaces. The difference between the highest and lowest unrelaxed energies is 2.93 J m^{-2}, whereas it is only 0.49 J m^{-2} for relaxed surfaces.

Crystal morphologies corresponding to relaxed and unrelaxed surfaces have been drawn using data given in Table 2.4 (Fig. 2.22). The simple rhombohedral

Table 2.4 Calculated energies of the low-index surfaces of sapphire, $\gamma^0{}_{hkl}$ (J · m^2)

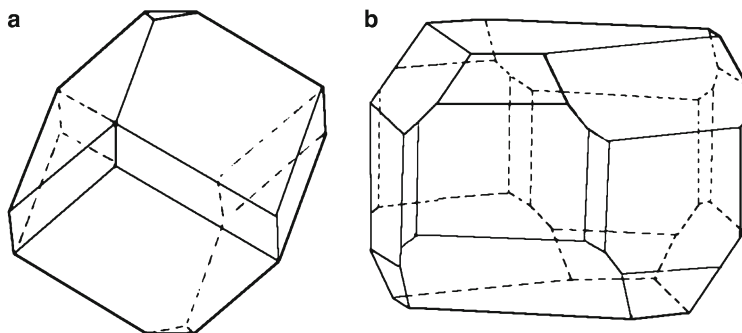| Surface	Unrelaxed energy	Relaxed energy	Hartman [34]
(111)	5.95	2.03	4.83
($\bar{2}$11)	6.46	2.23	–
(01$\bar{1}$)	3.63	2.29	2.55
(01$\bar{1}$)	4.37	2.50	3.80
(100)	5.58	2.52	4.80

Fig. 2.22 The predicted morphology of sapphire based on (**a**) unrelaxed and (**b**) relaxed surfaces

Table 2.5 Comparison of relative surface energies with the theoretical estimates [35, 36]

	Experimental estimate of facet surface energy		Theoretical estimates	
Surface	Sapphire $\gamma_{(hkjl)}/\gamma_{(0001)}$	Ruby 0.54% Cr_2O_3 $\gamma_{(hkjl)}/\gamma_{(0001)}$	First Principles	Interaction model
$\{\bar{1}012\}$	1.05	1.05	1.12	1.13
$\{11\bar{2}0\}$	1.12	1.00	1.06	1.23
$\{11\bar{2}3\}$	1.06			
$\{10\bar{1}1\}$	1.07	1.02	1.45	1.24
$\{10\bar{1}1\}$			0.795	1.10

habit, predicted assuming no surface relaxation, is replaced by more complex morphology in which the basal planes {111} play an increasingly dominant role.

In a number of papers the value of surface energy of the crystallographic planes was established from the analysis of faceted cavities. The equilibrium shape of internal cavities in sapphire was determined through the study of submicron internal cavities in sapphire and ruby (Table 2.5). Cavities were formed from indentation cracks during annealing at 1,870 K. Equilibrium could be reached only for cavities smaller than 100 nm [35]. Controlled-geometry cavities were introduced in sapphire substrates using photolithographic methods and annealing for prolonged periods [37].

The difference between the largest and smallest relative surface energies for sapphire is about 20%. Cavities in ruby are much more isotropic than in sapphire.

The shape of natural crystals usually has the following facets (denoted by the most often used literal symbols): $c(0001)$, $a\{11\bar{2}0\}$, $r\{10\bar{1}1\}$, $n\{22\bar{4}3\}$, $m\{10\bar{1}0\}$, $s\{02\bar{2}1\}$, $s\{22\bar{4}3\}$, $R\{01\bar{1}2\}$, $p\{11\bar{2}3\}$(Fig. 2.23) and others.[1] The symbols of crystallographic planes in the morphological and the structural classification systems,

---

[1] In some countries capital letters A, C, M are used.
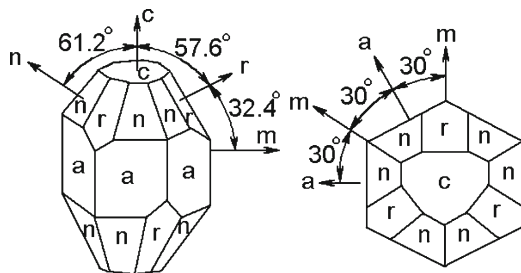
Fig. 2.23   Crystallographic diagram of sapphire
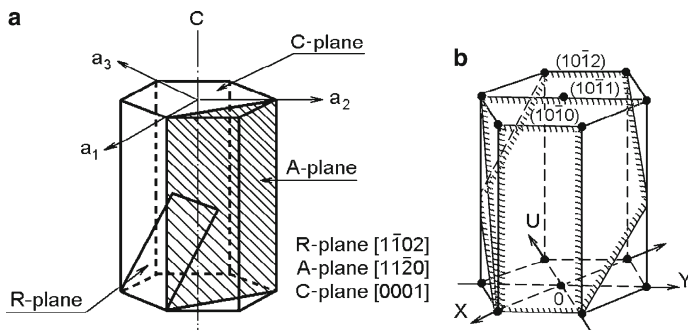
Fig. 2.24   (**a**) Location of the crystallographic planes of sapphire often met in practice. (**b**) Comparison of the symbols of facets with common trace. The trace is parallel to *OY*

the stereographic projections of sapphire, and the Wulff–Bragg angles for some planes are given in Tables 2.40, 2.41 and Fig. 2.109.

Besides the main crystallographic planes, tens of others exist which have their own symbols. The main forms with their spherical coordinates are presented in Table 2.42, as well as others rarely met [38].

The planes that are most often encountered in the practice of sapphire usage[2] are shown in Fig. 2.24. The plane $(10\bar{1}2)$ is inclined to (0001) plane at an angle of $57°36'$, while with the plane $(11\bar{2}0)$ it makes an angle of $32°24'$. The angles between the normals to the facets of sapphire are given in Table 2.43 [1].

Equilibrium forms. The form of a crystal in which free surface energy is minimal at constant temperature, pressure, and volume is considered to be the equilibrium form. The facets of the equilibrium form may appear on the surface of growing crystals. This is why, by taking into account these facets when orienting

---

[2]On occasion the most exotic planes find use, too. For instance, the crystallographic planes $(13\bar{4}28)$, $(32\bar{5}43)$, $(651\bar{1}40)$, etc. are utilized in X-ray optics for backward scattering of photons with energies close to that of Mossbauer ^{57}Fe radiation [5–6].

the crystal, it is possible to influence the character of roughness of the crystalliza-
tion front (CF) [39].

   There are ways to form equilibrium-shaped crystals. One is to heat small crystals
in a closed system at high temperatures so that transport processes are hastened.
This technique is difficult because of the necessity of controlling the external envi-
ronment to prevent a volume change of the crystal by evaporation, corrosion, or
condensation. The other method is to use internal cavities, which are, in effect,
"negative" crystals with very slow lattice diffusion and constant volume in contact
with a fixed atmosphere. The conditions of fixed volume in contact with its vapor
are easier to maintain with the latter case than with the former case. The deviation
of a crystal's shape from its Wulff shape at any time depends on the starting shape
and size of the crystal and the rates of kinetic processes that change its shape (Fig.
2.25) [36]. Segregating dopants have a considerable influence on the Wulff shape,
even in very dilute concentrations (ppm) (Fig. 2.26) [39].

   Experimentally, equilibrium forms are obtained by crystallization or dissolution
of spherical crystals, but solvents, impurities, and other factors often change the
equilibrium form. Conclusions concerning the equilibrium form thus are more reli-
able if made on the basis of the shape of a given crystal in its own melt, where the
influence of solvents is excluded. However, equilibrium crystal forms in the melt
are observed rather rarely, since the form usually is influenced by the temperature
field. Under metastable conditions the equilibrium crystal form in its own melt
transforms first into cellular and then into skeleton and dendritic forms [40, 41].
Depending on the growth conditions, the form of a crystal that is in equilibrium
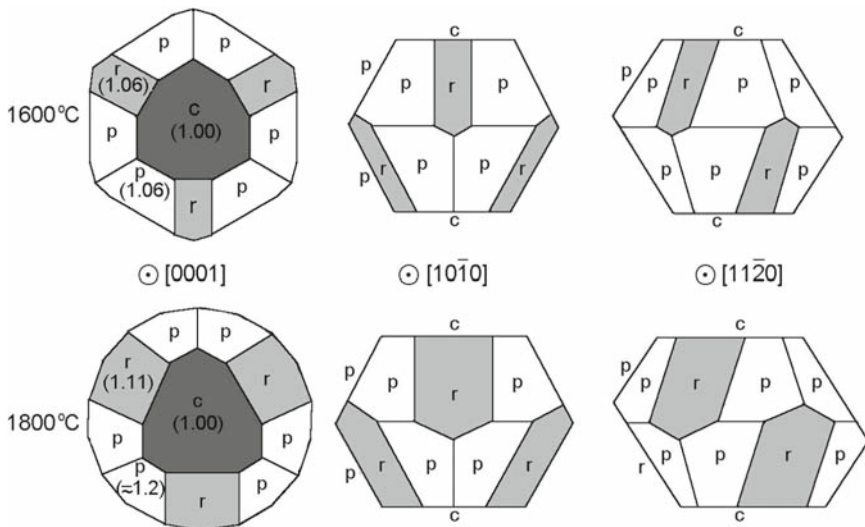

Fig. 2.25 Schematic illustrations of the equilibrium shapes as summing that the Wulff shapes are
fully faceted. Numbers in parentheses indicate the surface energy relative to that of the c(0001)
surface
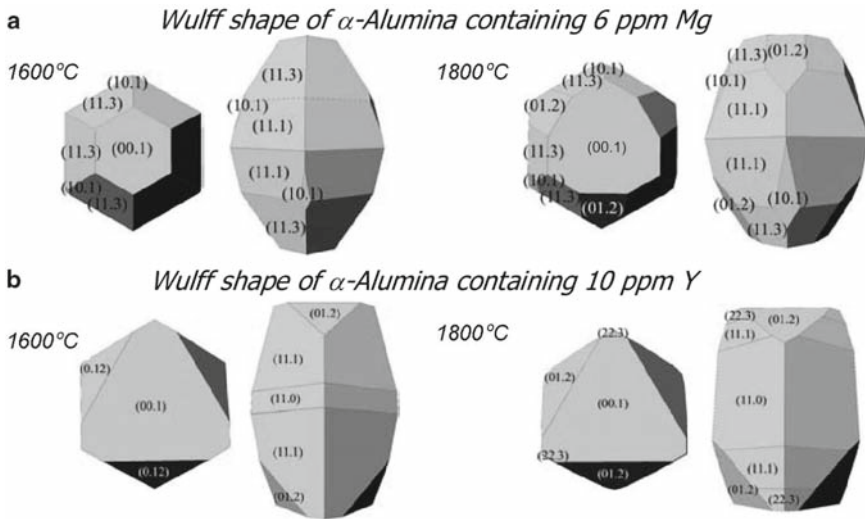
Fig. 2.26   Wulff shape of sapphire containing 6 ppm Mg (**a**) and 10 ppm of Y (**b**)

with the medium may change. However, the form of a skeleton crystal is constant, as it is caused by the properties of the crystal lattice. Therefore, the equilibrium form can be established from the analysis of skeleton and dendrite crystals.

The elementary morphological cell of sapphire corresponding to the positive orientation of the rhombohedron $\{10\bar{1}0\}$ is built on the lattice sites unoccupied by aluminum ions, and describes the arrangement of aluminum ions (Fig. 2.27). The arrangement of these constitutional hollows may be a criterion for estimating the equilibrium form of a crystal. Located inside the elementary morphological rhombohedron are two aluminum ions and three oxygen ions. For the complex Al_2O_3, the growth rate is the highest in the direction of the nearest hollows, which are the rhombohedron vertices. Proceeding from this fact, the morphological rhombohedron $\{10\bar{1}1\}$ is to be considered the equilibrium form of sapphire in its own melt [42]. Thus, skeleton and dendrite crystals demonstrate the predominating growth directions that also allow conclusions about the growth rate anisotropy.

Morphology of crystallization front. As is known, in the process of growth the crystal facet does not move uniformly forward; steps or teeth on it appear (Fig. 2.28) [43]. A cellular CF is observed during the growth of sapphire by the horizontally directed crystallization [44] and Stepanov methods [44, 45].

As a rule, the morphology of the CF is investigated on decantation surfaces [43]. In particular, the decantation surface of the crystal grown in the direction $\{10\bar{1}0\}$ consists of vertices of the elementary morphological rhombohedron $\{10\bar{1}1\}$. During growth of sapphire in the direction $[11\bar{2}0]$, the rhombohedron edge lies in the growth plane, so the CF and the decantation surface have a ribbed structure. During growth in the direction $[0001]$ the decantation surface consists of convex and
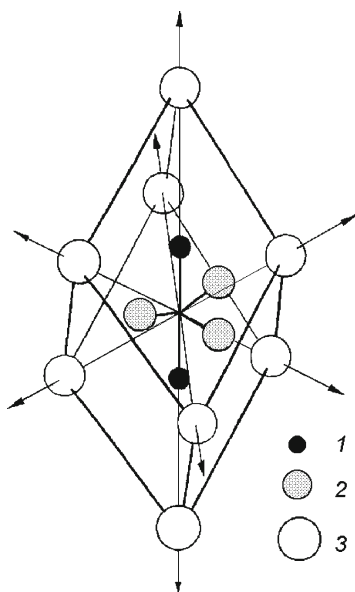
Fig. 2.27 Arrangement of the crystal lattice hollows surrounding the complex Al_2O_3 and the directions of the maximum growth rate; (*1*) aluminum ion, (*2*) oxygen ion, (*3*) octahedral hollows
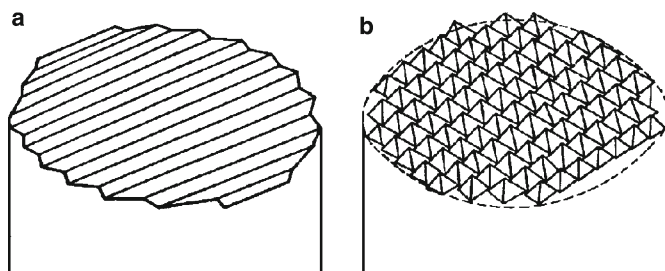
Fig. 2.28 Steps (**a**) and teeth (**b**) on the growing surface of corundum crystals (the Verneuil method; the *C*-axis makes an angle up to 55° with the growth axis)

concave pyramids that correspond to the vertices of the morphological rhombohedron. Thus, the CF of sapphire in its own melt usually is split by the elements of the morphological rhombohedron. The curved surface of the CF is split by those elements of the morphological rhombohedron that coincide with the surface curvature (Fig. 2.29) [46].

Under the conditions of overcooling, skeleton cones are formed on the facets $\{10\bar{1}1\}$ due to the priority growth of the vertices and the edges (Fig. 2.30b), which
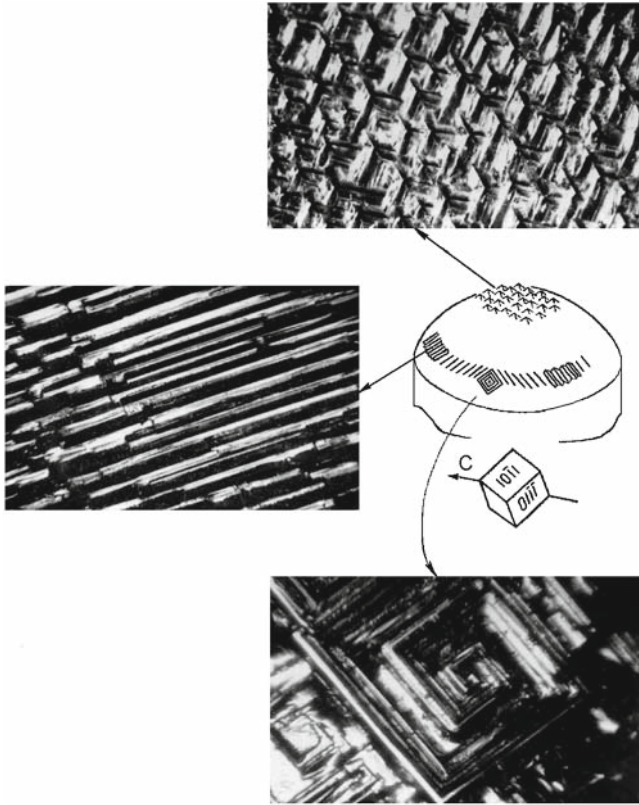
Fig. 2.29 Morphology of the decantation surface of sapphire grown in the direction [10$\bar{1}$0] ($\times$ 50)

may lead further to skeleton crystal growth. Overcooling of the melt favors predominating growth of the rhombohedron vertices and dendritic growth. Characteristically, the branches of the dendrite crystals are oriented in the directions of the rhombohedron vertices and the angles between them correspond to the angles between the rhombohedron diagonals (Fig. 2.30a).

2.1.2   Optical Properties

Refraction. In sapphire the refractive index of the ordinary ray is higher than in a great number of optical materials. This is caused by close packing of oxygen ions in the lattice and by ionic polarization. Malitson presented the refractive indexes for
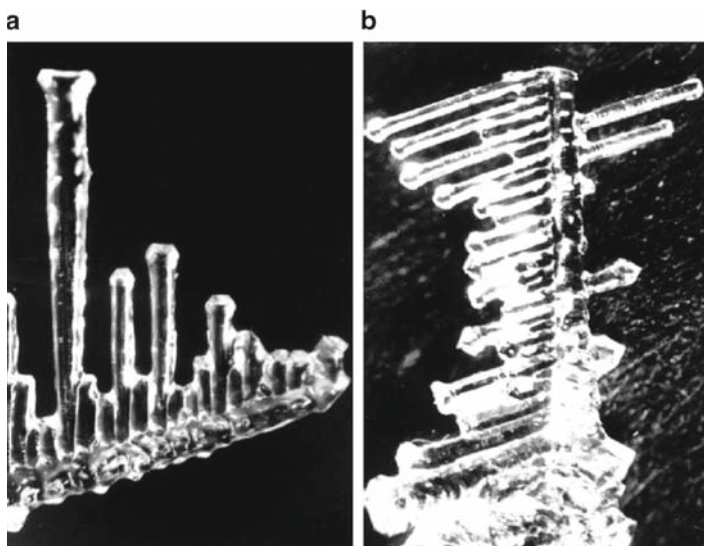
Fig. 2.30 (**a**) Dendritic sapphire branch (×15); (**b**) skeleton cone of sapphire crystal on the plane $(10\bar{1}1)(×15)$
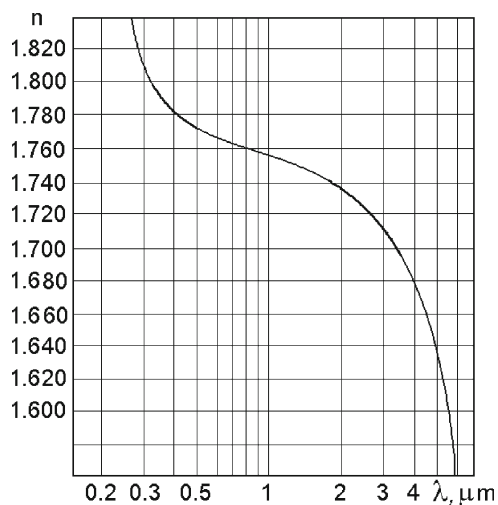
Fig. 2.31 Dependence of the refractive index on wavelength

different wavelengths in the interval 0.2–6 μm [47]. They increase with decreasing wavelength (Fig. 2.31) and reach a maxima of 2.5 in the vacuum ultraviolet ($\lambda =$ 0.1425 μm). As a rule, the refractive indexes of sapphire in the IR region of the spectra are given without reference to Freneuil loss.

Sapphire is a uniaxial optically negative crystal. It has one direction along the optical axis in which birefringence does not occur and the refractive index of the extraordinary ray is less than that of the ordinary ray. The difference between these values in the visible region of the spectrum is ~0.008. In the UV region, in the vicinity of the maxima point, it grows to 0.012 and drops to zero at the maxima.

Refractive index is temperature-dependent [48, 49]. Figures 2.32 and 2.33 show the temperature-dependencies of the refractive index at 3.39 μm wavelength for the ordinary and extraordinary rays.

Values for the refractive index of sapphire in the region of partial transparency and nontransparency at different temperatures are given in Tables 2.44 and 2.45. The thermo-optical coefficient of the refractive index dn/dt for the ordinary and extraordinary rays is presented in Table 2.6.
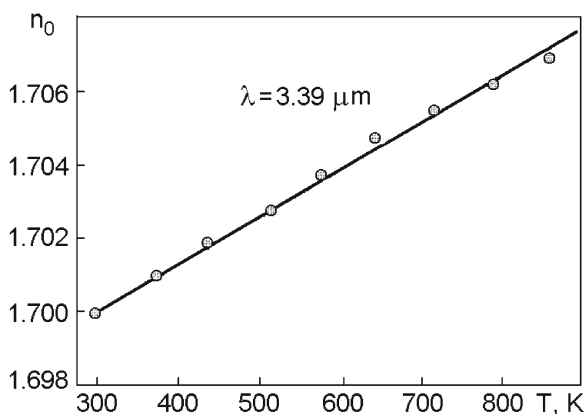
Fig. 2.32 Temperature dependence of the refractive index for the ordinary ray
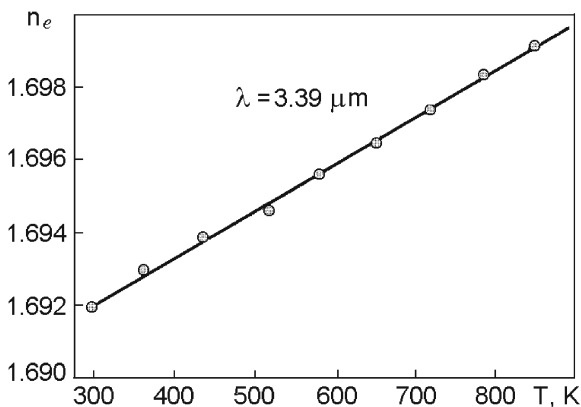
Fig. 2.33 Temperature dependence of the refractive index for the extraordinary ray

Table 2.6 Thermo-optical coefficient for the ordinary (dn_0/dT) and extraordinary rays (dn_e/dT) [49]

Wave-length (µm)	1	1.67	2.5	2.86	3.3	4	5
dn_0/dT (K^{-1})		$8.2 \cdot 10^{-6}$	$8.8 \cdot 10^{-6}$	$9.9 \cdot 10^{-6}$	$1.13 \cdot 10^{-5}$		$1.41 \cdot 10^{-5}$
dn_e/dT (K^{-1})					$1.151 \cdot 10^{-5}$	$1.24 \cdot 10^{-5}$ $1.403 \cdot 10^{-5}$	$1.556 \cdot 10^{-5}$
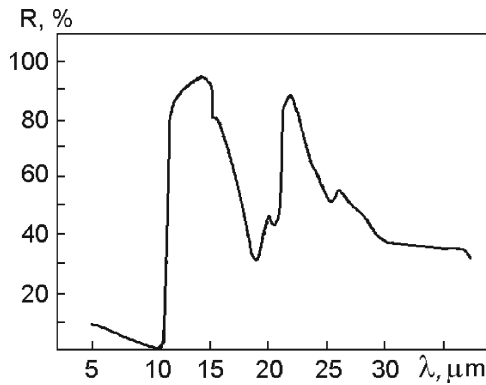
Fig. 2.34 Dependence of the reflection coefficient on wavelength

The equation for refractive index dispersion has the following form:

$$n^2 - 1 = \sum_{i=1}^{3} A_i \lambda^2 / (\lambda^2 - B_i^2), \tag{2.5}$$

where A_i and B_i are constants with A_1 = 1.023798, A_2 = 1.058264, A_3 = 5.280792, B_1 = 0.06144821, B_2 = 0.1106997, and B_3 = 17.92656.

Reflection. The reflection coefficient of a polished sapphire surface (R_z = 0.1 µm) at n = 1.768 is equal to 7.8%. Reflection essentially is dependent on the wavelength (Fig. 2.34) and the state of the surface, which changes with mechanical and thermal treatment. In the IR region of the spectrum, the reflection coefficient sharply increases at λ = 11 µm and its maxima are observed at 13.5 and 22 µm. The values of effective coefficient of mirror reflection of a sapphire surface subjected to different types of mechanical treatment (R_0) and thermal treatment in aluminum oxide vapor at 2,250 K for 1.5 h (R_1) and 8 h (R_2) are presented in Table 2.7.

Table 2.7 Coefficients of effective mirror reflection of the surface depending on its roughness and the angle of ray incidence (in %)

θ (deg.)	R_z (μm)								
	0.1–0.2			1.1–2.5			6.3–10		
	R_0	R_1	R_2	R_0	R_1	R_2	R_0	R_1	R_2
10	8.0	7.8	7.8	0.06	0.06	0.58	0.02	0.04	0.18
20	8.0	7.8	7.8	0.06	0.068	0.60	0.02	0.05	0.18
30	8.0	8.3	8.3	0.10	0.80	0.70	0.04	0.10	0.20
40	10.3	9.5	9.5	0.12	1.00	0.80	0.06	0.18	0.30
50	12.0	11.0	12.0	0.18	1.30	1.10	0.14	0.26	0.50
60	17.5	17.0	17.5	0.30	1.70	1.40	0.34	0.40	0.80
70	27.5	22.5	27.0	0.66	3.7	2.00	0.7	1.00	1.38
80	48.0	45.0	48.0	1.86	15.00	10.40	1.60	1.70	1.90
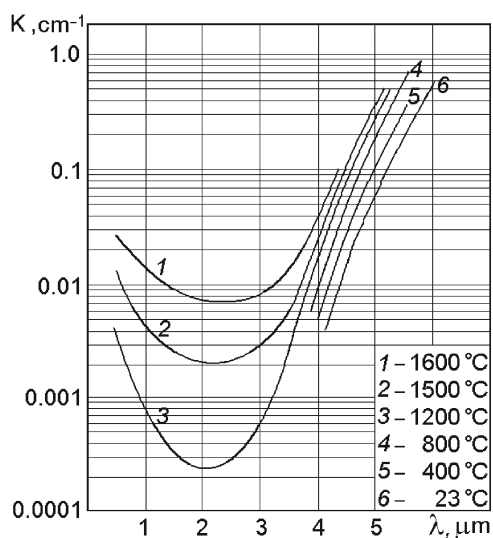
Fig. 2.35 Temperature dependence of the absorption coefficient

Absorption. The absorption coefficient of sapphire is temperature-dependent (Fig. 2.35) [50]. In the IR region, the value of absorption rises with temperature and reaches 0.28 cm^{-1} in the region of premelting temperature.

Structural perfection and impurity composition of crystals essentially affect their absorption. In particular, a considerable value of the absorption coefficient of ruby in the visible region of the spectrum is caused by Cr^{3+} ions. The absorption coefficients at the absorption band maximum for the ordinary and extraordinary waves are presented in Table 2.46.

Ruby is pleochroic, i.e., absorbs the ordinary and extraordinary rays in a different way. In the direction perpendicular to the optical axis the crystal has an intense violet-red color. In the direction parallel to the optical axis its color is yellowish-red and less intense. The absorption spectra of crystals with different impurities are presented in Fig. 2.110.

The absorption coefficient of sapphire is investigated in many papers. Despite disagreement in the results, they have been generalized [51] (Table 2.47). The general scheme for determination of the recommended values is the following. Based on the available literature data on the temperature dependence of the absorption coefficient and taking into account the error of the measurement method, the averaged dependence $k_\lambda(T)$ is built for each wavelength with a step of 0.1 μm. This is used to build the absorption spectra $k_\lambda(\lambda)$.

The absorption coefficients of sapphire are proportional to the following powers of temperature $(T^n)/n = 2.2$ for $\lambda = 4.2$ μm, $n = 2$ for $\lambda = 4.5$–5.5 μm, $n = 1.5$ for $\lambda = 6$ μm, $n = 1.2$ for $\lambda = 6.5$ μm, and $n = 1$ for $\lambda = 7$ μm.

The recommended values of absorption coefficient obtained from an analysis of literature data are to be considered as reference only. For some spectral temperatures, these have been extrapolated.

Transmission. As a rule, transmission in sapphire is described by the curve presented in Fig. 2.36. It was obtained for pure, sufficiently perfect crystals grown by the Czochralski method (Linde Cz UV grade). The samples were 1 mm thick. In the UV region, transmission of thin plates is essentially limited by the Fresnel loss. The presented values do not take into account this loss. Recent data on the transmission of pure perfect crystals in the UV region (UV grade) are presented in Fig. 2.37.

Transmission in the UV region is increased by high-quality polish of the surfaces (20/10 scratch-dig). Low-quality polish may diminish the value of transmission by ~10%. The quality of the surface polish is especially significant for $\lambda < 250$ μm. The presence of point defects and impurities gives rise to absorption at 204, 230, and 400 μm wavelengths. For real samples the value of transmission also depends
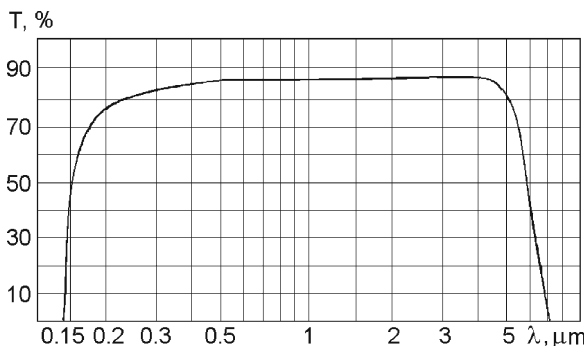
Fig. 2.36 Transmission of sapphire
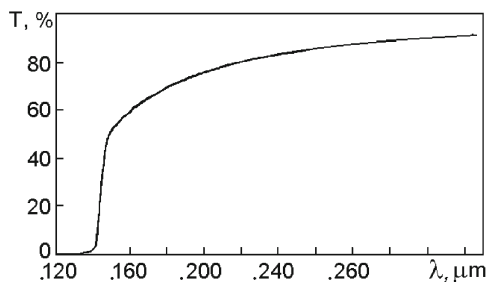
Fig. 2.37 Transmission of sapphire in the UV region
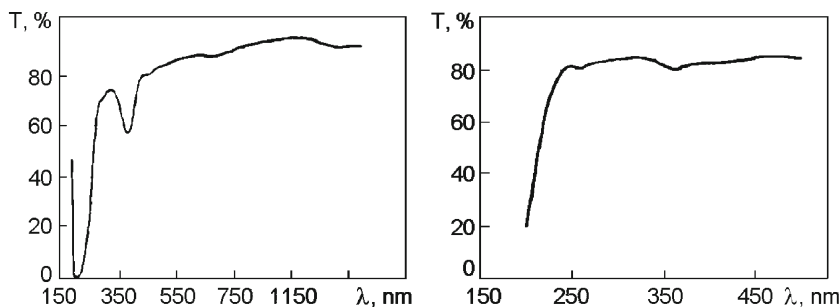
Fig. 2.38 Transmission spectra of 10-mm-thick sapphire grown using (**a**) molybdenum and (**b**) tungsten components

on the medium in the growth chamber and even the equipment components used (Fig. 2.38, [52]).

The X- and γ-irradiation of sapphire increases optical absorption; n- and γ-irradiation give rise to the formation of color centers and consequently to the appearance of absorption bands, which can be eliminated with high-temperature annealing.

In the IR region of the spectrum, sapphire possesses high transmission at wavelengths ranging from 1.0 to 5.5 μm. In the 1.0- to 4.0-μm interval, the value of transmission is ~85–86% (Fig. 2.39). Starting from $\lambda > 3$ μm the value of transmission decreases as temperature grows (Fig. 2.40). At $T < 80$ K, the transmission of sapphire increases in the extreme IR region (Fig. 2.40). Due to such an effect, sapphire can be used in cold inner windows for IR measurements.

As sapphire possesses high transmission without taking into account Fresnel loss, it can be applied in those cases when other optical materials require antireflection coatings. These coatings are able to decrease the loss by reflection and essentially increase transmission (Fig. 2.41). Starting from $\lambda > 3$ μm, the value of transmission decreases with the growth of temperature (Fig. 2.42).

Scattering in sapphire depends on the wavelength. Relative scattering diminishes with increasing wavelength and reaches its maximum at $\lambda = 1.3$ μm.
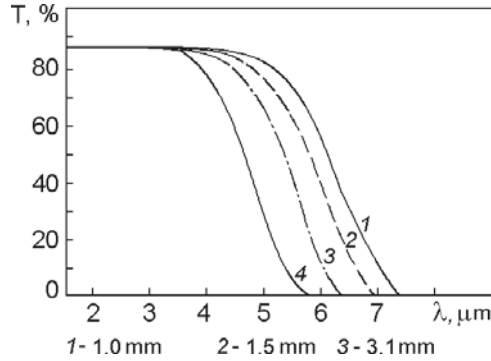
Fig. 2.39 Transmission in IR region. Thick (*1*) 1 mm, 293 K; (*2*) 1.5 mm, 293 K; (*3*) 3.1 mm, 293 K; (*4*) 4 mm, 793 K
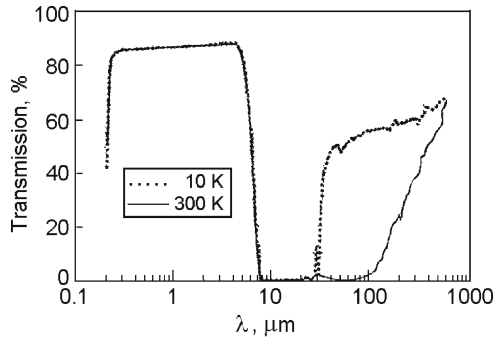
Fig. 2.40 Transmission of 2-mm-thick sapphire in the IR region at 10 and 300 K
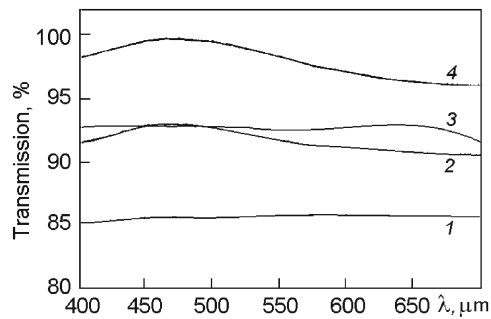
Fig. 2.41 Antireflection coating external transmission: (*1*) no coating; (*2*) one side AR coating; (*3*) one side multicoating; (*4*) both sides AR coating

Photoelastic constant	$2.1 \cdot 10^{-7}$ cm^2/kg [1]
Brewster angle	60.4°
Total internal reflection angle	34.5°
Abbe number ($n_0 - 1/n_f - n_c$)	72.20 (parallel to *C*)
Dispersive power ($n_f - n_c$)	0.011
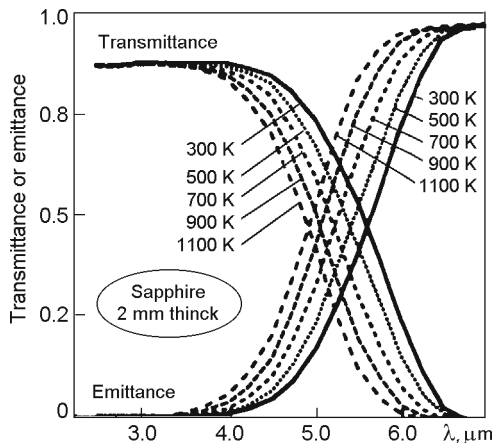
Fig. 2.42 Transmittance and emittance normal to surface (∥ *C*-axis of the crystal)
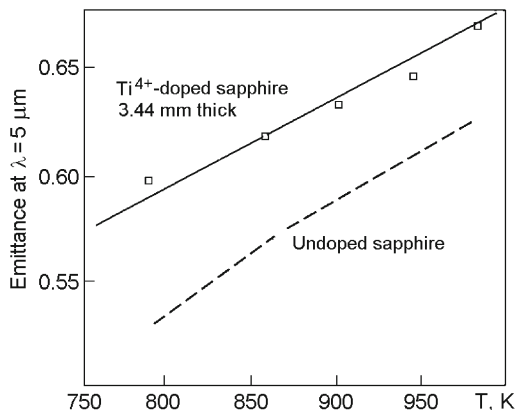
Fig. 2.43 Emittance of Ti⁴⁺-doped sapphire

Emittance. Emittance is the ratio of the radiative energy of a body to the corresponding energy of black body radiation at the same temperature. Emission remains low up to $\lambda \sim 4$ μm (Fig. 2.42). It increases with wavelength and temperature. Doping of sapphire increases emittance (Figs. 2.43 and 2.44) [53].

Optical properties in the region of phase transition undergo changes due to a considerable distinction in the properties of the liquid and solid phases. For instance, at $\lambda = 0.6$ μm in the visible region of the spectrum the scattering coefficient (K) of the melt is ~25 cm⁻¹ at 2,400 K, whereas at 2,300 K (solid phase) $K = 0.36$ cm⁻¹. For the same wavelength the refractive index at the phase transition changes from 1.78 to 1.81 in a narrow temperature interval (60–70°). In the 0.3- to 30-μm region the values of K differ by 2–2.5 orders. As seen from the optical property behavior of sapphire crystal and its melt in the region of the phase transition
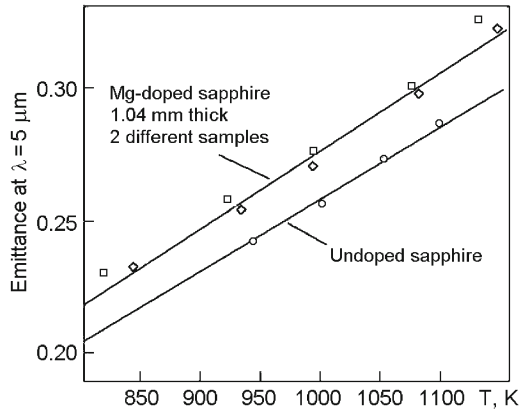
Fig. 2.44 Emittance of Mg-doped sapphire
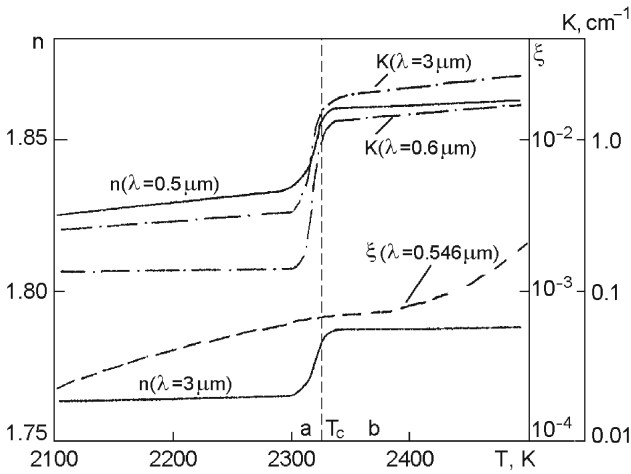
Fig. 2.45 Temperature-dependent behavior of the refractive index (n), absorption index (ξ), and absorption coefficient (K) for (**a**) sapphire and (**b**) its melt in the region of the phase transition (for 25-mm-thick melt-crystal layer)

(Fig. 2.45), it is only the absorption coefficient that smoothly changes, but it has no essential influence on the radiation-conductive heat transfer in this region [51].

Luminescence of sapphire is caused by impurities or lattice defects. Several weak luminescence bands are observed in sapphire. Their intensity depends on the type of impurity and the crystal's history. Luminescence in the region of 290–335 and 650–774 nm is related to the lattice defects and impurity ions, respectively. In particular, chromium ions emit in the region of 650–774 nm; manganese ions emit in the region of 680 nm; the 620-nm line is attributed to vanadium ions; and the
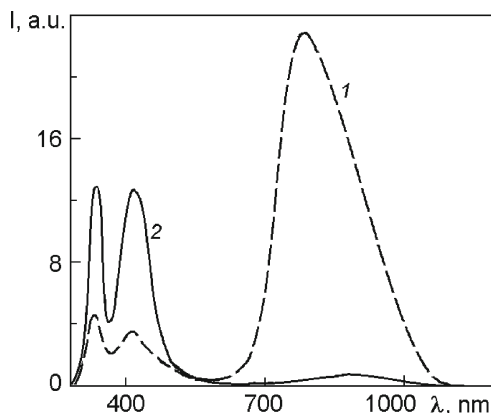
Fig. 2.46 Cathodoluminescence spectrum of (*1*) nonirradiated sapphire and (*2*) sapphire preliminarily irradiated on a linear accelerator

480-, 530-, and 600-nm lines correspond to divalent cobalt ions. The most widespread luminescent impurities are chromium and titanium. The $Cr:Al_2O_3$ crystals possess intense RL with a dominating band at 695 nm (1.78 eV), prolonged afterglow at room temperature (exceeding 10 h), considerable accumulated light sum, and typical TSL peak at 300°C, the intensity of which correlates with the content of chromium.

The comparison of sapphire grown by different methods [54] shows that crystals obtained by hydrothermal methods possess the minimum accumulated light sum, weak glow at laser, X-ray, electronic excitation, and fast afterglow decay. Meanwhile, these crystals have the lowest radiation resistance. As a rule, irradiation of the crystal and increasing temperature increase the glow intensity of some bands or change the ratio of their intensities. Only in $Ti^{3+}:Al_2O_3$ does the luminescence intensity at nitrogen temperatures turn out to exceed that at room temperature [55]). Figure 2.46 gives a characteristic example of the behavior of the glow band intensities ratio [56].

The intensity of the low-energy part of the luminescence spectrum sharply diminishes at helium temperatures, as the phonon component of luminescence is frozen out. Many types of luminescence (e.g., cathodoluminescence and photoluminescence) in nonactivated crystals have the same nature. Therefore, the absence of photoluminescence at cathodoluminescence reported in some papers can be referred to the distinction in the density of excitation.

TSL of nonactivated sapphire is distinguished by the presence of a thermopeak at 408 K. In UV-irradiated $Ti:Al_2O_3$, TSL is characterized by thermopeaks with the maxima at 423 and 495–500 K. The TSL spectrum consists of 290- and 410-nm bands. The intensity and spectrum of TSL depend on the titanium content and on the oxidation–reduction potential of the crystal growth and annealing media. To explain the dependence, three models of activation–vacancy centers are proposed [57].

The TSL spectra of sapphire irradiated with neutrons and excited with X-rays contain bands at 2.4, 3.7, and 2.8–3.1 eV, which coincide with the luminescence bands at photoexcitation. After proton irradiation the luminescence bands at 260, 330, 390, 410, and 510 nm were registered [58]. Several luminescence (emission) bands (3.80, 3.18, 2.82, 2.43, 2.23 eV) appeared, irrespective of thee sample's prehistory, at the excitation of sapphire irradiated by neutrons [59].

Besides luminescence in thermal equilibrium with the lattice, nonequilibrium luminescence or emission upon relaxation of electrons on electron and electron-oscillating levels also are observed on intense pumping with a Cr:Al$_2$O$_3$ laser. This luminescence possesses a continuous spectrum, and its intensity is defined by the wavelength of the exciting laser and is by several orders weaker than equilibrium luminescence.

The luminescence caused by lattice defects of sapphire grown under thermodynamically nonequilibrium conditions often is observed in different regions of the spectrum. The 330 nm band is caused by the main radiative transition IB → IA in F^+ centers. Emission in the 450- to 660-nm region is related to R centers (three unified F centers, e.g., three anion vacancies that captured three electrons) [60]. Glow in the 420-nm region also is related to aggregate centers. According to data reported [61], this is a P^- center (the neighboring anion and cation vacancies). The capture of an electron by this pair leads to the formation of a P center, whereas the capture of a hole leads to the appearance of a P^{2-} center.

Emission in the 510-nm band is observed in neutron-irradiated samples, attributed to interstitial Al$^+$ [62]. This ion can be stabilized by electron capture. It has been identified [63] according to the absorption band at 4.1 eV, the luminescence band at 2.45 eV, and a narrow luminescence band at 3.8 eV. Figure 2.47 shows the proposed scheme of its energy levels.
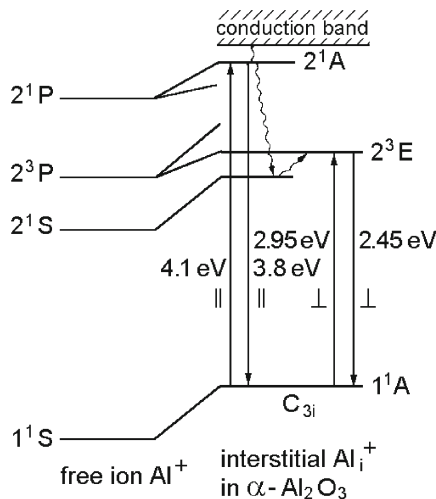
Fig. 2.47   Scheme of energy levels of Al$^+$ centers

Emission in the 550- and 595-nm bands observed in nonirradiated crystals are related to vacancy aggregates [64]. This is accompanied with glow in the 329- to 335- and 388- to 420-nm bands also related to vacancy centers. During γ-irradiation, the charge is transferred from centers that emit in the region of 550–595 nm to centers with emission in the 510-nm band.

It is difficult to compare quantitative luminescence results obtained by different researchers, as these results may reflect random features of the studied samples. The influence of anionic and cationic nonstoichiometry on luminescence was investigated [65] on samples with the same composition and initial structural perfection (Figs. 2.48–2.50).
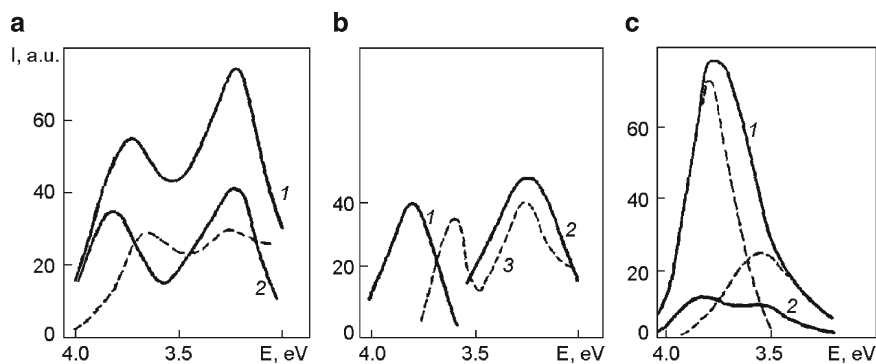
Fig. 2.48 Spectrum of fast-decaying luminescence for α-Al$_2$O$_3$ with anionic nonstoichiometry. (**a**) T = 80 K. (*1*) spectrum measured at the instant of termination of excitation pulse (5 ns); (*2*) since 50 ns. *Dashed line* shows the difference spectrum (*1–2*). (**b**) T = 80 K. Resolution of the luminescence spectrum into components with different decay times τ, ns: (*1*) 50, (*2*) 30, (*3*) short component with $\tau \leq 5$ ns. (**c**) T = 295 K. (*1*) at the instant of termination of excitation pulse, (*2*) since 200 ns. *Dashed line* corresponds to resolution of the spectrum into the components
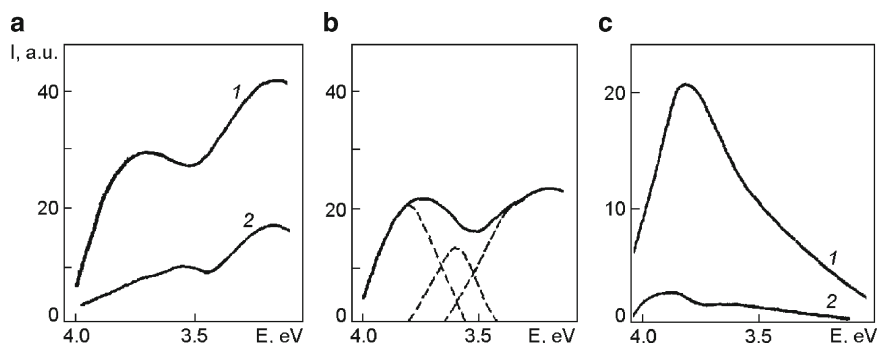
Fig. 2.49 Spectrum of fast-decaying luminescence for α-Al$_2$O$_3$ with cationic nonstoichiometry. (**a**) T = 80 K; (*1*) spectrum measured at the instant of termination of excitation pulse; (*2*) since 25 ns. (**b**) T = 80 K. Resolution of the difference spectrum (*1–2*) into components. (**c**) T= 295 K; (*1*) at the instant of termination of excitation pulse; (*2*) since 400 ns
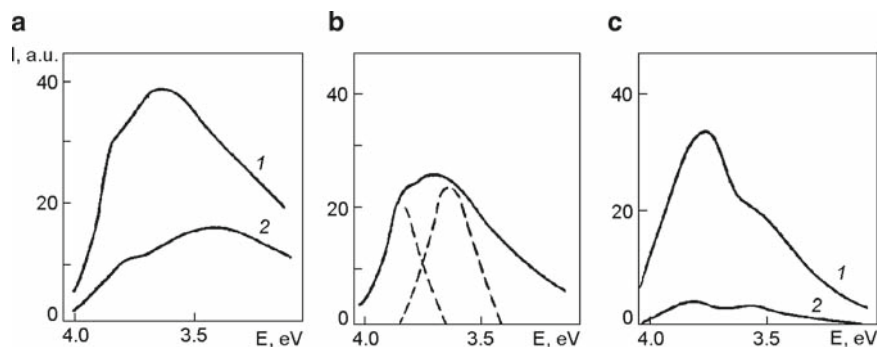
Fig. 2.50 Spectrum of fast-decaying luminescence for α-Al$_2$O$_3$ with anionic nonstoichiometry (normalized sample). (**a**) T= 80 K; (*1*) spectrum measured at the instant of termination of excitation pulse; (*2*) since 25 ns. (**b**) T= 80 K. Resolution of the difference spectrum (*1–2*) into components. (**c**) T= 295 K; (*1*) at the instant of termination of excitation pulse; (*2*) since 400 ns

Table 2.8 Spectral and kinetic characteristics of centers responsible for luminescence bands 3.8 eV in sapphire

Type of center	Luminescence band (eV)	W (eV)		t (s)	
		80 K	300 K	80 K	300 K
F^+	3.8	0.34	0.41	$7 \cdot 10^{-9}$	$7 \cdot 10^{-9}$
Al$^+$	3.82	0.18	0.22	–	–
	2.45	–	–	–	$5 \cdot 10^{-2}$
ALE	3.8	0.35	0.46	$2.8 \cdot 10^{-8}$	$2.8 \cdot 10^{-8}$

As seen from the figure, the luminescence intensity is highest in the crystals with anionic nonstoichiometry, while in the crystals with cationic nonstoichiometry it is the lowest. The luminescence decay times differ significantly, too. It is interesting to investigate the luminescence with E_m = 3.8 eV. The luminescence band may be caused by F^+ centers, interstitial Al$^+$ ions, and autolocalized excitons (ALE) in the anionic sublattice. The glow of these defects has different band half-widths (W) and intercenter decay times (Table. 2.8).

Clarification of the nature of the defects responsible for the observed glow is possible through comparison of Table 2.8 data and that of Figs. 2.40–2.42 with the spectral and kinetic parameters of the 3.8-eV band luminescence in the time interval 10^{-9}–10^{-7} s for the crystals with different nonstoichiometry (Table 2.9).

The fast-decaying 3.8-eV luminescence probably is caused by interstitial aluminum. The half-width of the observed glow band is significantly smaller and closer to that of the Al$^+$ center glow band than to other centers (Table 2.8). The half-width of the luminescence band (0.25 eV), which is larger than for Al$^+$ center luminescence (0.2 eV), is explained by the fact that the defect is not isolated, but forms the Frenkel pair Al$^+$–V_{Al}^{3-}.

Table 2.9 Spectral and kinetic parameters of 3.8 eV luminescence band [65]

Type of sapphire	W (eV)		t (s)		I (rel.unit)	
	80 K	300 K	80 K	300 K	80 K	300 K
Stoichiometric	0.25	0.38	30	200	25	30
Anionic	0.25	0.25	50	35	40	40
nonstoichiometry	–	0.4	–	200	–	40
Cationic	0.3	0.4	35	200	20	20
nonstoichiometry						
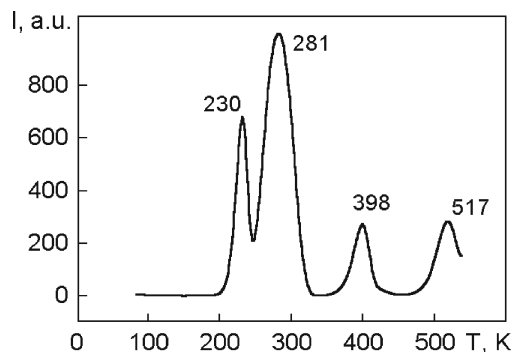
Fig. 2.51 Thermoluminescence curve for sapphire. The heating rate is 0.15 K/s

The threshold energy of the aluminum ion shift into the interstice is 18 eV [66]. Such a shift can be realized by a 300-keV electron. The concentration of these defects is less than ~10^{12} cm^{-3} per pulse. As evident from general considerations, the movement of the cation to the interstice is promoted by the presence of free space formed by anion vacancies in the nearest coordination sphere. Therefore, at higher V_O^{2+} concentrations the shift of the aluminum into the interstice leads to the formation of a pair of defects with an increased distance between pair components. This conclusion agrees with the fact that the lifetime of a Frenkel pair in samples with an ionic nonstoichiometry at 80 K (50 ns) exceeds that of such a pair in stoichiometric samples (~30 ns). Besides active laser media, the luminescent (thermoluminescent) properties of sapphire and ruby are used in radiation dosimeters (see Chap. 1), pressure gauges, luminescence receivers, and ionizing radiation converters.

The thermoluminescence spectrum of undoped sapphire is characterized by several bands (Fig. 2.51). In the low-temperature region, a peak at 100 K is observed in all samples. Its intensity is very low and can be recorded only at considerable amplification. Two other peaks have maxima within the 223–240 and 261–281 K ranges depending on the individual sample. They overlap in part, so the maximum

temperature shifts. The intensity ratio between those peaks depends on the excitation duration. Several partially overlapping peaks are observed in the 350–600 K range [67].

Studies of the 280-K thermoluminescence peak decay kinetics show it has a complex structure and is a superposition of at least two neighboring elementary peaks. As the light sum increases, the intensity of the low-temperature component rises faster than that of the main component. The studied trapping centers (TC) are shown to be defects present in the samples prior to excitation. The values of TC activation energy in undoped sapphire form a single oscillatory series, the oscillatory quantum energy $h\omega_{TL}$ being 0.079 eV (642 cm^{-1}).

2.1.3   Mechanical Characteristics

Density, measured by the method of hydrostatic weighing to an accuracy of 0.05%, varies from 3.97 to 3.99 g/cm^3 for sapphire and to 4.013 g/cm^3 for dark-colored ruby containing 2.97% of Cr_2O_3. Its dependence on the content of chromium is linear. Some impurities, such as titanium, calcium, and so forth, diminish the value of density. Calculated values of density somewhat exceed experimental values, and this is connected to the presence of micropores, microcracks, and so forth in the real crystals.

Hardness. Mohs' hardness is equal to 9; the value of hardness measured according to the 15-point Ridgway scale is 12. Knoop hardness measured parallel and perpendicular to the *C*-axis is 1,900 and 2,200 kg/mm^2, respectively. Knoop hardness values range from 1,525 to 2,200 kg/mm^2. The values of microhardness measured by microindentation of the surface are 19.40 GPa (parallel to the optical axis), 23.15 GPa (at an angle of 60° with the axis), and 22.0 GPa (perpendicular to the axis). The microhardness of α-$Al_2{}^{18}O$ is noticeably higher (the bond Al_2–^{18}O is shorter than the bond Al_2–^{16}O).

The friction coefficient has been investigated under a load applied perpendicularly to polished end surfaces. The lower component of the friction pair was rotating, whereas the upper remained immovable. The sliding friction coefficient of such sapphire pairs depends on orientation (Fig. 2.52) [68]. For friction against steel it is dependent on the pressure and the lubricant used (Table 2.10). The abrasion resistance (according to Mackensen) is 0.12 mm.

The elastic constants of sapphire measured at room temperature [69, 70] and the temperature dependence of pliability are presented in Tables 2.48 and 2.49.

The values of ultimate strength from different types of sapphire testing are contained in Table 2.57.

Tensile strength is 275–400 MPa (4–$6 \cdot 10^4$ psi);

Bending strength is 450–895 MPa. According to other sources, the bending strength in the direction parallel to the *C*-axis is 1.03 GPa ($1.5 \cdot 10^5$ psi) and in the direction perpendicular to the *C*-axis is 758 MPa ($1.1 \cdot 10^5$ psi) (catalogues of leading sapphire producers).

Compression strength is 2 GPa ($3 \cdot 10^5$ psi).
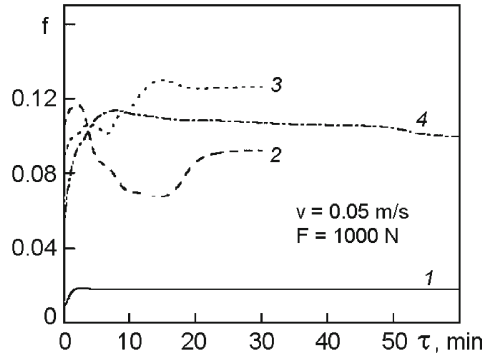
Fig. 2.52 Influence of the crystallographic orientation on the friction coefficient for sapphire pairs. (*1*) (0001), (*2*) (10$\bar{1}$0), (*3*) (11$\bar{2}$0), (*4*) (10$\bar{1}$2). For all cases the second component was a sample with a surface parallel to the plane (0001)

Table 2.10 Friction coefficients at different pressures

P	P/S (GPa)	Sapphire–steel	Ruby–steel
5	1.7	0.33/0.13	0.40/0.12
10	2.6	0.31/0.15	0.37/0.15
15	3.0	0.28/0.17	0.30/0.12
20	3.3	0.25/0.15	0.28/0.11
25	3.5	0.23/0.15	0.26/0.12
30	3.7	0.22/0.14	0.25/0.12

The magnitudes in front of the slash correspond to the dry friction coefficients; those behind the slash are the coefficients after clock mechanism oiling

Young's modulus (elasticity modulus) is the value opposite to pliability: $E = 1/S_{33}$. For different crystallographic directions this value is the following $E_{[0001]} = 1/S_{33}$, $E_{[11\bar{2}0]} = 1/S_{11}$. Presented below are the Young's moduli (GPa) measured by different authors [1]:

Crystallographic direction	Young's Modulus			
[0001]	469.7	467.0	461.2	328.0
[11$\bar{2}$0]	494.0	447.1	358.9	324.0
[10$\bar{1}$0]	–	–	–	322.0

The value of the Young's modulus is temperature-dependent: $E_{[0001]} = 435$ GPa ($63 \cdot 10^6$ psi) at 323 K, $E_{[0001]} = 386$ GPa ($56 \cdot 10^6$ psi) at 1,273 K. At present, the value of the Young's modulus most often used in calculations is 345 GPa ($50 \cdot 10^6$ psi).

Compression modulus is 250 GPa ($36 \cdot 10^6$ psi).

Shear modulus (rigidity modulus) is 145 GPa ($21 \cdot 10^6$ psi)–175 GPa ($26 \cdot 10^6$ psi).

Rupture modulus is 350–690 MPa ($5–10 \cdot 10^4$ psi).

Weibull modulus is the probability of brittle failure for a material under a stress exceeding its ultimate strength σ_S. If P_0 is the probability of failure per unit volume

of material, then the probability of failure for a sample with volume V is found from the equation

$$(1 - P_0)^V = 1 - P \tag{2.6}$$

The expression $1 - P_0$ is the probability of survival per unit volume of material under the stress σ; $1 - P$ is the probability of survival for the entire sample with volume V under the same stress.

Weibull's theory describes the probability of cumulative failure P as a function of the applied tensile stress σ and predicates on tensile-stress initiated fracture at strength-limiting surface flaws. Depending on the state of the surface (and even of the ends) and the sample's history, the Weibull modulus may vary from 5.38 (as grown) and 6.35 (annealed) [71] to 6.07 upon chemical–mechanical polishing [72] and even up to 9.79 [73].

As shown [73], chemical–mechanical polishing can improve the high-temperature strength characteristic of C-plane sapphire by 150% and the room-temperature Weibull modulus by 100% (Figs. 2.53 and 2.54). The results were obtained on samples polished in different companies.

Poisson coefficient is 0.27–0.30, depending on the crystallographic orientation. The strength characteristics of sapphire are structure-sensitive, and this fact explains essential distinctions in the results of measurements performed by different authors. The temperature-dependence [1] of reduced critical chipping stress and the ratio of chipping yield stresses for ruby of 90- and 60-degree orientation are presented in Figs. 2.55–2.57.

Activation energies E and activation bulk V^* depend on the stress τ^* (Fig. 2.58). The temperature dependence of activation energy has two regions: below 1,800 K, where the value of $E^* = 335$–500 kJ/mol, and above 1,800 K, where the value of activation energy grows to 3,350 kJ/mol. Based on the value of activation energy, the character of its dependence on temperature and stresses, one can expect the
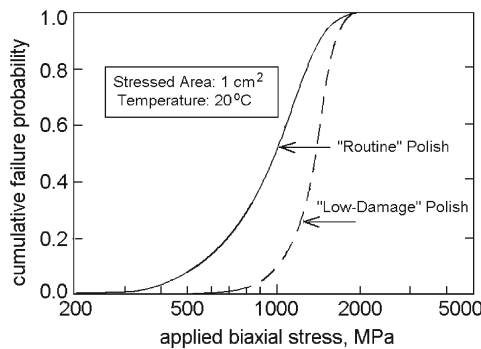
Fig. 2.53 Cumulative failure probability of routinely polished and "low-damage" polished C-plane sapphire
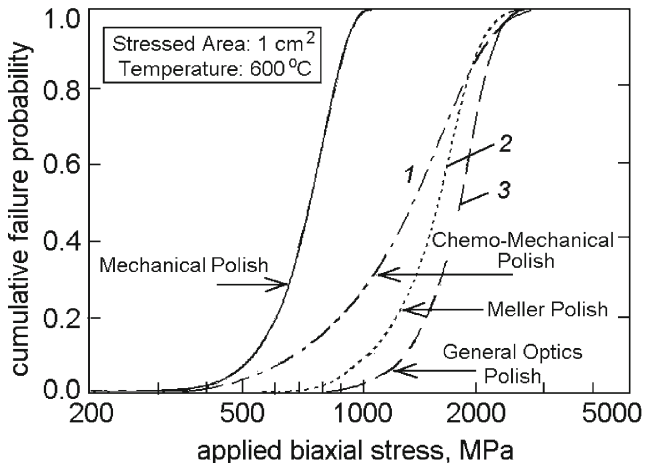
Fig. 2.54 Cumulative failure probability of mechanically and chemical–mechanical polished *C*-plane sapphire. (*1*) Roughness (rms nm) ≥1, measured strength (MPa) 1,082 ± 425, Weibull modulus 2.80 ± 0.42. (*2*) Roughness (rms nm) ≥2.5, measured strength (MPa) 1,330 ± 313, Weibull modulus 4.860 ± 0.31. (*3*) Roughness (rms nm) ≤1, measured strength (MPa) 1,534 ± 18, Weibull modulus 6.07 ± 0.66
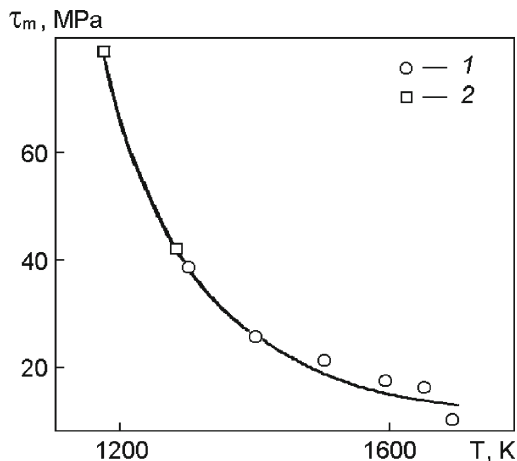
Fig. 2.55 Temperature dependence of reduced yield stress for sapphire: (*1*) tension; (*2*) bending

existence of two mechanisms of plastic deformation in sapphire. At temperatures up to 1,800 K, the thermally activated process of moving over the Peierls-Navarro barriers may take place; at higher temperatures, dislocation creep seems to be more probable.
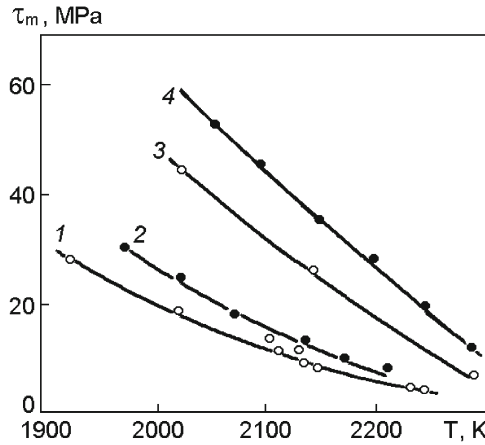
Fig. 2.56 Temperature dependence of critical chipping yield stress (extension rate is $8.7 \cdot 10^{-5}$ c^{-1}): (*1*) sapphire of 60-degree orientation; (*2*) the same, ruby; (*3*) sapphire of 90-degree orientation; (*4*) the same, ruby
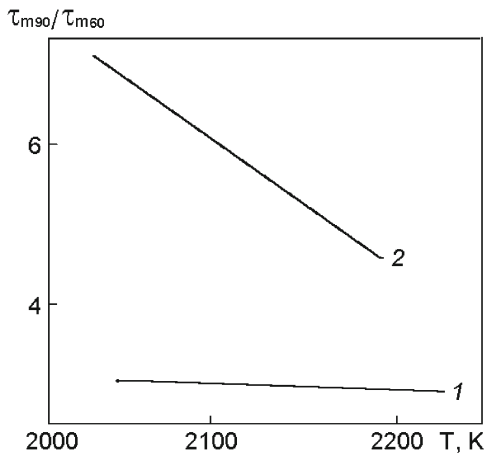
Fig. 2.57 Dependence of the ratio of chipping yield stresses for 90- and 60-degree orientation ruby on temperature and on deformation rate: (*1*) extension rate $8.7 \cdot 10^{-5}$ s^{-1}; (*2*) $5.3 \cdot 10^{-6}$ s^{-1}

2.1.4   *Dynamic Strength of Sapphire*

Understanding the processes of material destruction under high-intensity pulsed loads is of great importance for military, space, and explosion technologies and other primary pulsed energy sources. Collision of high-velocity microparticles (~10 km/s or more) with surfaces gives rise to instantaneous (~10^{-10} s) release of energy

a

E^*, kJ/mol

580

500

420

10   20   30 τ^*, MPa

b

V^*/b^3

160

120

80

40

10   20   30 τ^*, MPa
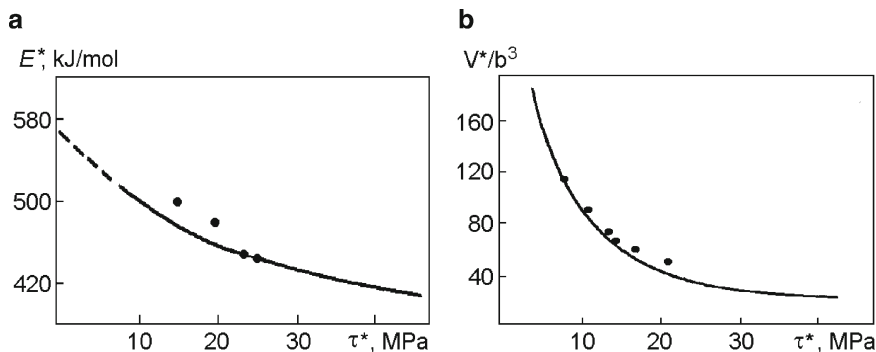
Fig. 2.58 Dependence of the activation energy (**a**) and of the activation bulk (**b**) on stress

on the order of $\sim 5 \cdot 10^7$–$5 \cdot 10^9$ J/kg, or 10–500 eV/atom, within a small volume at the point of impact. There, pressure sharply increases up to ~ 10–100 Mbar, the temperature reaches $\sim 10^5$–10^6 K, and shockwaves arise. The response of solids to shock loading has been studied for more than a century. However, to date the processes that occur under such conditions have not been unambiguously interpreted in terms of physics.

Investigations show that, due to a short period of loading, interaction between separate areas of the surface is practically absent. Within some areas the rate of deformation may be extremely high and the substance may be heated. Under the influence of high-energy action with a velocity exceeding 3 km/s, the transition of metals into the liquid state may occur in the shock zone. The mechanism of plastic deformation also changes. It is found that in metallic single crystals additional slip planes arise, and the contribution of twinning is revealed even in those materials in which deformation twins are not formed under normal conditions [74, 75].

For normal and moderately high deformation rates, the values of ultimate strength and flow limit in solids diminish with heating. Under conditions of submicrosecond shockwave loading, certain metals show athermic behavior of strength characteristics; in some cases these characteristics increase with heating up to T_{m}. Numerical simulation of high-rate deformation of metals by the molecular dynamics method indicates formation of a large number of nonequilibrium packing defects. This obviously results in instability and high mobility of the crystalline structure. In experiments, such an effect manifests itself as temporary loss of material strength caused by shockwaves.

Measurement of crystal lattice deformation at the moment shockwaves pass through is possible. The crystal lattice parameters are determined by the angle of X-ray diffraction. These parameters change as shockwaves pass through the crystal, indicated by oscillation of the Bragg angle.

With shockwave loads (10–100 MPa), the deformation state of a crystal changes from elastic to plastic deformation, i.e., crystals start "flowing." As the period of

shockwave action is very short (approximately a nanosecond), crystal lattice ordering is not violated by the flow of material. However, under such conditions the lattice undergoes isotropic uniform compression, i.e., compression in the direction of wave propagation and in the perpendicular plane. But if the material has acquired the properties of a liquid, Pascal's law comes into force. In actuality, X-ray diffraction experiments usually reveal uniform compression of the crystal lattice in all directions.

Measurements of shockwave-induced crystal lattice deformation in silicon and copper show that these materials have fundamentally different response mechanisms [76]. In particular, at a load of 10–100 MPa, the state of elastic deformation in copper crystals transforms into plastic deformation, while the crystal lattice remains unchanged. Only its isotropic compression in the direction of wave propagation and in the perpendicular direction arises. However, the crystal lattice of silicon is compressed by ~11% in the direction of wave propagation, while no changes occur in the perpendicular direction. Despite pressures exceeding the static flow limit and strong deformation in the longitudinal direction, silicon does not acquire a state of plastic deformation; its response remains completely elastic.

It is known that under the action of increasing loads dislocations in crystals start to move, interact, and generate new dislocations. Macroscopically, dislocation motion is just plasticity of the material. However, transition into the state of plasticity requires a certain period of time that depends on the initial concentration of dislocations and their mobility. As with other covalent crystals, silicon is characterized by extremely low dislocation mobility. Therefore, during short-term action of forces no transition into a state of plastic deformation is observed. For copper crystals the time of transition into the state of plasticity is short (10–100 ps), but nevertheless, under the action of an equivalent shock load copper acquires a hydrodynamic state. For ionic crystals, the density and mobility of dislocations are several orders higher than in covalent crystals, which provide the conditions necessary for crystal transition into the plastic state during the interaction of forces. In general, it is assumed that structural rearrangements in solids under shock compression may last 10^{-9}–10^{-7} s or less.

Shockwave loading is accompanied by an increase in temperature, which depends on the shockwave amplitude. At amplitudes of several tens of GPa, the temperature increment of homogeneous heating is hundreds of degrees. Local heating on the slip lines may exceed the temperature of homogeneous heating. Inhomogeneous heating leads to an essential short-duration loss of strength. Subsequent temperatures decrease through diffusion heat conduction in areas of intense heating and results in recovery of strength properties.

The behavior of elastoplastic materials is characterized by the splitting of shockwaves into elastic (elastic Gugonio precursor) and plastic components. Some experimental methods for studying shear strength are based on the elastoplastic structure of expansion wave and nonhydrodynamic shockwave damping. In modern experimental methods, the space–time profiles of loading and unloading waves are registered by means of fast piezoelectric, piezocapacitance, and piezoresistive transducers.

Among the mentioned experimental methods, one should distinguish the technique for registration of the main normal stresses behind the wavefront. In this case, additional calculations of the medium flow are not required, since the dynamic flow limit is determined as a stress difference.

Destruction is induced by interference of unloading waves. While passing through a material, shockwaves change its microstructure, hardening the material. The processes of hardening and destruction occur simultaneously. Shockwave damping in the material leads to breakage of the interface between the striker and the material, halting the introduction of the striker. Shockwave damping in the striker, caused by an interaction with the side unloading wave, speeds up mass flow by creating a new compression pulse. Destruction of the sample begins with the formation of a channel chip-off crack oriented along the symmetry axis. Such a crack appears due to the focusing of side unloading waves. With subsequent loading the crack itself becomes a source of unloading waves, which leads to the formation of circular coaxial chip-off cracks. The material starts fragmenting, carried out of the contact zone by the striker, and a hollow is formed below this zone. The latent stage of surface destruction ends when, due to geometry, the shockwave reflected by the bottom of the hollow starts passing through the side walls. The reflected pulse, which reaches the face surface near the contact zone, creates a cross crack (face chip-off).

During the past decade, the behavior of brittle materials has been thoroughly investigated. In particular, complete deformation diagrams have been obtained and the different behaviors of ceramics under the influence of shockwaves have been considered. The most significant results achieved in this field are connected with the discovery of destruction waves during shock compression of glasses. The formation of destruction waves is one of the mechanisms of catastrophic strength loss in materials with high hardness, and demonstrates nonlocal response to loading. In ceramics, interatomic bonds may break under shock. The highest resistance to destruction is characteristic of materials with the highest values of dynamic compressibility and dissociation energy.

Systematic investigations of sapphire's response to shock loading started a few years ago. Sapphire products may undergo shock loading in a number of application fields, such as protective windows of environmental detectors, aerospace applications, and so forth. Individual data obtained on randomly chosen samples vary in result, but comparative analysis of the mechanical properties of different glasses and ceramics used as protective materials (Table 2.11) shows that sapphire is superior to all known transparent materials and is on par with ceramic materials employed for protection against bullets and shell splinters.

Presented below are results of an experimental check of sapphire's response to shock loads taking into account the samples' history, which includes their structural perfection (dependent on the growth method) and prior chemical-mechanical or thermal treatments. An attempt was made to establish a relationship between the behavior of the material and its grain structure. The shock load values were chosen based on practical requirements of sapphire screens and windows to withstand shocks with an energy of 6–8 J. These investigations were carried out on sapphire

Table 2.11 Mechanical characteristics of protective materials

Material	Density (g/cm³)	Flexural strength (MPa)	Microhardness (GPa)	Fracture toughness (MN/m$^{3/2}$)
B₄C (opaque)	2.5	410	32	2.5
Si₃N₄ (opaque)	2.35	800	15.8	6
SiC (opaque)	2.35	400	28	3–4
ALON (clear)	3.69	380	18	2
Sapphire (clear)	3.97	760	20	4
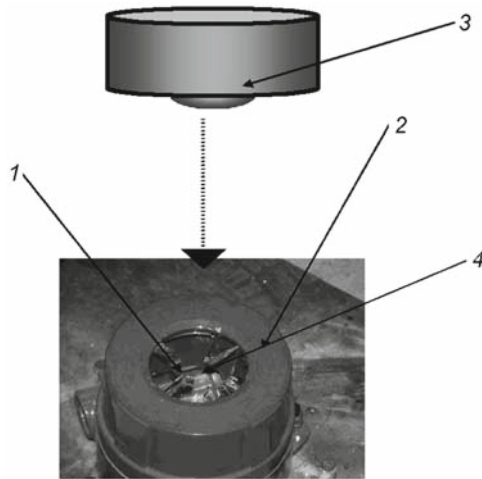
Fig. 2.59 Schematic of shock testing (*1*) sapphire sample; (*2*) fixing of the sample; (*3*) falling ball; (*4*) cracks formed at testing

cylinders with a diameter of 75 mm and thickness of 4.6 mm, and on 78 × 78 × 4.6 mm plates, made from crystals grown by the HDS, Kyropoulos, and Stepanov methods. The surfaces C, A, and R were polished to 120/100, 60/40, and 40/20. The tests were performed in accordance with standard requirements with the shock energy varied from 4 to 10 J (Fig. 2.59).

It is known that the maximum rate of loading transfer through any material is equal to the velocity of sound in this material, specifically $(E/\gamma)^{1/2}$, where E is the Young's modulus and γ is the density of the material. The velocity of sound in sapphire, the rate of shock loading transfer, may reach $(1.04–1.12) \cdot 10^4$ m/s, which considerably exceeds the velocity of a bullet (300–850 m/s). As a general rule, the action of shock loading lasts approximately a hundredth of a second, and the period of energy withdrawal from the point of shock is by several orders faster. At the instant of shock, a series of stress waves emanate from the point of shock. The waves reach the boundaries of the sample or blocks, twin interlayers, or so on, and
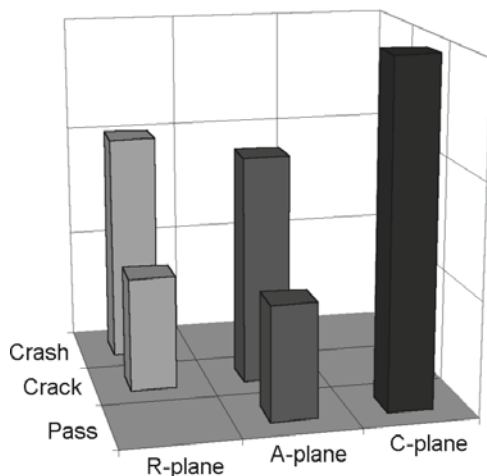
Fig. 2.60 Behavior of sapphire with different orientations during shock testing. The maximum shock energy is 7 J

are reflected, diminishing their intensity slightly. Superimposition of the direct and reflected waves results in the formation of standing waves, which may give rise to a sharp increase of stresses in the antinodes and to destruction of the sample. So, the progress of events is defined by processes that depend on the shape and size of the sample, the place of shock, and the structural perfection and orientation of the crystal.

Figure 2.60 shows the strength comparison of sapphire samples of different crystallographic orientations grown by the same method. Practically all samples with the (0001) orientation subjected to a special thermal treatment withstand three to five shocks of up to 7 J. The *R*-oriented samples are destroyed after the first shock, and only a third of the (11$\bar{2}$0) orientation samples survive tests carried out under the same conditions.

It is known [77] that the size of grain structure elements in sapphire, a_e, and the properties connected with them depend on the growth method (see Fig. 2.61). Samples grown by different methods and subjected to different annealing regimens have fundamentally different values of a_e. A positive correlation exists between strength and a_e, and the previously obtained dependence $k_c(a_e)$ [77] has the same tendency, i.e., the larger the value of a_e, the greater the cracking resistance. It may be assumed that due to large values of a_e and the "density" of their boundaries, the waves emanating from a point of shock do not propagate over the whole of the sample's bulk, but are partly reflected from the grain boundaries. In this case, a part of the shock energy is scattered, and the standing waves formed in the antinodes will not have the energy sufficient for destruction of sapphire. With other conditions being equal, samples with a high-quality polish exhibit the highest strength (Fig. 2.62).
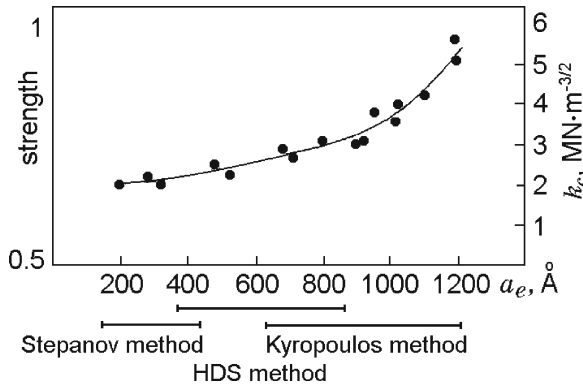
Fig. 2.61 Dependence of the relative strength and cracking resistance of sapphire crystals grown by different methods on the size of their grain structure elements
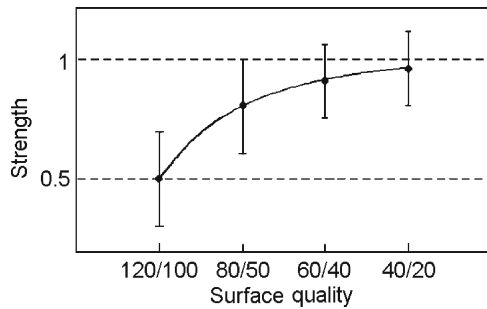
Fig. 2.62 Dependence of sapphire strength on surface quality

The depth of the defective layer formed on the surface of sapphire during mechanical treatment depends on the crystal growth method and on the grain structure, with other conditions being equal. For instance, crystals grown by the Verneuil and Stepanov methods have small grain structure elements, the depth of their defective layer is the largest, and their relative strength and cracking resistance during shock loading are the lowest (Fig. 2.63a).

In sapphire crystals, which have ~20% covalent bonds, all the destruction types are observed: brittle failure, plastic flow (preceding destruction), and chip-off. At centric impact, brittle failure may be observed in the center of the sample, but destruction of the periphery zones is not excluded (Fig. 2.63b).

The value of failing stress at chip-off is shown to depend on the shape and duration of tensile stress pulses, the stress-strain state of the medium, and different physical factors such as temperature, initial microstructure, and so forth. Thus, chip-off strength is a function of many variables. The energy criterion for chip-off destruction is based on the work required for chip-off in the region of dilatation
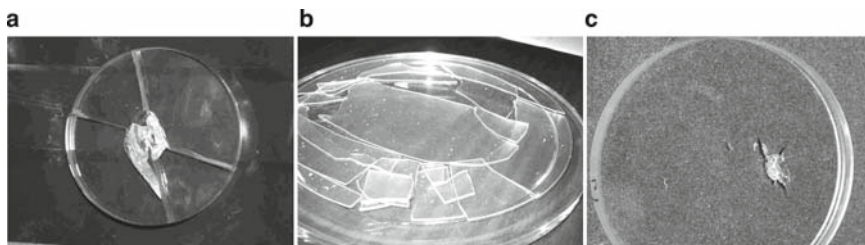
Fig. 2.63 (**a**) Centric impact. Brittle failure in the center of the sample. (**b**) Centric impact. Destruction of the periphery areas of the crystal. (**c**) Centric impact. Chip-off in the periphery of the sample
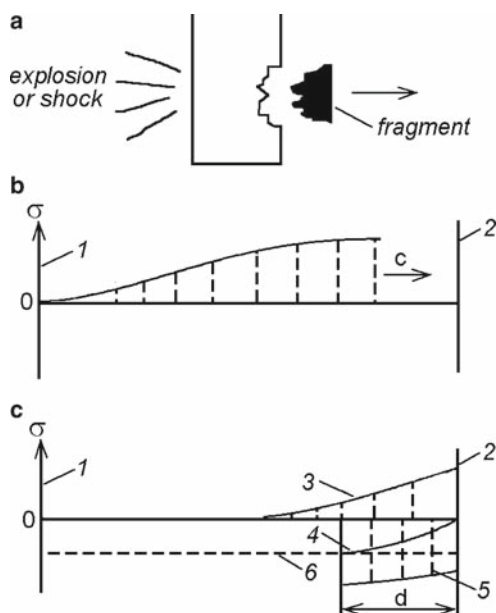
Fig. 2.64 Schematic of (**a**) chip-off, (**b**) pulse propagation, and (**c**) profiles of stresses arising with a shock: (*1*) sample's surface subjected to shock; (*2*) back side of the sample; (*3*) compression stress profile; (*4*) resulting profile; (*5*) stretching stress profile (reflected wave); (*6*) critical breaking stress; d ($\leftrightarrow$) distance between the surface and the place of breaking

wave interaction and is accomplished at the expense of elastic energy in the stretching pulse. Chip-off will occur if the elastic energy is sufficient for realization of this process.

To understand the mechanism of chip-off [75], one should consider the compression stress pulse that passes through a tested sample in consequence of shock (Fig. 2.64). The compression wave (Fig. 2.64b) reaches the free surface of the sampleand is reflected as a stretching wave. The reflected stretching wave then interacts with the incident compression wave (Fig. 2.64c). At a distance d from the back surface

of the sample, the resulting stretching stress becomes equal to the critical normal breaking stress, the material breaks, and a piece of it separates from the surface. Thus, chip-off occurs exclusively due to wave effects.

The described progression of destruction also is observed in rectangular plates. As a rule, the angular zones are the first to be broken.

Plastic flow of sapphire under shock loading has been revealed. On the sapphire surface, a sharp deformation relief is formed at the point of shock (Fig. 2.65).

Earlier, similar patterns of deformation relief caused by plastic flow were observed only with diffusion welding of sapphire at $T > 2,200$ K and high specific pressures. The size and character of the deformation relief depend on the orientation of the sample (Fig. 2.66). Samples of (0001) orientation have a symmetrical trace of shock on the surface and their deformation relief is sharp. The shock energy is spent mainly on the formation of such a relief, i.e., on plastic flow of the material. Therefore, crystals with the (0001) orientation usually withstand shocks better (Fig. 2.66a). In R-oriented crystals plastic flow is extremely faint (Fig. 2.66b). In many cases it is not revealed at all, and the applied shock energy leads to destruction of the crystal. The behavior of orientation A is intermediate between the C and R orientations. An essential share of shock energy may be spent on plastic flow of the surface at the point of shock and such crystals may withstand shock loading.

Such an analysis of experimental facts yields the following conclusions:
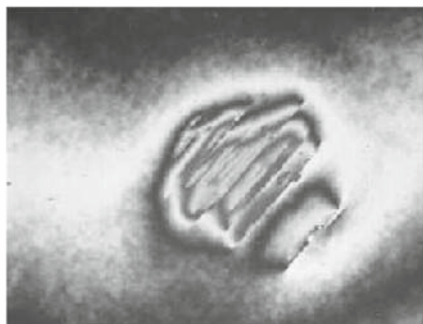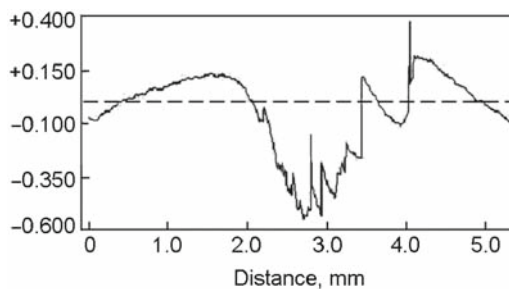
Fig. 2.65 Deformation relief formed on the surface at the point of shock. Centric impact. Brittle failure at the place of shock. The study was performed by means of the Zago apparatus
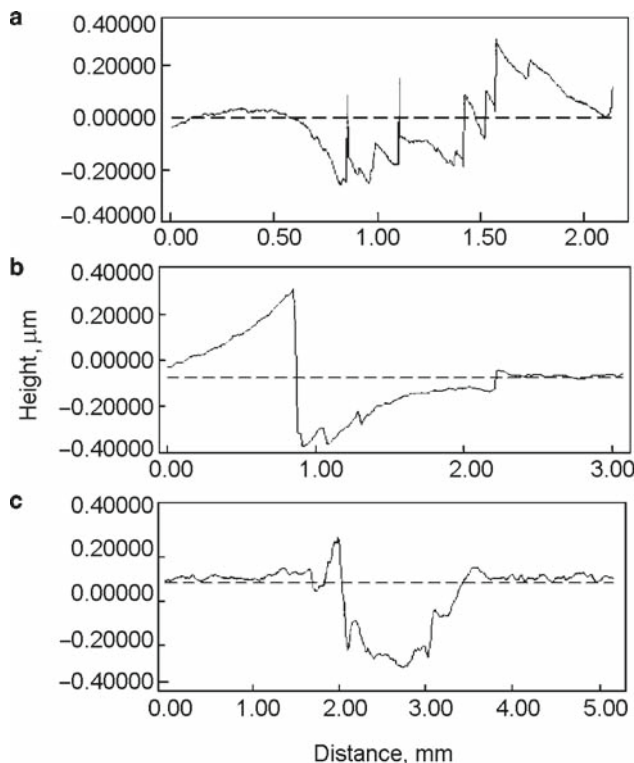
Fig. 2.66 Deformation relief formed on the surface of the crystals with the orientation (**a**) C (0001), (**b**) $R(10\bar{1}2)$, (**c**) $A(11\bar{2}0)$

- The behavior of sapphire can be predicted only by comparing the kinetic shock energy with the interatomic and intermolecular bond energies
- The physical–mechanical parameters of sapphire, such as Young's modulus, compressive and tensile strengths, Poisson's ratio, shock viscosity, and so forth, are only structural characteristics that lose their physical sense during the material's transition into the plastic state under shock loading
- The strength of sapphire under shock loading depends on the method of crystal growth and annealing, the crystallographic orientation, and the surface quality
- The dependence of sapphire strength on the crystal growth method is defined by the substructure of the crystals
- The values of cracking resistance and shock strength of sapphire are correlated
- At the point of shock plastic flow of sapphire occurs, and a sharp deformation relief is formed
- Shock loading of sapphire gives rise to all types of destruction: brittle failure, plastic flow which precedes destruction, and chip-off
- Special, high-temperature treatment fundamentally raises the shock strength of sapphire

2.1.5   Thermal Properties

Melting temperature is 2,323 K.
Boiling temperature is 3,253 K.
Linear expansion coefficient of sapphire (α) depends on temperature and orientation (Fig. 2.67) [78]. Like other thermal parameters established by different authors and presented in catalogues, the values of α differ significantly.

The most often used values of the linear expansion coefficient:

$\perp C$	293–323 K	$5.0 \cdot 10^{-6}$ K^{-1}
$\|C$		$6.6 \cdot 10^{-6}$ K^{-1}
60° orientation	293–323 K	$5.8 \cdot 10^{-6}$ K^{-1}
$\perp C$	1,273 K	$(7.9–8.3) \cdot 10^{-6}$ K^{-1}
$\|C$		$(8.8–9.0) \cdot 10^{-6}$ K^{-1}
60° orientation	1,273 K	$7.7 \cdot 10^{-6}$ K^{-1}

At room temperature (295.65 K) the linear extension coefficients for the lattice constants are: $\alpha_a = 5.22 \cdot 10^{-6}$K^{-1}; $\alpha_c = 5.92 \cdot 10^{-6}$K^{-1}.

The investigation of thermal extension of sapphire in the region of low temperatures, which appears to be topical in view of this materials use in superconducting resonators, shows that below 50 K α is lower than 10^{-7} K^{-1} [79], and this value is negligible in most cases. However, impurities may give rise to low-temperature anomalies. For example, ruby with the magnetic impurity Cr^{2+} has an anomaly of temperature expansion caused by the Yan-Teller effect. Anomalies also discovered in sapphire with deviations from the stoichiometric content [80]. The results of the thermal expansion study of a sample with an anionic vacancy content of 10^{18} cm^{-3} (10^{-3}%) are shown in Fig. 2.68. The measurements were carried out using a capacitance dilatometer on a sample with 16 mm diameter and 100 mm width.

The values of a are determined in 17–115 K temperature interval with $\pm 2 \cdot 10^{-8}$ K^{-1} error at $T > 50$ K and with $\pm 5 \cdot 10^{-9}$ K^{-1} error at $T < 50$ K. Thermal expansion of
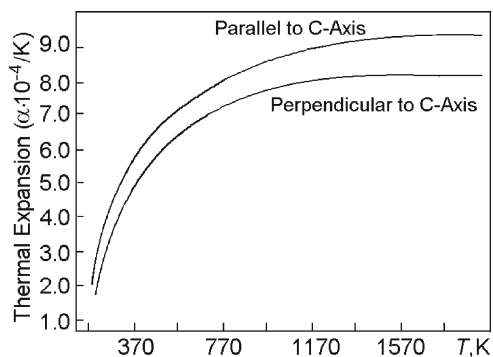
Fig. 2.67 Temperature dependence of the linear expansion

$$\alpha \cdot 10^{-8}, \text{K}^{-1}$$
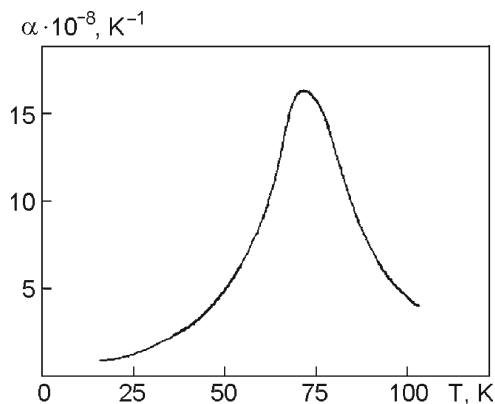
Fig. 2.68 Expansion of sapphire with anionic vacancies in the low temperature region. The sample is oriented along the axis [10$\bar{1}$0]

sapphire with anionic vacancies at $T < 100$ K turns out to considerably exceed that of the stoichiometric crystal. The value of α reaches its maximum of $16 \cdot 10^{-8}$ K^{-1} at 70 K.

Sapphire is a universal reference standard material for thermal expansion. The sapphire reference standards used in high-temperature comparative dilatometers with the kinematic polycrystalline corundum system must have thermal expansion equal to that of corundum polycrystals. Such reference standards are made from sapphire rods with $d = 6$ mm and having the rod axis oriented at an angle of $59 \pm 2°$ with the C-axis. Accurate values of the relative extension and the differential temperature coefficient of linear expansion are contained in Table 2.50 [81].

Thermal conductivity coefficient (λ_T) of sapphire also depends on the temperature and the orientation. The temperature dependences of sapphire and ruby λ_T are presented in Figs. 2.69 and 2.70, the temperature-dependence of thermal conductivity λ_T, W/(m K) (q) and of thermal resistance (W) are shown in Figs. 2.71 and 2.72.

The most often used values of the thermal conductivity coefficient are the following:

- At 298 K $\perp C$: 30.3 W/(m K)
           $\|C$: 32.5 W/(m K)
- At 273 K 60° orientation 46.06 W/(m K)
- At 373 K 60° orientation 25.12 W/(m K)
- At 673 K 60° orientation 12.56 W/(m K)

Thermal conductivity of sapphire at T_m, obtained by extrapolation is equal to 3.4 W/(m K), the ratio of thermal conductivity of sapphire to that of its melt $\lambda_{sol}/\lambda_{liq} = 1.65$.

λ_T, W/cm·K λ_T, W/cm·K
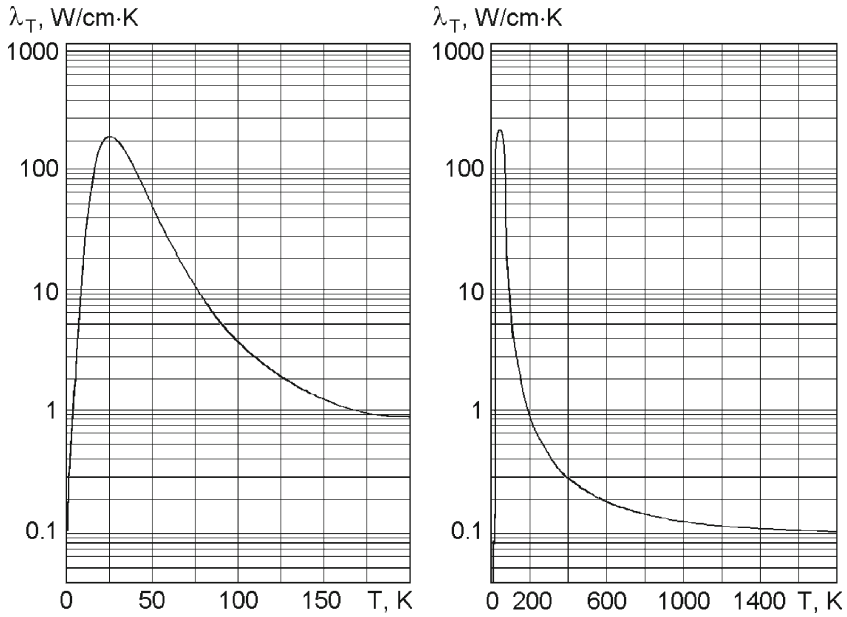
Fig. 2.69 Temperature dependence of the thermal conductivity coefficient for sapphire: (**a**) low temperatures; (**b**) high temperatures

λ_T, W/m·K
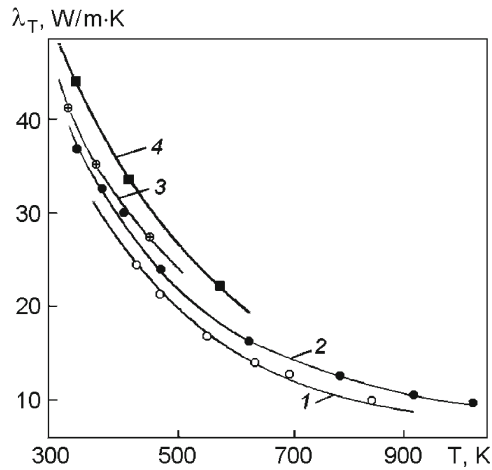
Fig. 2.70 Temperature dependence of the thermal conductivity coefficient for ruby with varying chromium content: (*1*) 1.1%; (*2*) 0.75%; (*3*) 0.16%; (*4*) 0.003%
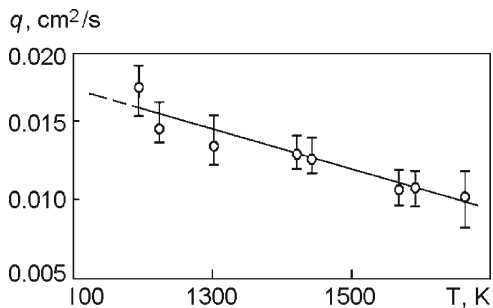
Fig. 2.71 Temperature dependence of thermal conductivity
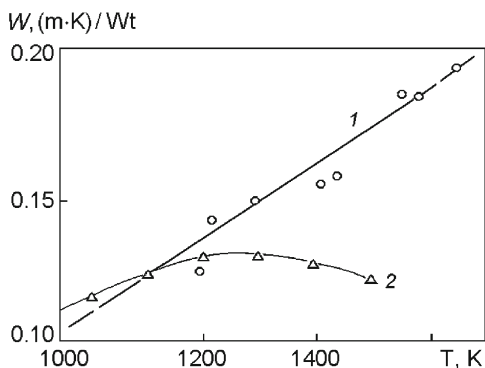
Fig. 2.72 Temperature dependence of thermal resistance: (*1*) calculated data; (*2*) experimental data

Specific heat of sapphire (c_p) at 293 K: 0.181–0.187 cal/(g K), at 1,273 K: 0.300 cal/(g K).

Specific heat of sapphire at low temperatures:

T (K)	10	25	50	100	150	200	298.1
c_p (kJ/(kmol K))	0.04	0.20	1.9	13.4	33.5	51.92	79.13

Molar heat capacity ($c_{p\lambda}$) at 293 K: 18.63 cal/(mol K), at 1,273 K: 29.86 cal/(mol K).

The temperature dependences of specific heat and molar heat capacity are shown in Fig. 2.73 and 2.74. The numerical values for thermal conductivity and heat capacity of ruby versus temperature are given in Table 2.51.

Molar heat capacity (kJ/(mol K) can be estimated in the 298–2,300 *K* temperature interval by means of the following dependence:

$$c_{p\mu} = 4.2(26.12 + 4.388 \cdot 10^{-3} T - 7.269 \cdot 10^{5} T^{-2}).\qquad(2.7)$$
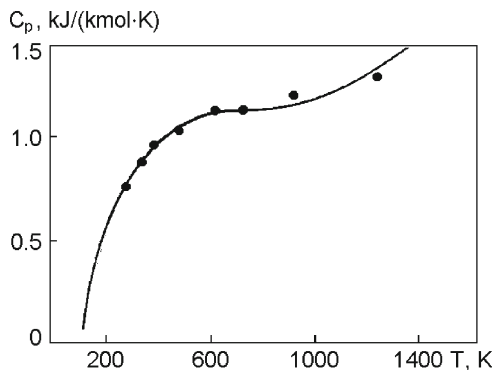
Fig. 2.73 Temperature dependence of specific heat
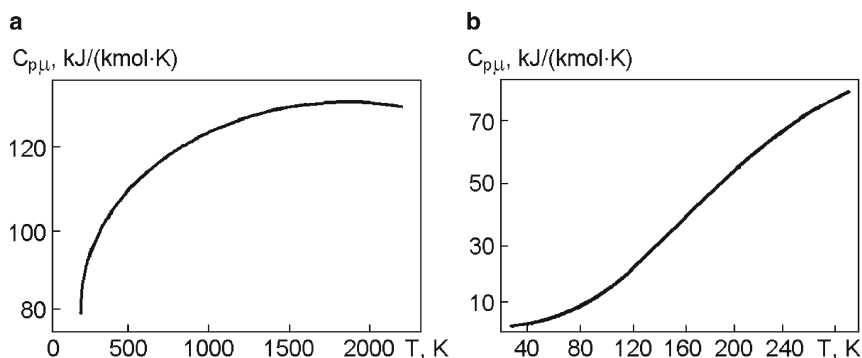
Fig. 2.74 Temperature dependence of molar thermal capacity: (**a**) high temperatures; (**b**) low temperatures

Presented below are the values of some thermodynamic parameters of Al_2O_3 at room temperature and melting temperature:

$$\Delta H_{298} = 1,671,000 \text{ kJ/mol}; \quad \Delta F_{298} = 157,800 \text{ kJ/kmol};$$
$$\Delta S_{298} = 51 \text{ kJ/(kmol K)}; \quad \Delta H_m = 108,900 \text{ kJ/kmol}.$$

The temperature dependence of the thermodynamic parameters of sapphire is given in Tables 2.52, 2.54, and 2.56. Since the processes that occur at attenuation of sound waves have the same character as those defining thermal resistance, Table 2.53 presents the temperature dependence of the sound absorption coefficient for ruby.

Coefficients of diffusion of Cr^{3+} and Fe^{3+} in sapphire and in ruby (0.5 mass% of Cr) are temperature-dependent (Table 2.12) [82]. The coefficient of oxygen diffusion in sapphire is $4.2 \cdot 10^{-20}$ cm² s⁻¹ at 1,473 K [83]. That is, the diffusion path of

Table 2.12 Cr^{3+} and Fe^{3+} diffusion coefficients in sapphire and in ruby

	Diffusion coefficients ($cm^2 s^{-1}$)			
	Sapphire		Ruby	
T (K)	Cr^{3+}	Fe^{3+}	Cr^{3+}	Fe^{3+}
1,473	$3.64 \cdot 10^{-14}$	$2.54 \cdot 10^{-14}$	$5.81 \cdot 10^{-14}$	$3.73 \cdot 10^{-14}$
1,523	$7.97 \cdot 10^{-14}$	$6.77 \cdot 10^{-14}$	$1.11 \cdot 10^{-13}$	$1.09 \cdot 10^{-13}$
1,573	$2.94 \cdot 10^{-13}$	$2.05 \cdot 10^{-13}$	$3.24 \cdot 10^{-13}$	$3.16 \cdot 10^{-13}$
1,623	$4.43 \cdot 10^{-13}$	$3.70 \cdot 10^{-13}$	$6.94 \cdot 10^{-13}$	$5.17 \cdot 10^{-13}$

oxygen does not exceed 2.5 Å/h. In the temperature interval from 1,853 to 2,113 K for ^{16}O the diffusion coefficient is $1.56 \cdot 10^{-10}$ m^2 s^{-1} [84], the activation energy being equal to 788 ± 29 kJ/mol.

The dependence of diffusion on crystallographic direction has been studied insufficiently. It has been reported [85] that ^{22}Na diffusion along the *C*-axis is almost twice as high as along the perpendicular direction.

Implantation of ions into a sapphire surface and evolution of the surface-adjacent layer upon thermal treatment. Ions of metals and gases, including those which implantation into the surface-adjacent sapphire layer during the growth process is either impossible or difficult, can be introduced by ionic bombardment. Ions of Mn, Ni, Cr, Xe, and so forth are implanted at temperatures from −170 up to 250 K. The doses vary from $3 \cdot 10^{16}$ to $5 \cdot 10^{17}$ ions/cm², the density of ionic current is lower than 2.5 mA/cm² for doses not exceeding $1 \cdot 10^{17}$ ions/cm², and the ion energy is 300 keV to 1 MeV. The implantation depth reaches several thousand Å. Upon deep implantation the surface layer becomes amorphous. The degree and depth of surface damage depend on the implantation energy. In particular, the critical dose for sapphire amorphous-phase transition is ~$2 \cdot 10^{15}$ ion/cm² for 150 keV Cr ions implanted at ~77 K or 300 keV Ni ions implanted at ~100 K. For 400 keV Xe ions the critical dose is $3 \cdot 10^{16}$ ions/cm² [86]. During postimplantation annealing at 873–1,873 K the damaged surface-adjacent layer recrystallizes. The process of annealing is accompanied with migration and redistribution of the implanted ions.

Unlike Mn, Ni, or Xe ions, trivalent Cr, Ga, and Fe ions can be incorporated into the aluminum sublattice upon annealing in air. At 1,473 K all Cr^{3+} ions enter the sublattice and further migration of ions is not observed.

2.1.6 Electrical Properties of Sapphire

At room temperature sapphire is one of the best dielectrics. The character of electric conduction (χ) is described by the equation:

$$\chi = \chi_1 \exp(-E_1^* / kT) + \chi_2 \exp(-E_2^* / kT) \tag{2.8}$$

where E_1^* and E_2^* are the activation energies of charge carriers. The activation energies of low- and high-temperature conduction are 2.25 and 5.50 eV, respectively. Electrical resistance (ω) is temperature-dependent (Table 2.13).

Table 2.13 Temperature dependence of electrical resistance

T (K)	ω (Ω m)	T (K)	ω (Ω m)
293	$1 \cdot 10^{14}$	973	$2.5 \cdot 10^7$
373	$2 \cdot 10^{13}$	1,073	$3.5 \cdot 10^6$
473	$4 \cdot 10^{12}$	1,273	$1 \cdot 10^6$
573	$1.1 \cdot 10^{11}$	1,373	$4 \cdot 10^5$
673	$1.6 \cdot 10^{10}$	1,473	$4 \cdot 10^4$
773	$1.3 \cdot 10^9$	1,773	$2 \cdot 10^3$
873	$1.9 \cdot 10^8$		

In catalogues of different sapphire producers other data can be found. For instance, the bulk resistance at 298 K has been reported to be equal to 10^{14} Ω cm, which coincides with the magnitude contained in Table 2.13, whereas in other catalogues the said value is 10^{16} Ω cm. For 773 and 1,273 K temperatures values of ω equal to 10^{11} and $10^6 \Omega$ cm, respectively, are reported. It should be noted, however, that at present one cannot persuasively claim that these data are correct.

Resistivity of sapphire (Ω cm)	
293 K	$\perp C$: $5.0 \cdot 10^{18}$
	$\|C$: 1.3–$2.9 \cdot 10^{19}$
773 K	$>10^{12}$
1,273 K	$>10^9$

The value of resistivity diminishes with increasing temperature, as with other oxides (Fig. 2.75) [87]. The electrical conduction value abruptly changes from 10 to 0.03 Ω^{-1} cm^{-1} at the liquid to solid phase transition.

At 1,573–2,023 K the behavior of sapphire and polycrystalline aluminum oxide is similar to that of p-type semiconductors at high pressures of oxygen and of n-type semiconductors at low pressures [88]. At high temperatures, the type of electrical conduction in sapphire varies depending on the partial pressure of oxygen in the surrounding atmosphere (Fig. 2.76) [89].

The change in mechanisms of electrical conduction is explained by the theory of high temperature thermochemical processes, when the crystal is in equilibrium with the vapors of crystal-forming components. In the state of high-temperature equilibrium with low partial pressures of oxygen, donor-type defects are predominantly formed, whereas at high pressures acceptor-type defects arise. In both cases a
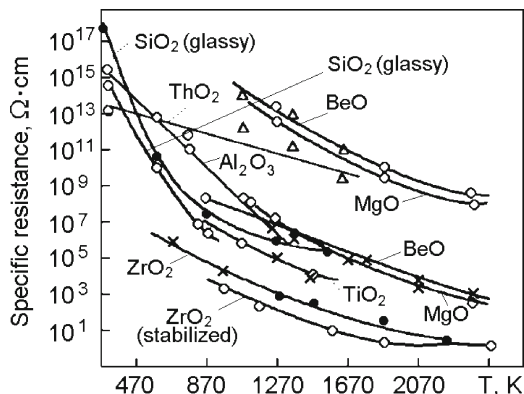
Fig. 2.75 Temperature dependence of resistivity for Al$_2$O$_3$ and some other oxides
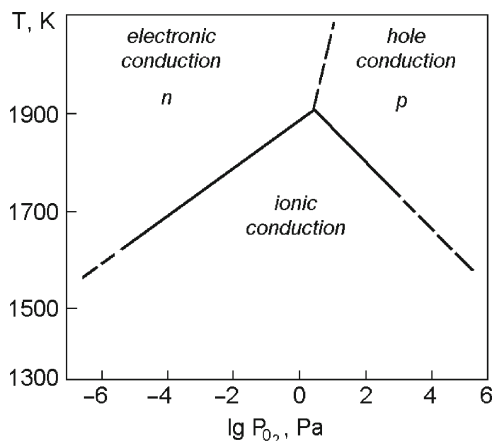
Fig. 2.76   Mechanisms of electrical conduction of sapphire

deviation from stoichiometric content of Al$_2$O$_3$ occurs. At medium partial pressures of oxygen no deviation from stoichiometry should be expected, perhaps in addition to the formation of donors, acceptors, and associates.

Irradiation of sapphire changes its electrical conduction [90]. Upon irradiation with doses up to 0.1 MGy the value of electrical conductivity decreases, whereas at higher doses (>1 MGy) the primary value of electrical conduction is almost restored (Fig. 2.77) [91, 92].

Dielectric constant of sapphire at 298 K in 10^3–10^9 Hz interval is

$$\|C \qquad 11.5$$
$$\perp C \qquad 9.3$$
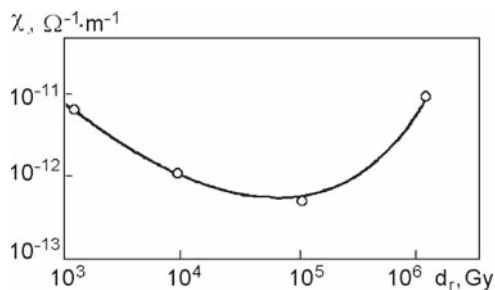
Fig. 2.77 Dose dependence of the value of electrical conduction for sapphire
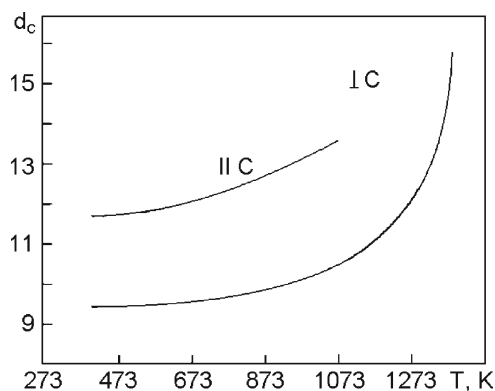
Fig. 2.78 Temperature dependences of the dielectric constant in the directions parallel and perpendicular to the optical axis

(In some catalogues the value of the dielectric constant at $1 \cdot 10^2$–$3 \cdot 10^8$ Hz frequencies in the direction $\parallel C$ is 10.55, in the direction $\perp C$ it is equal to 8.6.) The value of the dielectric constant increases with temperature irrespective of the crystallographic orientation (Fig. 2.78).

*Tangent of dielectric loss angle (*tg δ) is the same in the directions parallel and perpendicular to the optical axis. For a frequency of 1.0 MHz it is equal to $1 \cdot 10^{-4}$; for higher frequencies tg $\delta < 1 \cdot 10^{-4}$. At 298 K and frequencies up to 10^{10} Hz, tg δ in the direction parallel and perpendicular to the C-axis it essentially differs:

$$\perp C: \quad 3.0 \cdot 10^{-5}$$
$$\parallel C: \quad 8.6 \cdot 10^{-5}$$

Dielectric losses in sapphire are temperature-dependent (Figs. 2.79 and 2.80). For comparison, this figure also presents the temperature-dependence of tg δ in γ-irradiated sapphire (the irradiation dose is 10^4 Gy).
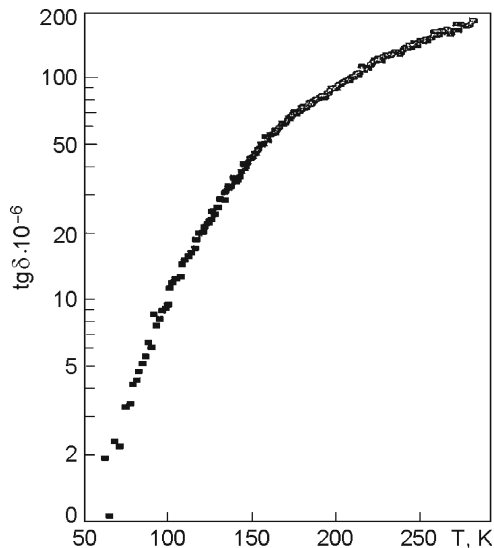
Fig. 2.79 Dielectric losses at low temperatures and 145 GHz
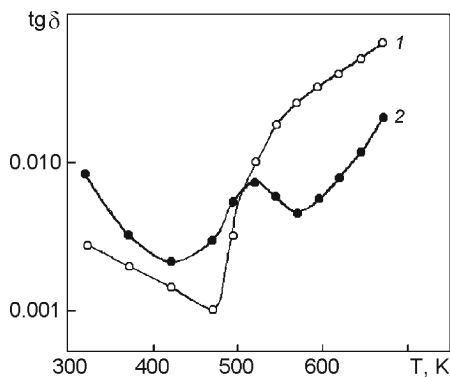
Fig. 2.80 Temperature dependences of tg δ in the initial (*1*) and irradiated crystals (*2*)

    As is seen, the value of dielectric loss increases in the region of low temperatures
and diminishes as temperature rises. In the 293- to 430-K interval, the frequency
dependence of tg δ is more pronounced than its temperature dependence. Figure
2.81 presents the frequency dependences of tg δ at different temperatures for nonir-
radiated sapphire (a) and for sapphire irradiated by a 10^4 Gy dose (b). The observed
nonlinear behavior of the frequency dependence of tg δ is supposed to be caused by
polarization processes in sapphire.
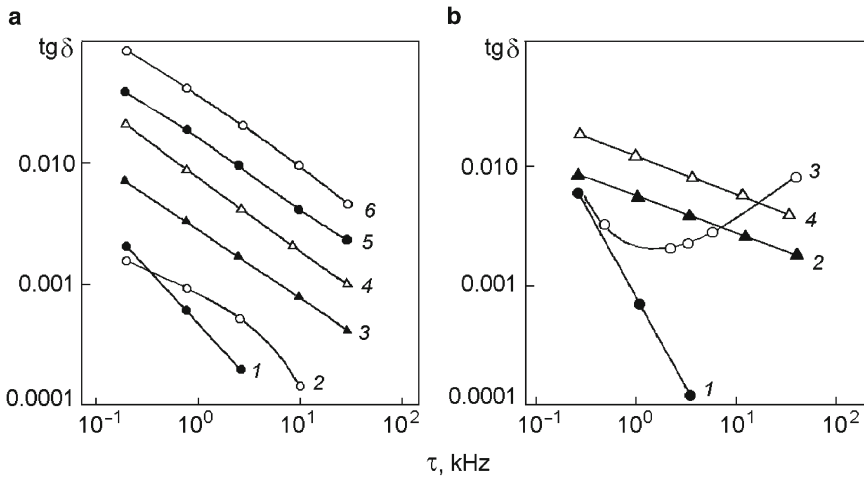
Fig. 2.81 Frequency dependences of tg δ at temperatures for (**a**) nonirradiated and (**b**) irradiated sapphire: (*1*) T = 323 K; (*2*) 432 K; (*3*) 523 K; (*4*) 573 K; (*5*) 623 K; (*6*) 673 K

Magnetic susceptibility of sapphire:

$$\|C: \quad 0.21 \cdot 10^{-6}$$
$$\perp C: \quad 0.25 \cdot 10^{-6}$$

2.1.7 Laser Properties

Sapphire acquires laser properties after the introductio n of activating additives. It should be noted that the crystal can be used as a laser medium only in the case of isomorphic substitution of aluminum.

The coefficient of activator distribution, K_d, is dependent on the thermodynamic parameters of the matrix-activator system and the growth conditions (Table 2.14). It is difficult to calculate K_d taking into account thermodynamic and kinetic factors. This value can be estimated within the framework of the energy theory of isomorphism by the relation [93]:

$$\text{In } K_d = \Delta H_m / R_g (T_c^{-1} - T_m^{-1}) - Q_s / R_g (1.2T_c^{-1} - t_i) \tag{2.9}$$

where ΔH_m is the melting heat, R_g is the gas constant, T_c is the crystallization temperature of the mixture, T_m is the melting temperature of the activator, t_i is an empirical constant, and Q_s is the energy of mixing for the solid solution. The introduction of large-size cations (Sc, Ln) into sapphire considerably diminishes the distribution coefficient.

Table 2.14 Presents estimates of K_d for different activators, as well as a comparison of K_d with experimental values K_{de}

Ion	T_m of oxide (K)	r/r_1*	Q_s (kcal/mol)	Q_l (kcal/mol)	K_d	K_{de}
Cr^{3+}	2,538	0.042	15.9	−3.2	0.30	0.4
Fe^{3+}	–	0.063	35.7	−7.1	0.05	0.01
Ga^{3+}	2,013	0.048	20.6	−4.1	0.18	0.05
Sc^{3+}	2,750	0.106	101	−20.2	0.0002	0.005

*r/r_1 is relative difference of interatomic distances; Q_l is the shift energy for oxides with Al_2O_3 in liquid phase

Among Al_2O_3-based laser media, the most widespread are $Cr:Al_2O_3$ and $Ti:Al_2O_3$. The application fields of these materials are considered in Chap. 1.

$Cr:Al_2O_3$. Ruby has the following advantages as an active medium [94, 95]: high pulse power; possibility of operation at room temperature; the highest mechanical strength compared with other laser media; good photochemical resistance to pump source radiation; and high threshold of surface and bulk damage under the influence of its own radiation. The characteristics of ruby as a laser medium are given in Table 1.11.

Ruby efficiently absorbs pump lamp emission in the blue and green regions of the spectrum. Ruby laser emission can be registered by low-inertia vacuum photoreceivers. In the region of ruby element radiation, such photoreceivers possess high sensitivity and stability. In this connection, ruby lasers compare favorably with more efficient lasers in the threshold location of objects upon laser illumination. At the same time, the threshold of excitation and generation of ruby is higher than with four-level active media.

Optical strength. Surface damage of sapphire (chips or cracks) and bulk damage (stars or tracks) may occur immediately at the onset of laser irradiation. The threshold of surface damage depends on the quality of the surface and usually is lower than the threshold of bulk damage. Microcracks in the surface layer and even edge bevels can focus laser irradiation. Another cause of damage is radiation absorption by abrasive particles contained in the surface-adjacent layer.

For short pulses the threshold damage power is inversely proportional to the duration of irradiation, t_p. For long-duration pulses the damage threshold does not depend on t_p. The location of the transitional region depends on surface structure. For quasiamorphous and crystalline surfaces, the dependence behavior changes at $t_p = 5 \cdot 10^{-6}$ s and $t_p = 2 \cdot 10^{-6}$ s, respectively. The surface-adjacent layer absorbs ~10% of the laser pulse energy. In a 1-μm thick layer, a pressure of ~200 N/m² is created when the radiation power density is 0.5 GW/cm² and $t_p = 30$ ns, leading to "microexplosion."

The strength of sapphire crystal ends can be increased by diminishing the depth of the defective surface-adjacent layer. In particular, for thicknesses of 5, 2, 0.03,

and 0 μm, the surface damage threshold (in relative units) is 0.47; 1.0; 2.5, and 4, respectively.

To a lesser extent, the surface damage threshold depends on crystal orientation. Rotation of the crystal end plane by 90° with respect to the vector of laser beam polarization does not influence the damage threshold for the basal plane, but for the prism plane this value changes by 1.3–1.5 times. Such a difference is explained by redistribution of polarized radiation between microcracks, developing mainly in the direction of the C-axis, and by other defects of the surface-adjacent layer.

When irradiation intensity is close to the threshold density of the surface evaporation energy, the main damage mechanism for the output surface becomes evaporation in the regions of local energy maxima. Estimation of the threshold evaporation energy of an output end, when irradiated by a monopulse ruby laser with a power density of 0.5 GW/cm² and t_p = 30 ns, indicates an energy density threshold equal to 20 J/cm². The output end usually is destroyed at lower powers versus the input end.

As a rule, volume damage in ruby takes place at irradiation energy densities higher than 0.7 J/cm², due to absorption of the radiation by inclusions and other absorbing defects, or to self-focusing of the radiation. A significant part of the energy is absorbed by Cr^{4+} ions and impurities, some of which change their phase state under irradiation. The volume of the phase also changes, leading to additional volumetric stresses. Besides passive absorption, some impurities (e.g., Mg^{2+}) diminish the output energy as the number of pulses increase. Upon strong excitation, titanium impurities lead to the formation of stable color center (CC) and decrease the bulk strength.

Bulk strength also may be reduced due to the initial or pumping-induced optical inhomogeneity of RE, leading to nonuniform energy distribution over the element's cross section and to damage in zones subjected to the most intense irradiation. High-power lasers use either highly homogeneous rubies (grown by the Czochralski method) or an optical design in which the beam repeatedly passes through different regions of the active body during generation.

The influence of pores on the bulk strength is not significant. Obviously, regions containing pores do not participate in the process of generation and have low local energy densities.

Bulk damage may give rise to destruction of the crystal ends. For a pulse energy of 0.2 J and t_p = 30–70 ns, the first Fresnel diffraction maximum from the edges of the bulk damage region, located 8–10 mm from the end, may favor damage of the surface.

In the process of RE operation, individual damaged regions similar in size to pores accumulate in the bulk. Their quantity grows with time up to several tens per cubic centimeter. Damaged regions shaped as stars grow to several tenths of a millimeter, while the track type may reach tens of centimeters. However, total damaged volume usually does not exceed 1–8% of the element's volume. Exclusion of such a volume from generation does not lead to a noticeable change in the pulse energy or radiation direction. Even elements with numerous damaged regions withstand

hundreds of thousands of pulses. Large damaged areas at the ends and in the bulk can be detrimental, if they overlap a considerable part of the RE cross section. Experimental data on the surface and bulk strength of ruby and sapphire, obtained in the regimen of one-mode generation, are presented in Table 2.15.

Radiation resistance of ruby. Some equilibrium number of CC is observed even in nonirradiated ruby. Radiation resistance of RE is characterized by the change in pulse energy, E_p, and the threshold energy, E_t (Tables 2.16–2.18).

A correlation exists between the generation parameters and the total distortions of the electron paramagnetic resonance spectra (the parameter β in Tables 2.17 and 2.18). The spread in the data presented is related to the impurity content of the RE and other individual peculiarities of the crystals.

Valence transitions of impurity ions lead to changes in laser radiation parameters during the process of irradiation. The quantity of emitting ions diminishes and the processes of energy migration and dissipation change.

The probability of change in the number of dopant electrons during the irradiation process is defined by the ratio of the energy of electron ionization (capture) to the Madelung constant α_M. The state of the ion, I_{Me}^{+n}, is stable if the ionization energy is higher than the absolute magnitude of α_M [96]:

Table 2.15 Surface and bulk radiation resistance of ruby and sapphire

Crystal	Light damage threshold (W/cm²)		t_p (s)
	Surface	Bulk	
Ruby (0.05% of Cr)	10^8–10^9	–	$2 \cdot 10^{-9}$–$2 \cdot 10^{-6}$
	~10^6	–	$5 \cdot 10^{-6}$–$1 \cdot 10^{-4}$
		$(0.6$–$1.0) \cdot 10^{10}$	$(2$–$3) \cdot 10^{-8}$
Sapphire	$(1.0$–$2.0) \cdot 10^{10}$	–	$2 \cdot 10^{-8}$

Table 2.16 Change of characteristics of ruby elements after γ-irradiation

Ruby element	Irradiation conditions	Change of characteristics
0.04–0.05% of Cr^{3+}	$0.8 \cdot 10^3$ rad	$E_p' : E_p = 1.7$
	$1.7 \cdot 10^3$ rad	$E_p' : E_p = 3$
	$1.5 \cdot 10^4$ rad	$E_p' : E_p = 1$
0.04% of Cr^{3+}	$2.7 \cdot 10^4$ rad	
	20 min	$E_p' : E_p = 1.3$
	30 min	$E_p' : E_p = 1.35$, recovery of E_p after 15–20 pulses
0.1% of Cr^{3+}	$1 \cdot 10^6$ rad	$E_p' \geq E_p, E_t' \geq E_t$
		$E_p' : E_p = 0.8{:}1.8 = 0.44$
		$E_t' : E_t = 375{:}145 = 2.6$
0.05% of Cr^{3+}	$1 \cdot 10^7$ rad	Rise of delay time of generation onset from 260 to 427 ms

E_p', E_t' are value after radiation

Table 2.17 Change of characteristics of ruby elements irradiated with fast electrons

Irradiation dose (electrons/cm²)	$E'_t{:}E_t$	$E'_p{:}E_p$	β^a Before irradiation	After irradiation
$7.4 \cdot 10^9$	1.05	1.75	0.47	0.08
$7.4 \cdot 10^{10}$	0.96	3.8	0.16	0.1
$7.4 \cdot 10^{11}$	1.07	0.96	0.7	0.8
10^{14}	0.80–0.75	1.25–1.3	–	–
10^{15}	1.03	1.67	0.26	0.16
10^{15}	1	1	0.1	0.16
10^{15}	0.86	1.35	0.24	0.06
10^{15}	0.87	2.3	0.3	0.02
10^{15}	0.86	1.03	0.12	0.08
10^{15}	0.95	1.14	0.17	0.05

Energy: 10 MeV; flux density: $1.8 \cdot 10^{11}$ electrons/(cm² s)
[a] β is total distortion of EPR spectra

Table 2.18 Change of characteristics of ruby elements irradiated with fast protons (100 MeV)

Irradiation dose (electrons/cm²)	$E'_t : E_t$	$E'_p : E_p$	β Before irradiation	After irradiation
10^{12}	1.65	0.43	0.12	0.4
10^{15}	1.56	0.57	0.2	0.4
10^{15}	1.09	1.2	0.13	0.12
10^{15}	0.78	2.85	0.1	0.07

$$I_{M_e} + n > |\alpha_{\mathrm{M}}| \qquad (2.10)$$

In this formula, distortions of the lattice by the impurity ions are not taken into account. For the cationic site of ideal sapphire, $\alpha_{\mathrm{M}} = -35.2$ eV and the potentials I_{Me} of Al ions have the following values: $I_{Al^+} = 18.83$ eV; $I_{Al^{2+}} = 28.45$ eV; [97] and $I_{Al^{3+}} = 119.98$ eV. The difference $I_{Al^{3+}} - |\alpha_{\mathrm{M}}| = 84.8$ eV indicates high stability of the Al^{3+} state in corundum. For the impurity ions, $I_{Cr^{2+}} = 33.2$; $I_{Cr^{3+}} = 52$; $I_{Fe^{2+}} = 30.6$; $I_{Fe^{3+}} = 57.1$; and $I_{Mn^{2+}} = 34$ eV.

The formation of a charge-deficient or charge-excessive cation in the second coordination sphere does not change the impurity valence. Therefore, the pairs Mn^{2+}–Mn^{4+} are not formed in the ideal lattice of sapphire. The appearance of an electronic state that does not satisfy the relation (II.9) testifies to a considerable content of structural defects stabilizing this state.

Annealing of irradiated RE leads to recombination of radiation defects. Even after short-term light treatment E_p recovers.

The intensity of induced absorption can be reduced by the introduction of vana-dium or titanium. Titanium works as a protector only in crystals annealed in vac-uum or in a reducing medium.

Ti:Al$_2$O$_3$ is one of the best active media for tunable lasers.

Characteristic of *d*-elements is a strong interaction of the unfilled d-shell of the ion with the crystalline field, which results in widening of the absorption bands and in luminescence. Wide luminescence bands are used for tuning laser radiation fre-quency and the spectrum of titanium is one of the widest. Unlike with ruby, the splitting scheme of titanium levels does not contain absorption in the region of pumping and generation.

For Ti:Al$_2$O$_3$-based lasers, efficiencies comparable to or exceeding those of dye lasers in the 0.7- to 0.9-μm range have been achieved. The crystals possess high laser resistance. Breakdown upon irradiation with 0.532-nm wavelength and $t_p = 10$ ns occurs at 4–5 J/cm^{2}energy density. The generation characteristics of Ti:Al$_2$O$_3$ are presented in Table 1.12.

For pumping, the absorption band in the blue-green region of the spectrum cor-responding to the main transition $^2T_{2g} \rightarrow {}^2E_g$ is used. The most intense absorption band is located in the UV region. This region contains the first excited ^{2}S level of free Ti^{3+} ions, which corresponds to the configuration 4S^1 where the absorption is overlapped by the fundamental absorption of the matrix. The transition d → S, resolved with respect to parity and spin, corresponds to charge transfer.

Absorption in the region of generation depends on the content of titanium and reaches 0.15 cm^{-1}, ~10% of the absorption at the main line maximum. Excitation of Ti:Al$_2$O$_3$ in the UV region is accompanied by luminescence, with maxima at 0.25 and 0.315 μm. The crystal has a wide luminescence band in the 0.6- to 1.1-μm region (Fig. 2.82).

In comparison with the absorption spectra, the luminescence spectra show a noticeable distinction between the radiation intensities of different polarizations: the intensity of π-polarization (*E*||*C*) is almost three times higher than with σ-polarization. The luminescence band is asymmetric and has a maximum at 0.79–0.80 μm. The quantum luminescence yield is 0.81–1.0 at 300 K, the lifetime 3.9–2.6 ms.
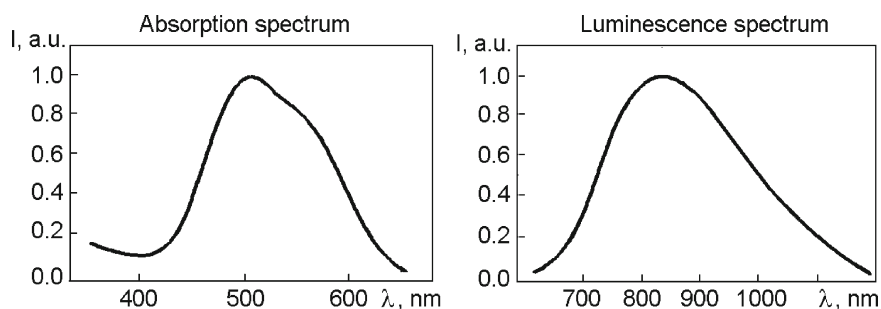
Fig. 2.82 Absorption and luminescence spectra of Ti:Al$_2$O$_3$

Besides the luminescence band in the IR-region, bands that overlap the visible region also are observed. The total luminescence spectrum of Ti:Al$_2$O$_3$ contains an IR-luminescence band of Ti^{3+} with a peak at ~0.78 μm and an additional band in the short-wavelength region with a peak at about 0.42 μm. Upon pumping with high-power radiation of 0.532-μm wavelength, the luminescence lifetime is 4.0 ms for the 0.78-μm band. Its increase is related to luminescence pumping in the blue-green region (~0.42 μm). The lifetime of the short-wavelength band is 7.4 ms, the lifetime of luminescence in the 0.42-μm band is 2.3 ms.

Upon UV pumping two additional luminescence lines are observed: a polarized line with a peak at ~0.425 μm and a π-polarized line with a peak at about 0.575 μm. The lifetime of the latter is 2.1 ms.

The spectral characteristics of both laser media depend on the oxidation–reduction potential of the annealing medium. For high-power (pico- and terawatt) femtosecond Ti:Al$_2$O$_3$-based lasers, acousto-optically programmed filters, pulse compressors, and other means for improvement of the wave front and pulse shape have been elaborated.

2.1.8 Wettability

The effectivity of sapphire use in chemical engineering and in medical implants is defined, among other factors, by the wetting of its surface with liquid substances in contact. The wettability is among the "bioactivity" factors of the implant surface. Depending on the surface destination, both the maximum and minimum wetting may be required. At the same time, there are substantially no literature data on the sapphire wetting. In ref. [98], which deals with the contact wetting angle, the sur-face-free energy of sapphire has been determined to be 52.95 erg/cm^2, but the corresponding crystallographic plane has been identified. In the mineralogical literature, the wettability characteristics of 92–80° are indicated most often; these data are not associated with crystallographic characteristics, too. That is why the angular range is so broad. Sapphire is anisotropic; thus, the surface-free energy values differ considerably for various crystallographic planes [99].

The wettability is characterized quantitatively by the wetting angle Q^0 formed at a solid surface along the phase interface. The value, according to Foxe equation, is related to the material surface energy and depends on the surface-free energy (SFE) values of three phase interfaces being in contact at the wetting line (s–l, s–g, l–g) as follows:

$$\cos Q = (\sigma_{s-g} - \sigma_{s-l}) / \sigma_{l-g}. \tag{2.11}$$

It is the number of free bonds per unit surface area that can be considered to be an approximated measure of that energy.

In real crystals the SFE depends on the number, type, and distribution of structure defects. To unify these parameters, the crystals were grown at the speed of

10 mm/h and annealed in vacuum at 1,950°C. Then 10-mm-thick disks of 18 mm in diameter were cut out of the crystals; the orientation error was less than 1°. The sample surfaces polished to $R_z = 0.05$ μm were wiped with cotton wetted with alcohol and then with water-wetted cloth and dried in air. Measuring rest drop wetting angle Q^0 using optical microscopy, the wetting was studied for pure sapphire at crystallographic planes (0001); {10$\bar{1}$0}; {11$\bar{2}$0}; {10$\bar{1}$2}; and for crystals doped with 0.1% Cr at (0001) plane and with 0.05% Ti at {11$\bar{2}$0}one. The surface was wetted with distilled water, glycerin, and isotonic solution (0.9% NaCl) in air at 25°C. The wetting angle measurement error was 0.5–1.3%.

The wetting angles for the main crystallographic planes of sapphire are within 68 to 85° range both in polar liquid (distilled water) and a nonpolar one (glycerin) (Figs. 2.83 and 2.84). The nonpolar glycerin wets the surfaces of all samples studied better
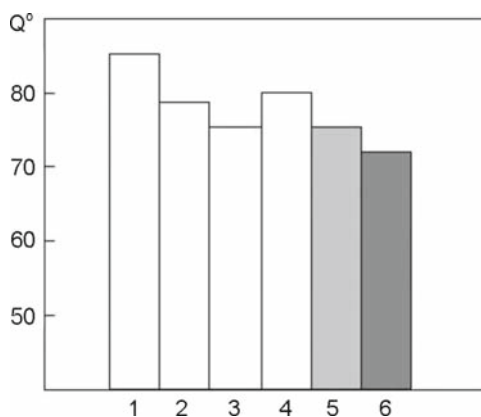
Fig. 2.83 Wetting angle of sapphire planes with water: (*1*) (0001), (*2*) {10$\bar{1}$0}, (*3*) {11$\bar{2}$0}, (*4*) {10$\bar{1}$2}, (*5*) {11$\bar{2}$0}(0.05 Ti), (*6*) (0001) (0.1 Cr)
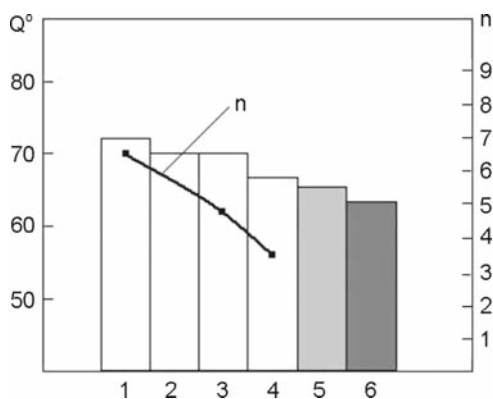
Fig. 2.84 Wetting angle of sapphire planes with glycerin: (*1*) (0001), (*2*) {10$\bar{1}$0}, (*3*) {11$\bar{2}$0}, (*4*) {10$\bar{1}$2}, (*5*) {11$\bar{2}$0}(0.05 Ti), (*6*) (0001) (0.1 Cr)

than water. The crystallographic orientation and dopants more weakly affect the Q^0 value, although the general variation character remains unchanged. The crystal doping is a factor of importance enhancing the wettability. Doping with Cr ($C = 0.1\%$) causes $Q^0_{(0001)}$ decrease by 12° and 8° for water and glycerin, respectively. The same effect is revealed at Ti doping ($C \sim 0.05\%$), the $Q^0_{(11\bar{2}0)}$ decrease amounting 3°. In isotonic NaCl solution ($C = 0.9\%$), the crystal composition and crystallographic parameters are observed to influence the wettability, too, but the variation trend does not correlate with the data on other liquids in all the cases. This can be explained by differences in effects of the solution ionic components (Na^+ and Cl^-) on the physicochemical sorption processes at the planes studied. The values of surface energy for the sapphire crystallographic planes estimated from the wetting angles are in correlation with the results of wear resistance tests carried out before. The maximum wear rate with free abrasives is seen to correspond to minimum Q^0 values (maximum energy) in water for $\{10\bar{1}0\}$ and $\{11\bar{2}0\}$ (see Fig. 2.83). This demonstrates that water is involved actively in the wearing process as a surface-active substrate. The maximum biological inertness of a sample corresponds to minimum surface energy and respectively to the maximum possible wetting angle. These data are in correlation also with corrosion resistance of various crystallographic planes of sapphire [100].

The physicochemical processes in the treatment area in the presence of water can be described briefly as follows. At the crystal–liquid interface, considerable adhesion forces occur between the liquid boundary layer molecules and the crystal surface. These forces hinder the sliding at the interface. The wetting phenomenon is explained usually by such an interaction of force fields. The surfaces in friction are separated as a rule by a thin lubricant layer that is connected so strongly that their direct contact is excluded, and the relative displacement occurs along the intermediate liquid layer. The surface activity of a liquid depends on its molecular structure, the activity being the stronger the higher the molecular polarity. As the liquid molecules adsorbed at the crystal surface are mobile, the molecular interaction is propagated into the crystal near-surface layer along the microcracks. The wedging effect of the liquid molecules (the Rebinder effect) develops the microcracks toward macrocracks, and thus causes the shearing of particles from the crystal surface, so the dispersion process is facilitated. Since water wets the $\{10\bar{1}0\}$ and $\{11\bar{2}0\}$ planes better during the grinding, it is just these planes where the maximum wear rate is observed.

Thus, the dependence of sapphire wetting with water and glycerin on the crystallographic orientation has been studied. The wetting angle for both liquids is maximum at the (0001) plane. The minimum wetting angle values are observed at $\{10\bar{1}0\}$ and $\{11\bar{2}0\}$ for water and at $\{10\bar{1}2\}$ for glycerin. A correlation has been found between the water wettability of the main crystallographic planes of sapphire and the wear rate of those planes under grinding with free abrasive using water as the suspension medium.

2.2   Chemical Properties

Molecular mass	101.9612
Electronegativeness	2.58
Dissociation energy of molecule, $D_{Al_2O_3}$	740 kcal/mol
Formation heat for Al_2O_3 molecule	377 kcal

2.2.1   Dissolution

Dissolution of crystals is studied to determine the symmetry, facets of equilibrium form, traces of radioactive decay (tracks of decay), dislocation structure, as well as to increase the strength by removing the defective surface-adjacent layer formed at mechanical treatment. The rate of dissolution V_s is a function of the surface energy and the bond strength and to a certain extent depends on the defectiveness of the surface-adjacent layer. The process of dissolution (etching) of crystals usually begins at the most active points, such as the places where dislocations reach the surface. The shape of etch pits (Fig. 2.85) depends on the location of the chains of the strongest bonds [101] which also define the appearance of crystals.

The dependence of the rate of dissolution on the orientation of crystals was revealed as far back as the nineteenth century [102]. The rate grows as the density of ions on the facet increases and the energy of bonds between the ions diminishes.
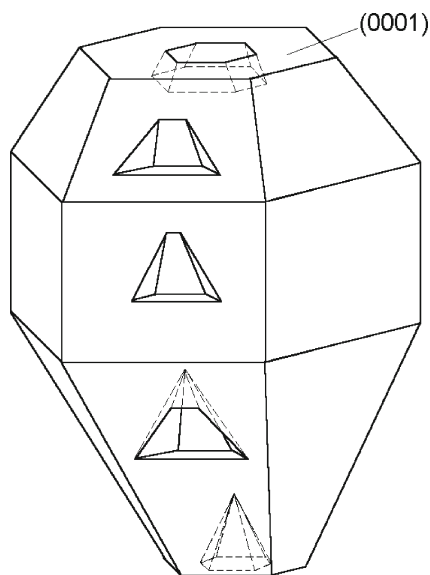
Fig. 2.85 Etch pits shown as an intersection of the figures of the growth form with fictitious (negative) etching polyhedrons

The bond type also matters. With other conditions being equal, the activation energy of covalently bonded ions is higher due to the fact that at oscillation shifts higher energy is required to overcome the bonding force.

Crystal facets, edges, and vertices dissolve at different rates. In the process of dissolution, slopes of the surfaces of the corresponding orientations move along the isoclines in the direction of trajectory of the peak of the dissolution body (Fig. 2.86) [103].

The isoclines are contiguous to the normals to the facets and coincide with them at least at one point, e.g., in the directions $[1\bar{1}2]$ and $[1\bar{2}1]$. In the zones where the vertices and the edges are located, V_s has the maximum value. The vertex motion rate is defined by the relation

$$V_{[0\bar{1}1]} = \frac{V_{[\bar{1}\bar{1}2]}\sqrt{3}}{2} = \frac{V_{[1\bar{2}1]}\sqrt{3}}{2} \tag{2.12}$$

At dissolution of sapphire in H_3PO_4 at 573 K the dominating final equilibrium form (*L*-form) is the rhombohedron $[10\bar{1}2]$; dissolution of other planes obviously suppressed by adsorption. The dissolution stages of sapphire ball (the view along $[20\bar{2}1]$) are shown in Fig. 2.87.

The facet $(10\bar{1}2)$ moves at the constant movement d_r. The final form of dissolution of a spherical sample consists of the facets of equilibrium form.

The equilibrium form of Al_2O_3 crystals was theoretically determined by Heimann [104] using the PBC method. The facets $\{10\bar{1}2\}$, $\{11\bar{2}0\}$, $\{10\bar{1}4\}$, $\{0001\}$ belong to the dissolution form of concave hemisphere (*G*-form). As in the case of *L*-form, the rhombohedron $\{10\bar{1}2\}$ is a significant facet of *G*-form. The $\{11\bar{2}0\}$,
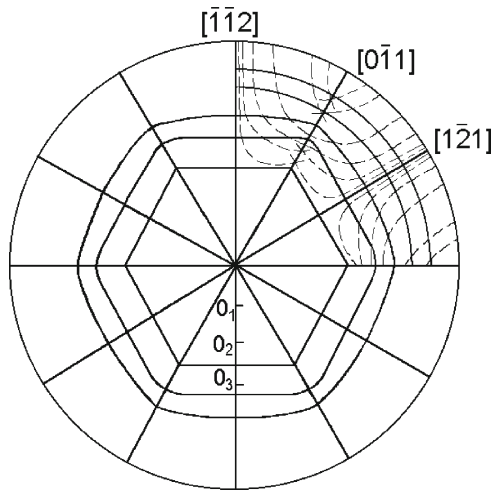
Fig. 2.86 Isoclines at dissolution of a hexagonal crystal
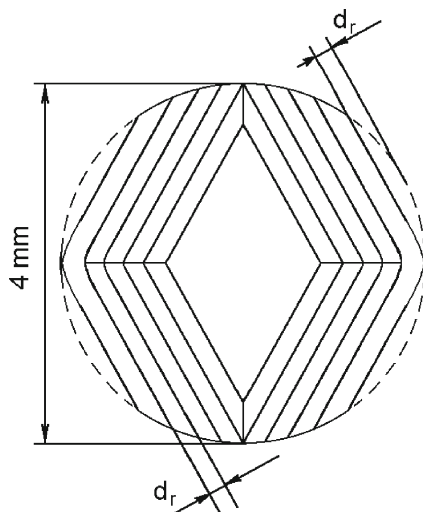
Fig. 2.87 Stages of dissolution of sapphire ball in H_3PO_4 at 573 K
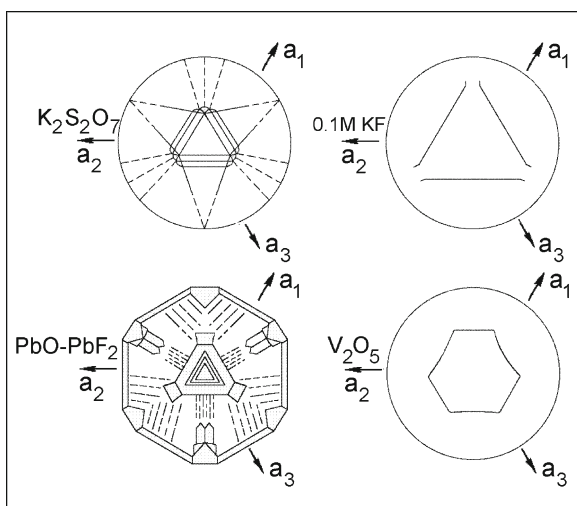
Fig. 2.88 Idealized view of etched hollow hemispheres with a diameter of 4 mm on (0001) facet of sapphire

{0001}, and the rhombohedron {10$\bar{1}$4} follow. As follows from Fig. 2.88, Table 2.19 and the forms of dissolution of sapphire in solvents (Figs. 2.89–2.94), all the observed *L*-forms can be explained by the participation of the facets {11$\bar{2}$0}, {10$\bar{1}$4}, {0001} on *G*-form polyhedron [105–107].

By cutting off the vertices of this polyhedron the *L*-form is obtained. It consists of two rhombohedrons shifted by 60° and of two scalenohedrons (Fig. 2.93).

Table 2.19 G and L forms of sapphire

Solvent	Theoretical L form	Experimental L form	Type (Fig. 2.93)	Theoretical G-form (Fig. 2.89)	Experimental[a] G form (Fig. 2.88)
$K_2S_2O_7$ <800°C >800°C	$[\bar{0}hh1], [\bar{h}0h1],$ $2[hkil]$	$[10\underline{1}\underline{3}]>[14.\bar{5}.9.\underline{18}]$ $[14.\bar{5}.9.\underline{18}]> [1013]$	I	$\{0001\}+ \{11\bar{2}0\} + \{10\bar{1}2\} + \{\bar{1}014\}$	$(0001), 3(\bar{h}0hl), (\bar{h}0hl), (hkil)$
$PbO–PbF_2$ (1:1), 950°C	$[\bar{0}hh1], [\bar{h}0h1],$ $2[hkil]$	$[123]>[\underline{3}0\bar{3}5] [\bar{5}054]>$ $[4.\bar{1}8.14.15]$	I	$\{0001\} + \{11\bar{2}0\} + \{10\bar{1}2\} + \{\bar{1}014\}$	$(0001), 3(\bar{h}0hl), (\bar{h}0hl), 2 (hkil), (hh\bar{2}hl)$
0.1 M KF, 600°C, 3 kbar	$[\bar{h}0h1], [2[\bar{h}0h1]$	$[\bar{5}054]>[10\bar{1}5]>[10\bar{1}3],$ $[60\bar{6}1]$	II	$\{0001\} + \{11\bar{2}0\} + \{10\bar{1}2\}$	$(0001), (\bar{h}0hl), (\bar{h}0hl)$
V_2O_5, 950°C	$[\bar{h}0h1]$	$[\bar{5}054]$	III	$\{0001\} + \{10\bar{1}2\}$	$(0001), (\bar{h}0hl), (\bar{h}0hl)$

[a]Due to unsatisfactory geometry of hollow hemisphere the prism facets ($\underline{hh}\underline{\bar{2}h}0$) can be observed only in exceptional cases ($PbO–PbF_2$)
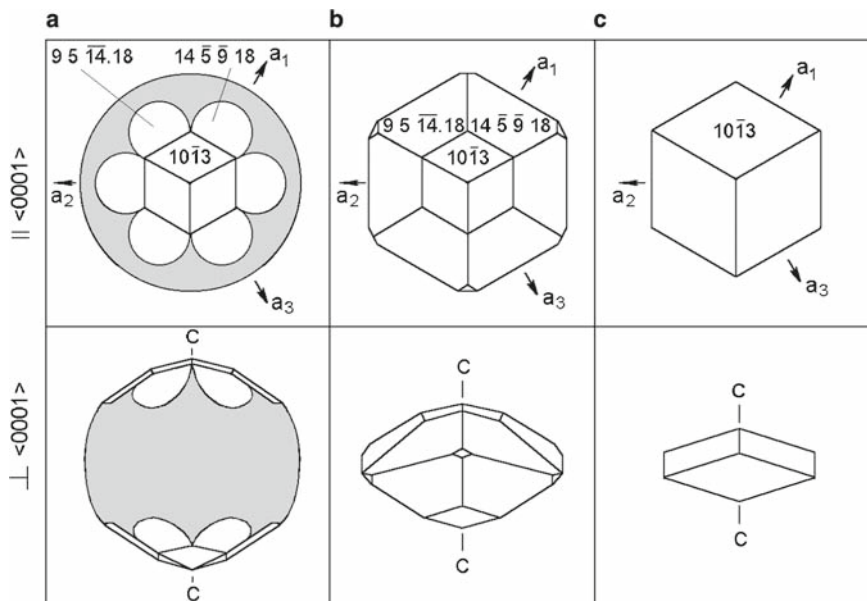
Fig. 2.89 Forms of dissolution of sapphire (*L* forms) in K$_2$S$_2$O$_7$ melt at *T* < 1,073 K. Shaded regions show primary sphere surfaces
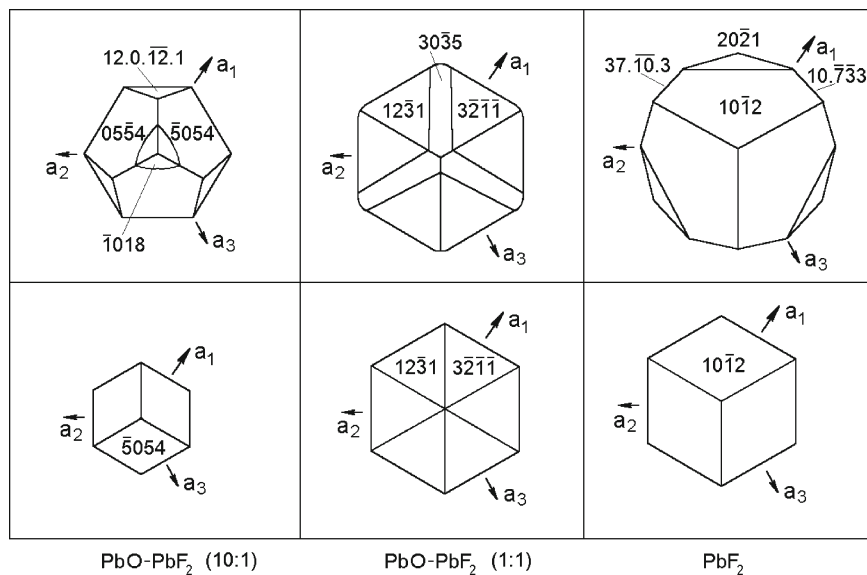
Fig. 2.90 Forms of dissolution of sapphire in pure PbF$_2$ melt and in PbO–PbF$_2$ (with 1:1 and 10:1 molar ratios) at 1,223 K
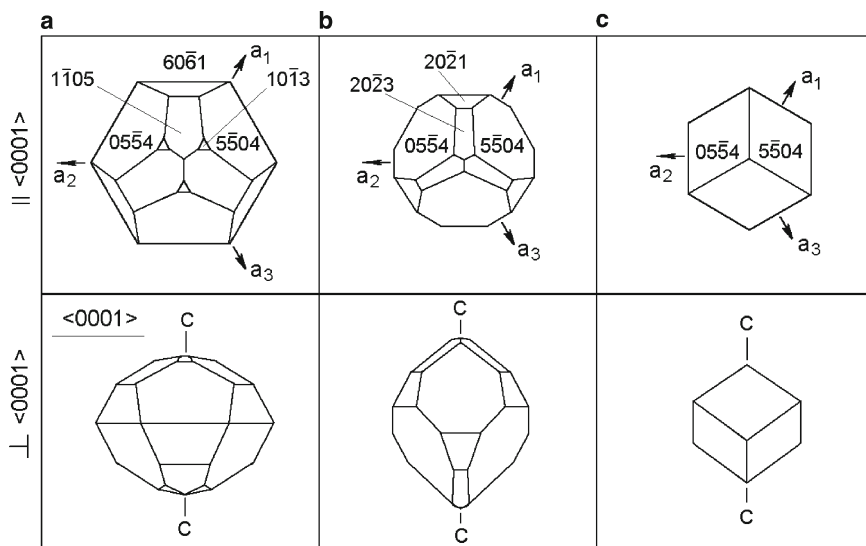
Fig. 2.91 Forms of dissolution of sapphire in 0.1 M KF and K₂CO₃ at 873 K and 3 kbar
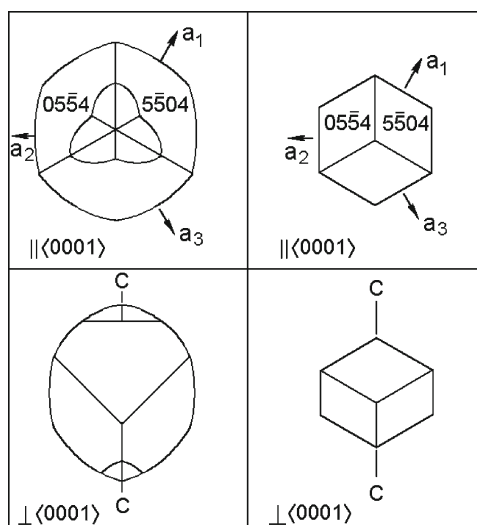
Fig. 2.92 Forms of dissolution of sapphire in V₂O₃ melt at 1,223 K

Experimentally these facets were found at dissolution of sapphire in $K_2S_2O_7$ melt. The cut of the final form is temperature-dependent (see Table 2.19).

The polar diagram V_s (Fig. 2.94) obtained at dissolution of sapphire spheres at their interaction with carbon in a gaseous medium vividly shows the presence of dissolution anisotropy [108]. To build this diagram, the segments proportional to V_s
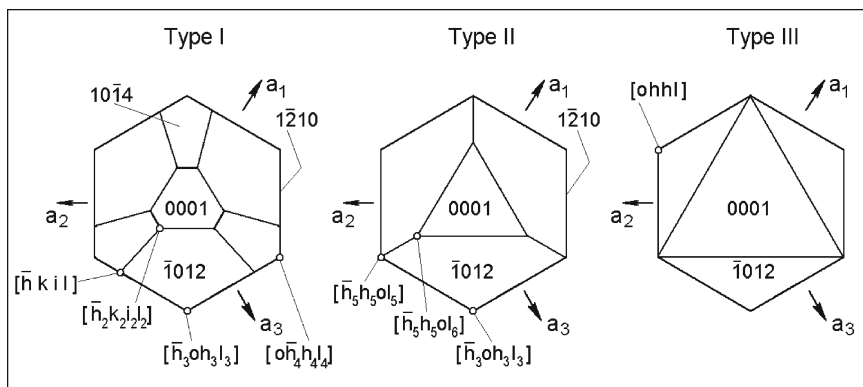
Fig. 2.93   *G*-polyhedron form of sapphire (in [0001] direction) with *L* facets formed at cutting off the vertices
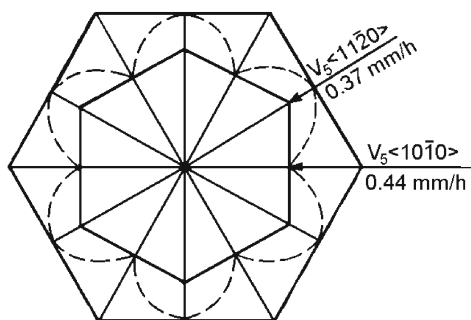
Fig. 2.94   Polar diagram of the rate of dissolution

in $\langle 11\bar{2}0 \rangle$ and $\langle 10\bar{1}0 \rangle$ directions were laid off along radius vectors. The internal envelope of the diagram presents the form of dissolution and the external one shows the stationary growth form for the basal plane.

The ideal dissolution form of sapphire that depends on the lattice parameters and is independent of the conditions of dissolution is a parallelogram dodecahedron with rhombohedral symmetry group. The real form depends on the impurities, nature of the solvent, and the conditions of dissolution (Fig. 2.95, Table 2.20) [110].

On all types of facets and at all the temperatures the dissolution rate of ruby is higher. On the surface of ruby spheres a rougher layer is formed.

The role of water in the processes of hydrothermal dissolution of sapphire is investigated in connection with crystallization under hydrothermal conditions. Solubility of sapphire in pure water is very low even at thermobaric parameters.[3]

---

[3]Solubility of 8 mg of sapphire in 100 ml of water at 1,070 K and a pressure of 6 kbar is 0.0035%.
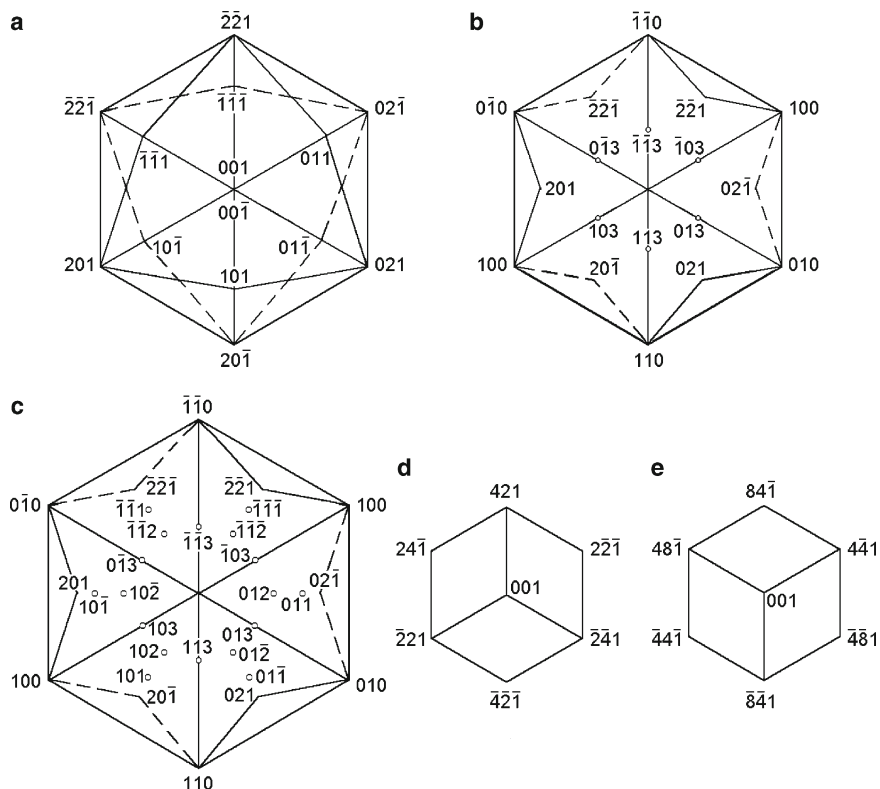
Fig. 2.95 Stereographic projections of dissolution forms of sapphire and ruby: (**a**) ideal dissolution form. (**b–e**) Real dissolution forms obtained under the conditions: (**b**) thermochemical etching of sapphire and ruby spheres; (**c**) dissolution of ruby in carbon oxide; (**d**) dissolution of sapphire spheres in the melts of PbO–PbF$_2$ (1:1); PbO–PbF$_2$ (10:1), 273 K; 0.1 M KF or 0.1 M K$_2$CO$_3$, 873 K, 3 kbar; Y$_2$O$_3$, 1,223 K [109]; (**e**) dissolution of sapphire spheres in pure PbF$_2$, 1,223 K

However, in the presence of mineralizers, in particular, alkalis, the solubility sharply increases. The results of experimental investigations of dissolution kinetics of quartz and sapphire in water solutions in autoclaves at 373–723 K are presented in Fig. 2.96 [111]. The numeric results are given in Table 2.21.

The data contained in the table data make it possible to calculate the dissolution rate constant according to the formula:

$$dC / dt = kS(C_k - C_\tau),$$

(2.13)

where C_k is the content of Al$_2$O$_3$ in saturated solution, C_τ is the concentration of the dissolving substance at the moment of time τ, and S is the surface of the dissolving material.

Table 2.20 Anisotropy of dissolution rates of sapphire and ruby spheres and polar diagrams V_s in basal plane

T (K)	hkl	V_s (mm/h)		Polar diagrams	
		Sapphire	Ruby	Sapphire	Ruby
1,773	001	0.033	0.396		
	110	0061	0.445		
	021	0.085	0.530		
	113	0.100	0.538		
1,873	001	0.085	0.475		
	110	0.095	0.535		
	021	0.110	0.685		
	113	0.210	0.695		
1,973	001	0.330	0.860		
	110	0.370	0.870		
	021	0.380	0.900		
	113	0.400	0.960		
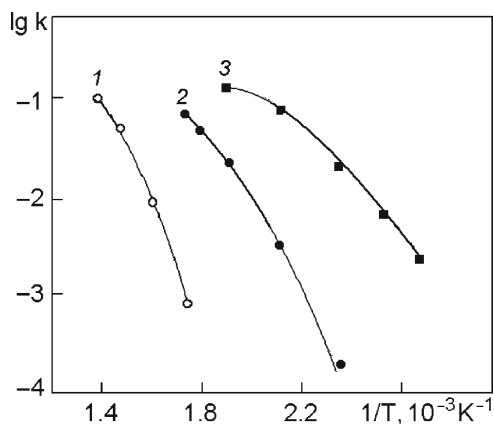
Fig. 2.96 Logarithm of the constants of quartz and corundum dissolution rates in NaOH and NH$_4$F water solutions as a function of reciprocal temperature (500 atm. pressure): (*1*) corundum, 0.5 M NaOH, (*2*) quartz, 1 M NaOH solution, (*3*) quartz, 1 M NH$_4$F solution

The lower temperature boundary is limited by 573 K, as at temperatures below the said magnitude it requires too long a time to reach equilibrium: 150 days at 523 K, 838 years at 423 K, 175,000 years at 373 K. Continuous decrease of the value of apparent activation energy – 33.5, 31.2, and 15.4 kcal/mol – with the growth of temperature in 573–623, 623–673, and 673–723 K intervals is explained by the fact that in the process of dissolution the resistance of the surface-adjacent layer to

Table 2.21 Dissolution of sapphire in 0.5 M NaOH water solution at different temperatures and a pressure of 500 atm

τ (h)	V_s (g/l)	τ (h)	V_s (g/l)	τ (h)	V_s (g/l)	τ (h)	V_s (g/l)
	573 K		623 K		673 K		723 K
14	1.3	5	6.2	0.5	5.0	0.167	4
39	3.5	10	7.7	1	7.9	0.5	8.6
70	5.1	15	12.1	1.5	11.0	1	12.4
108	8.7	17.5	14.2	2	12.2	3	20.2
144	11.1	20	13.2	3	14.9	5	20.1
180	14.3	25	15.9	4	16.7	7.5	20.9
234	16.5	30	17.6	5	18.6	10	20.6
360	16.5	36	18.7	7	21.1	15	20.6
		48	17.7	9	20.0		
		60	17.8	12	20.1		
				18	19.6		
				36	20.7		
				48	20.2		

The experiments in which equilibrium takes place are separated by bold line. The average values for calculating the dissolution rate constants are the following: 573 K – 16.5; 623 K – 17.9; 673 K – 20.1; 723 K – 20.5 g/l.

Table 2.22 Contamination of acid solutions by aluminum after treatment of sapphire by boiling acid solutions, (mk g)/mol

		Time of boiling (h)				Time of boiling (h)	
Acid solution		3	6	Acid solution		3	6
HCl	5 mol	0.04	–	HNO_3	5 mol	1.5	–
HCl	12 mol	0.2	2.6	HNO_3	14 mol	14	35
H_3PO_4	5 mol	6.5	–	H_2SO_4	5 mol	1.8	–
H_3PO_4	12 mol	11	11	H_2SO_4	18 mol	90	150

diffusion through it diminishes. In ref. [111] such an effect is attributed to the decreasing thickness of the layer of adsorbed water molecules. The components dissolved in aqueous medium have a destructive influence on the surface-adjacent layer of water, the intensity of which depends on hydration properties of the ions.

Due to low solubility of sapphire in acids, one can estimate their interaction from the contamination of acids by aluminum (Table 2.22) [112].

In a number of analytical methods for controlling stoichiometry of crystals and the distribution of impurities in them (atomic-emission and atomicsorption spectrometry with flame atomization of substances), the analyzed material is introduced into a flame atomizer in the form of solution. The most suitable solvent for the analysis of sapphire is concentrated orthophosphoric acid.

Orthophosphoric acid is one of a few low-temperature solvents used for corundum crystals. It has the form of reaction mixture containing $H_4PO_4^+$ cations and

$H_3P_2O_7^-$, and $H_4P_3O_{10}^-$ anions formed as a result of H_3PO_4 condensation, and a change of its acid–base function. The dissolving action of condensed phosphoric acids at increased elevated temperatures is caused by loosening of the anionic part of corundum lattice and by passing of cations into solution due to the complexation with $H_3P_2O_7^-$ and $H_4P_3O_{10}^-$.

A noticeable dissolution of sapphire in concentrated orthophosphoric acid starts at 483 K, the optimum temperature being 543–573 K. The conditions of dissolution are shown in Table 2.23 and in Fig. 2.97.

Further growth of temperature is unreasonable, as it leads to condensation of phosphoric acids, and as a consequence to the formation of low-soluble glasslike products. (This phenomenon gave rise to the error of some investigators who reported the polishing action of H_3PO_4 at $T > 673$ K. In fact, it was the effect of pseudopolishing caused by the formation of a glasslike aluminum phosphate film on the crystal surface.)

The mixture of H_3PO_4 with H_2SO_4 possesses more stable properties. The ratio of H_2SO_4 to H_3PO_4 ranges from 1:1 to 1:3 (Table 2.24).

Impurities and dispersivity of samples increase their solubility (Fig. 2.98). The action of stronger solvents (Figs. 2.99 and 2.100) was studied. The dissolution heat of Al_2O_3 in lead fluoride is 9.8 kcal/mol [114].

Table 2.23 Conditions of dissolution of aluminum oxide in condensed phosphoric acid [113] (the volume of initial 70% orthophosphoric acid was 10 ml)

Substance	Weight (g)	T (K)	Dissolution time (min)	Conventional solubility (g/ml)[a]
α-Al_2O_3 powder	0.3...0.4	540	16	0.050
α-Al_2O_3 crystal	0.15	560...570	30	0.16
α-Al_2O_3:Ti powder	0.3	540	13	0.090
α-Al_2O_3:Ti crystal	0.2	570	25	0.020

[a] Mass of the substance (g) passing into solution at 540 K, in reference to 1 ml of initial 70% phosphoric acid
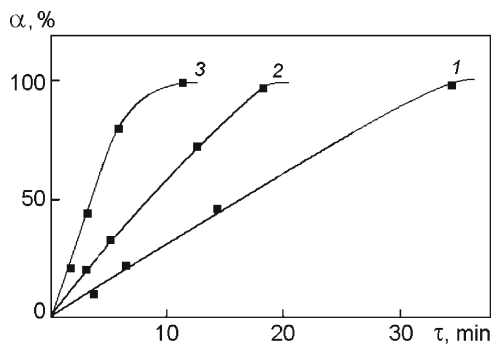
Fig. 2.97 Time dependence of the share of dissolved Al_2O_3. A weight of 0.3 g. (*1*) 215°C; (*2*) 270°C; (*3*) 330°C

Table 2.24 Temperature dependence of dissolution rate for (0001) plane (μm/h)

T (K)	H$_2$SO$_4$: H$_3$PO$_4$		
	3:1	2:1	1:1
523–568	20		
578–583	60	40	25
583–588	65		
618–628	120		
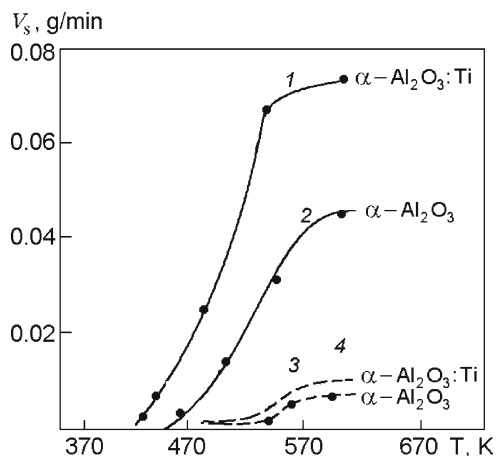
Fig. 2.98 Temperature dependence of sapphire dissolution rate V_s (*1*) Ti:Al$_2$O$_3$ with a dispersity up to 40 μm (raw material); (*2*) Al$_2$O$_3$ with a dispersity up to 40 μm (raw material); (*3*) Ti:Al$_2$O$_3$ crystal; (*4*) Al$_2$O$_3$ crystal

The dissolution rate of sapphire also grows after irradiation. As a rule, it is connected with surface damage or with the absorption of bombarding particles, such as krypton, by the surface-adjacent layer.

2.2.2 Thermochemical Polishing

In some cases it is necessary to remove the damaged layer that arises on the surface of polished crystals without significant worsening of the polishing quality. This can be realized by thermal treatment of sapphire in vacuum or in gaseous media. However, to obtain the desired effect, high temperatures (over 1,973 K) are required.

a Al$_2$O$_3$ wt. %

b V_s, wt. %
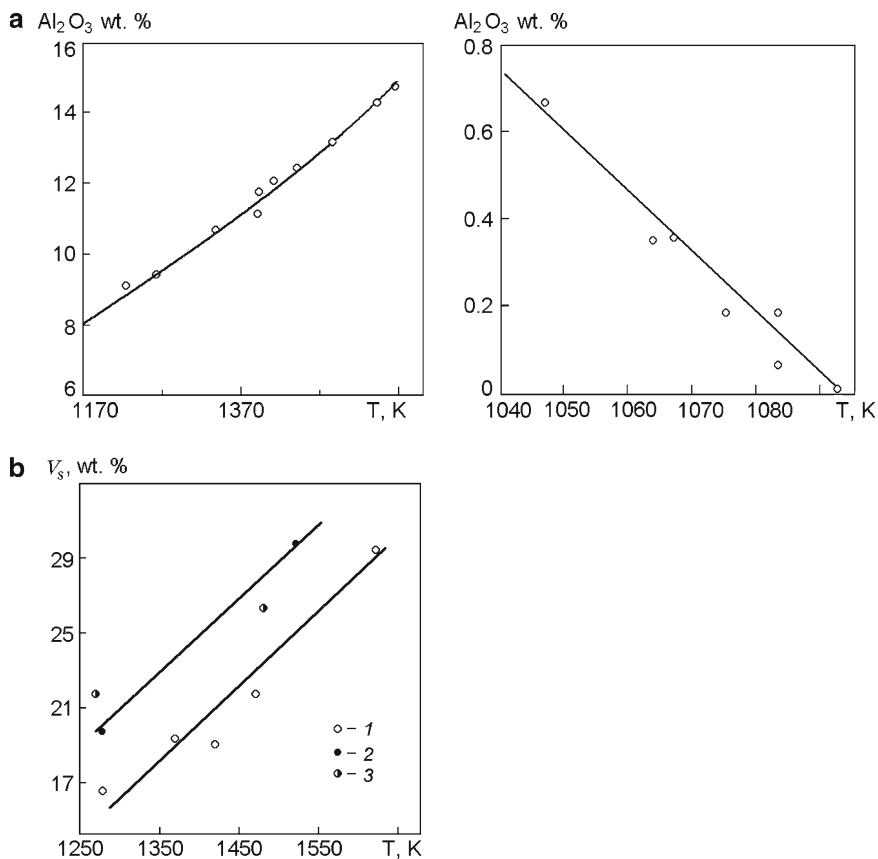
Fig. 2.99   Solubility in PbF$_2$ melt for (**a**) sapphire and Al$_2$O$_3$:Ga, Cr, (*1*, **b**); Al$_2$O$_3$: 46% Ga (*2*, **b**); Al$_2$O$_3$: 1.32% Ga (*3*, **b**) [114]
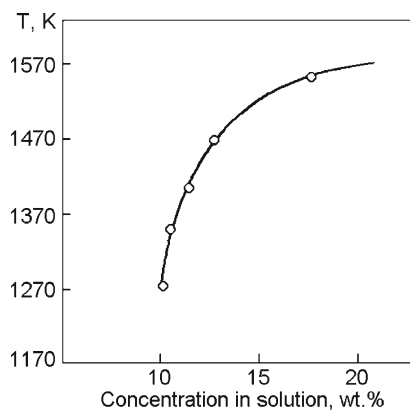
Fig. 2.100   Solubility of sapphire in PbO–0.35 Ba$_2$O$_3$–1.2 PbF$_2$ melt [114]

Thermochemical polishing proceeds at lower temperatures. For instance, in potassium bisulfate melt a noticeable dissolution starts at 723 K. When heated up to temperatures higher than the melting point (419 K), potassium bisulfate transforms into pyrosulfate and then at $T > 673$ K it becomes the normal sulfate:

$$2KHSO_4 = K_2S_2O_7 + H_2O \qquad (2.14)$$

Dissolution of aluminum oxide in potassium bisulfate melt proceeds according to the scheme:

$$Al_2O_3 + 3K_2S_2O_7 = Al_2(SO_4)_3 + 3K_2SO_4 \qquad (2.15)$$
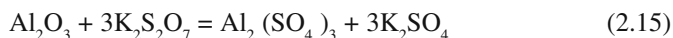
Stirring increases the dissolution rate. The dissolution rate in $K_2S_2O_7$ is described by the equations [115]:

$$lgV_s = 4.84 - 4310/T \text{ (at stirring)} \qquad (2.16)$$

$$lgV_s = 5.63 - 5350/T \text{ (without stirring)} \qquad (2.17)$$

The activation energies are 23.5 ± 1 and 20.0 ± 0.5 kcal/mol, respectively.

Widespread solvents do not always provide a polishing effect (Table 2.25). As follows from the table, solvents can both polish and etch the surface.

Table 2.25 Dependence of the state of sapphire surface on the type of solvent and regimen

Solvent	T (K)	V_s (μm/min)	Action on surface	Reference
H_3PO_4	570	50	Selective etching	[116]
	690		Polishing	
KOH, concentrated	620		Selective etching	[116]
$Na_2B_4O_7 \cdot 10H_2O$	1,170	1	Weak polishing	
	1,220	2.6	Weak polishing	
	1,270	3	High-quality polishing	
	1,320	4	Breaking of corners/edges	
	1,370	5	Etching	
	1,320	12	Strong etching	
$Na_2B_4O_7 \cdot 10H_2O$ + LiF	1,070	2	Weak polishing	
2% LiF	1,120	3	High-quality polishing	
7% LiF	1,170	5	High-quality polishing	
10% LiF	1,120	5–6	Strong etching	
$Na_3AlF_6/Na_2B_4O_7 \cdot 10H_2O$ (2:1)	1,270	–	Polishing effect	[117]
$KHSO_4/Na_3AlF_6$ (3.5:1)	1,120	–	Polishing effect	[117]
PbF_2/PbO	820–920	–	Polishing effect	
V_2O_3	1,070	1.5	Weak polishing	
	1,170	2	Polishing effect	
	1,270	2.3–2.5	High-quality polishing	
	1,320	3–4	Etching	

In ref. [115] chemical polishing was realized by means of $Na_2B_4O_7$ vapor. The crystal was heated up to 1,273–1,473 K. In ref. [118] the crystal that was heated up to 1,273 K was polished by colloid silicon dioxide under pressure.

The purpose of thermochemical polishing is to remove the surface-adjacent layer at minimal worsening of the quality of polishing. This can be achieved by providing thermodynamic equilibrium of dissolution process, when the rate of crystal dissolution is proportional to the difference between the saturation concentration and the concentration of the dissolved sapphire. The said problem is solved by using V_2O_3-based polishing solvents.

Metavanadates of alkali metals [119, 120] are grown by melting V_2O_3 and, e.g., LiOH. The temperature dependence of the saturation concentration of C_s is described by the relation

$$\lg C_s = A - B/T, \qquad (2.18)$$

where A, B are constants (Table 2.26). Anhydrous powder of alkali metal metavanadate powder and a calculated amount of aluminum oxide powder are placed into platinum crucible, where this mixture is heated up to 1,123–1,148 K and kept during 2 h. Then the sample is dipped into the crucible. After the treatment the crystal is washed in alkali metal chloride melt.

Colloidal SiO₂ solution is one of the best reagents for chemical surface polishing and the medium into which the products of the low-temperature reaction

$$xAl_2O_3 + ySiO_2 + H_2O \rightarrow Al_{2x}Si_yO_{3x+2y}H_2O \qquad (2.19)$$

are removed. Gaseous medium also is effective enough for thermochemical polishing (etching, evaporation). For such purposes hydrogen, fluoride (SF_4, $CCIF_4$, CHF_3), and carbon media are used.

CClF₃ is used as a polishing etchant for the planes $(10\bar{1}2)$, $(11\bar{2}0)$, (0001), and $(10\bar{1}4)$.

The etching temperature is 1,670–1,500 K. The maximum etching rate makes 0.6 μm/min at 1,770 K. The treatment in hydrogen flow is most often used.

Hydrogen medium at 1,173–1,973 K activates the processes of healing of surface defects at the expense of the reduction and evaporation of aluminum oxide. Changes in sapphire morphology are observed at temperatures starting from 1,573–1,623 K (Fig. 2.101).

The character of the opening up surface points to the fact that the material is removed layer by layer, parallel to the basal plane. At $T > 1,923$ K, the effect of

Table 2.26 Values of constants for sapphire dissolved in metavandates of alkali metals

Solvent	A	B
$LiVO_3$	2.93	3,020
$NaVO_3$	2.64	2,680
KVO_3	2.12	1,940
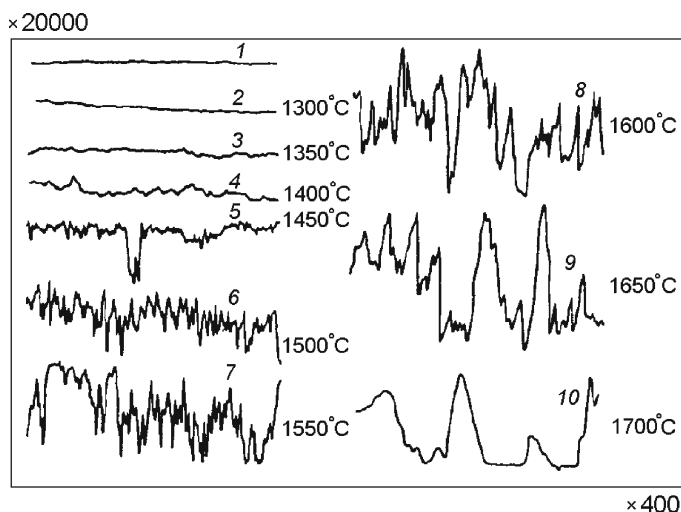
Fig. 2.101 Changes in sapphire surface microrelief at successive thermal treatment in dry hydrogen. The time of holding the sample at each temperature is 3 h. The plane (0001). (*1*) Initial sample; (*2–10*) samples treated at different temperatures; ordinate axis – vertical increase; abscissa axis – horizontal increase

such a selective removal of material vanishes and the process acquires polishing character.

A noticeable loss of the weight of the samples is observed starting from 1,623 K. The evaporation rate is $0.37 \cdot 10^{-2}$ mg/cm^2 h. In dry hydrogen medium at 1,623–1,673 K complete transformation of the damaged surface-adjacent layer without noticeable changes in the surface quality and in the dimensions of the product takes place. The rise of the temperature to 1,973 K leads to a sharp increase in the evaporation rate to 1.8 mg/cm^2 h. As the rate of sapphire evaporation in vacuum is insignificant (at 1,973 K it makes ~0.05–0.1 mg/cm^2 h) and has a dissociative character, the rise of evaporation can be explained by chemical interaction of sapphire with hydrogen and by carryover of the products of the reaction

$$Al_2 O_3 + 2H_2 \rightarrow Al_2 O + 2H_2 O \qquad (2.20)$$
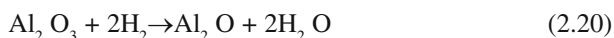
The observed transport of aluminum oxide obviously is connected with Al_2O decomposition and the formation of Al_2O_3 and Al:

$$3Al_2O \rightarrow Al_2O_3 + 4Al \qquad (2.21)$$

The rate of sapphire etching in hydrogen is the logarithmic function of the temperature (Fig. 2.102) [121].

At deposition of silicon on sapphire substrate the latter is annealed in hydrogen in the same reactor where silicon layers are grown. Under the conditions when the rate of hydrogen flow is 1–5 l/min, the annealing time is 15–180 min and removal of material at 1,473–1,932 K is accompanied with polishing. Although the polishing
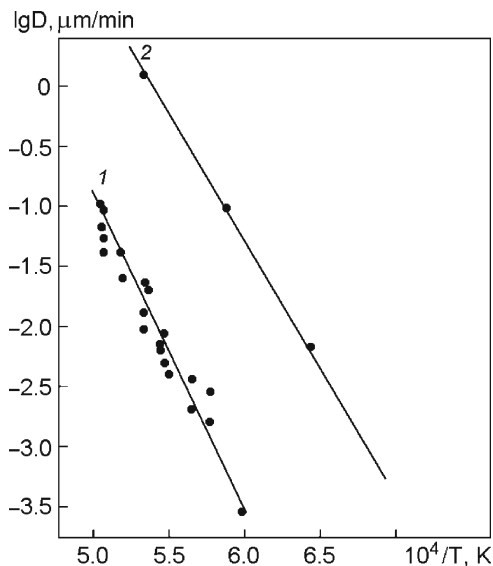
Fig. 2.102 Temperature dependence of the rate of sapphire evaporation in hydrogen; (0001) plane. (*1*) Successive treatment with holding during 3 h at each temperature; (*2*) treatment in the presence of graphite

rate (from 0.003 μm/min at 1,473 K to 0.3 μm/min at 1,923 K) is lower than the rate of polishing in melts, the quality of polishing is higher. As a rule, the silicon films grown on substrates thermochemically polished in $Na_2B_4O_7 \cdot 10H_2O$ and H_3PO_4 melts have polycrystalline structure. Besides the Kekuchi lines, the electron diffraction patterns of the surfaces of these substrates contain diffusion rings. After removal of a 3-μm-thick sapphire layer by etching in hydrogen at 1,773–1,923 K, the electron diffraction patterns clearly show the presence of Kekuchi picture.

Carbon-containing media, for example, CO and CO_2, to a larger extent favor evaporation of the surface-adjacent layer. Therefrom, the processes of recrystallization of the defective layer starting from 1,173 K and reduction of aluminum oxide with its subsequent evaporation starting from 1,623 K at of 10^{-2}–10^2 Pa pressure take place [116, 117, 121].

Aluminum oxide reduction by carbon oxide in vacuum proceeds according to the scheme:

$$Al_2O_3 + CO = Al_2O_2 + CO_2 \tag{2.22}$$

$$Al_2O_3 + CO = 2AlO + CO_2 \tag{2.23}$$

$$Al_2O_3 + 2CO = Al_2O + 2CO_2 \tag{2.24}$$

$$Al_2O_3 + 3CO = 2Al + 3CO_2 \tag{2.25}$$
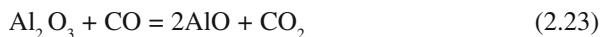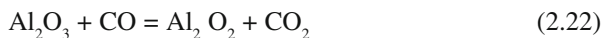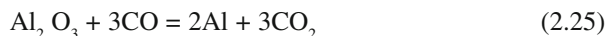
The quality of the etched surface depends on the temperature, gas pressure, and crystallographic orientation (Fig. 2.103).

The observed difference between the etching rates of the basal and prism planes is explained by different densities of oxygen atoms in these planes. For nonselective etching (polishing) it is necessary to etch off $\sim 10^{-8}$–10^{-7} g/(cm^2 s) layer, depending on the temperature and the crystallographic orientation.

Etching with the help of carbon-containing medium also is used for obtaining figure holes in sapphire. For this purpose special graphite shapers are applied; carbon-containing medium is formed between the shapers and sapphire at sufficiently high temperatures [123].

Ionic plasma etching reduces the temperature of the process to 470–770 K. As etching gases, argon, CF_3, CF_4, SF_6, CHF_3 (with threshold values of the bombarding ion energy of 10–20 eV), CO and CO_2 [at a pressure of 60–80 Pa and $T > 200$ K the etching rate for the plane (0001) is 10^{-5}–$4 \cdot 10^{-4}$ cm/s], as well as BCl_3, BBr_3 (the etching rates are 1.5 nm/s at 310 K and HF power of W/cm^2) are used. The time dependences of the thickness of the etched-off layer are shown in Fig. 2.104.

Magnetic plasma etching through a mask is used for etching bands with a width of about 5 μm in sapphire substrates. For this purpose the gas mixture of 20% of Cl and 80% of BCl is applied.
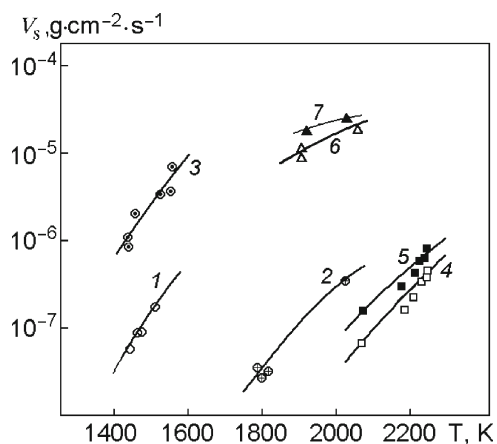
Fig. 2.103 Etching rate for different planes of sapphire depending on the temperature at a constant pressure [122]: (*1*) (0001), P= 4–6 $\cdot$ 10^{-2} Pa; (*2*) (0001), P= 1–3 $\cdot$ 10^{-1} Pa; (*3*) (0001), P= 1–4 Pa; (*4*) (0001), P= 10–40 Pa; (*5*) (11$\bar{2}$0), P = 1–4 Pa; (*6*) (0001), P = 60–80 Pa; (*7*) (1$\bar{1}$02), P= 60–80 Pa
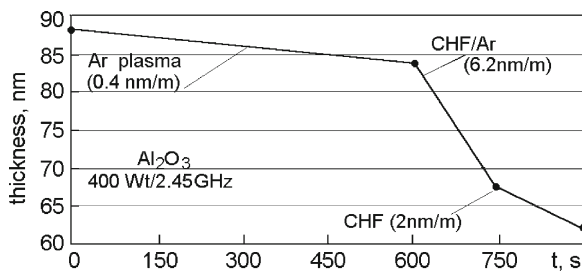
Fig. 2.104 Dependence of the thickness of etched sapphire layer on the time of ion action

Fig. 2.105 Evaporation forms on annealed sapphire ball. Isolated vertexes: c: 0001; R: $01\bar{1}2$, r: $10\bar{1}1$, a: $01\bar{1}2$, π: $1\bar{1}02$, s: $11\bar{2}3$, n: $2\bar{2}43$
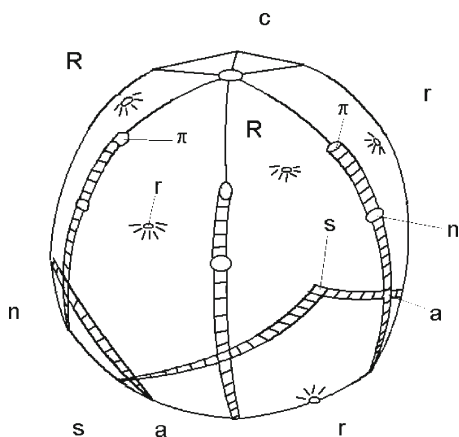
Evaporation forms of the crystals are similar to the dissolution forms. The mechanisms of evaporation and dissolution seem to be analogous. First, the surface areas with elevated energy are removed. At dissolution in mother liquor medium, the growth and the dissolution forms completely coincide. When the chemical composition of the medium is changed, the dissolution and evaporation forms may change, too. The evaporation form of a sapphire ball in hydrogen or in carbon-containing medium is a combination of isolated vertexes (Fig. 2.105) [124].

The rate of Langmuir evaporation of the plane $(10\bar{1}0) > (\bar{2}110) > (0001)$ [125]. The evaporation morphologies of the planes $(10\bar{1}0)$ and $(\bar{2}110)$ correspond to the layer mechanism; one of the facets (0001) has the monolayer (normal) mechanism. The evaporation energy is 210 ± 20 kcal/mol.

Al_2O_3 molecule has an essentially higher value of formation heat (377 kcal) in comparison with other oxides (e.g., 177 and 192 kcal for Fe_2O_3 and SiO_2, respectively); therefore, it is more difficult to reduce sapphire to the metal.

2.2.3 Corrosion Resistance

Sapphire possesses sufficient resistance to sulfur vapor up to ~1,300 K; to sodium and potassium up to 1,100 K (in Na melt its mass diminishes by 1% during 160 h at 1,200 K); to tin up to 2,200 K; in lead and bismuth up to 1,300 K; in caustic soda up to 1,100 K; in iodine and iodides up to 1,300 K; in hydrogen sulfide and CO_2 up to 1,500 K; and in titanium tetrachloride at 1,300–1,400 K. Constructional sapphire components work in Mg, Al, Cr, Co, Ni, Cs, Pb, Bi, and Zn melts and in their alloys, as well as in rare earth, cast iron, and steel melts. The crystals are resistant to hot water solutions and melts of a number of compounds (Table 2.27, Fig. 2.106).

Corrosion resistance of sapphire surface. As sapphire is widely used in chemical technologies; it is necessary to know the conditions of maximum corrosion resistance of the surface of sapphire products. Corrosion resistance of sapphire to different aggressive media has been studied [112–114], but the obtained data concern the bulk resistance.

The resistance of the surface to aggressive media is influenced by the defectiveness of the surface-adjacent layer formed at mechanical treatment. Moreover, it

Table 2.27 Loss of mass under the action of chemical reagents (%)

Reagents	T (K)	Time of action (h)	Loss of mass	
			Sapphire[a]	Ruby[b]
Boiling in water solutions				
HNO_3 (1:4.6)	400	6.6	0.01	0.03
HNO_3 (1:1)	400	6.0	0.01	0.03
KOH (70%)	400	6.0	0.01	0.03
H_2SO_4 (1:9)	400	6.0	0.01	0.03
HCl (1:1)	400	6.0	0.01	0.03
HF (1:1)	400	6.0	0.01	0.06
Fusing				
Lithium metaborate	1,300	1.0	93.4	–
Lithium megaphosphate	1,300	1.0	7.2	10.0
Potassium hydrosulfate	1,100	0.7	2.4	4.1
Boron anhydrite	1,200	0.7	4.2	0.03
Na_2O_2 + soda 1:5	900	0.25	0.5	0.2
NaF	1,300	1.0	4.1	11.2
H_3PO_4	600	1.0	0.2	–
HCl	1,100	1.0	0.05	0.03
LiF	1,200	1.0	0.4	1.0
Holding in melts				
Copper	1,350	4.0	0.05	–
Steel St3	1,900	4.0	0.02	–
Ni:Cr	1,500	4.0	0.01	–
Carbon steel	1,900	4.0	0.13	–

[a]~7 cm^2 working surface
[b]~2 cm^2 working surface
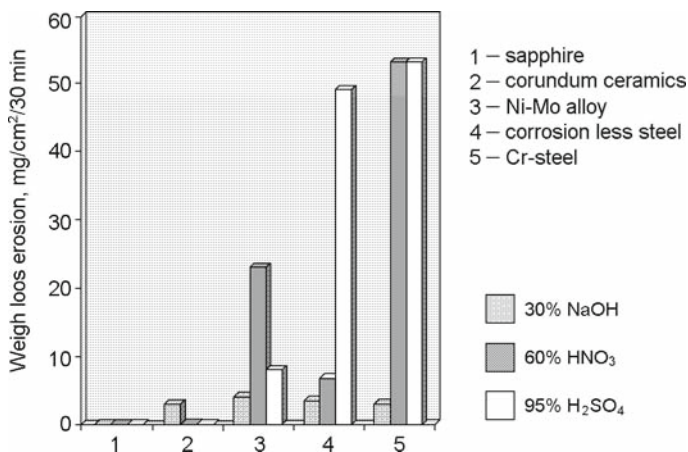
Fig. 2.106 Erosion resistance of sapphire in acids and alkalis

depends on the bulk structure defects that reach the surface; the density and distribution of such defects depend on the crystal growth method. Sapphire is anisotropic; therefore, it is necessary to take into account the nature of atomic bonds of the crystallographic planes, their electronic structure, and energy properties.

To study the influence of the mentioned factors, the crystals were grown by different methods from the same raw material, i.e., the crystals obtained by the Verneuil method. The growth medium was reductive (the Verneuil method), vacuum (the Kyropoulos and HDS methods), and argon (the Stepanov method). The samples of different crystallographic orientations were treated to obtain different degrees of roughness. For comparison, smooth basal and prism planes wedged out in the process of crystal growth were considered. The crystals with the maximum anionic nonstoichiometry were obtained by annealing at 2,253 K in $CO + CO_2$ medium at a residual pressure of 60 Pa. The crystals possessing the maximum cationic nonstoichiometry were produced by annealing in oxidative medium at 2,023 K; the content of O_2 in the annealing space was 12–15 vol%. The influence of point defects was studied by changing the density of cationic and anionic vacancies [125].

The corrosion resistance of the surface was investigated by the method of layer-by-layer etching using 0.3 ml of condensed phosphoric acid spread onto the surface of the sample [100]. After holding the sample at 573 K during 30 min, the film that formed on its surface was dissolved in bidistilled water. The degree of surface destruction was determined from the content of aluminum in the solution. The process of etching was repeated six times. The thickness of the dissolved layer (h, cm) was determined using the ratio:

$$h = \frac{m \cdot 1.89}{\gamma \pi r^2} \qquad (2.26)$$

where $1.89 = Al_2O_3/2Al$ is the ratio of molecular masses; m is the average value of aluminum mass that passed into solution at one etching process; $\gamma = 3.98$ g/cm^3 is the density of Al_2O_3; and r is the radius of the sample, cm. The relative standard deviation from a single result of the measurement of h is 0.15.

The rate of the chemical reaction is a function of the surface energy and of the strength of the crystal lattice bond. It depends on the degree of destruction of the surface and the surface-adjacent layer. Mechanical treatment decreases the strength of the surface more than by two times (Table 2.28), depending on the degree of its destruction.

It is known that dislocations reaching the surface increase the rate of its dissolution. However, at $\rho = 10^3$–10^5 cm^{-2} this dependence is barely noticeable for the same crystallographic plane (Table 2.29). Not only dislocations but also 1.00-mm pores that reach the surface do not have a significant influence on the value of corrosion resistance. The contribution of pores cannot be considered decisive either. An essential increase in the content of chromium apparently raises the strength of the plane $(10\bar{1}0)$ but does not influence the plane (0001) (Table 2.30). Moreover, the value of corrosion resistance is not noticeably influenced by point defects in the form of anionic and cationic vacancies.

At the same treatment, a decisive contribution to the corrosion resistance of the surface belongs to their crystallographic orientation. Irrespective of the methods of crystal growth and thermal treatment, the value of h for the plane (0001) is 0.72–

Table 2.28 Corrosion resistance of sapphire surface depending on the type of treatment [Kyropoulos method, (0001) plane]

Type of treatment	Damaged layer depth (μm)	Thickness (h) of layer removed at one etching act (μm)
Natural facet	0	0.72
Polishing	1–5	0.77
Fine lapping	20–30	0.96
Rough lapping	>40	1.8

Table 2.29 Corrosion resistance of sapphire surface depending on dislocation density

Growth method	ρ (cm^{-2})	Plane	Type of surface treatment	h (μm)
Verneuil	$(1$–$5) \cdot 10^5$	(0001)	Polishing	0.75
			Natural facet	0.82
Kyropoulos	10^3	(0001)	Polishing	0.77
			Natural facet	0.72
HDS	$5 \cdot 10^3$	(0001)	Polishing	0.83
Stepanov	10^5	(0001)	Polishing	0.73
			Natural facet	0.72
	10^5	$(10\bar{1}0)$	Polishing	0.29
		$(10\bar{1}0)$	Natural facet	0.23
	10^5	$(11\bar{2}0)$	Polishing	0.15
		$(11\bar{2}0)$	Natural facet	0.12

Table 2.30 Corrosion resistance of the surface of doped sapphire grown by Verneuil method

Crystal	Content of doping addition (mass%)	Plane	h (µm)
Al_2O_3	$1 \cdot 10^{-4}$	$(10\bar{1}0)$	0.25
	$1 \cdot 10^{-4}$	$(000\bar{1})$	0.80
Al_2O_3:Cr	$1 \cdot 10^{-1}$	$(10\bar{1}0)$	0.25
	$6 \cdot 10^{-4}$	$(10\bar{1}0)$	0.20
	1.3	$(10\bar{1}0)$	0.12
	1.3	$(000\bar{1})$	0.80
Al_2O_3:Ti	$6 \cdot 10^{-2}$	$(10\bar{1}0)$	0.24
	$6 \cdot 10^{-2}$	(0001)	0.80

Table 2.31 Dependence of V_s of aluminum oxide on crystallographic parameters at etching with $K_2S_2O_7$ (870 K, 1 min)

Crystallographic plane	V_s (µm/min)	Character of etching	Reference
(0001)	2.18 ± 0.2	Selective	[119]
$(10\bar{1}0)$	1.03 ± 0.5	Polishing	[119]
$(11\bar{2}0)$	0.95 ± 0.2	Polishing	[126]
70–80° deviation from C-axis	1.33 ± 0.5	Mixed	[126]

0.83 µm; for the planes $(11\bar{2}0)$ and $(10\bar{1}0)$ it equals 0.12–0.15 and 0.12–0.29 µm, respectively. These data agree with the results of etching sapphire surface by potassium bisulfate which is a stronger etchant (Table 2.31).

Corrosion is caused by a number of surface phenomena. The atomic structure in the vicinity of free surface is distinguished by surface relaxation (decrease of the interplanar distances in the surface-adjacent atomic nets) and reconstruction (change of the symmetry in the surface-adjacent layers) characteristic of the crystals with covalent bond. These phenomena raise the surface energy proportionally to the reticular density of the crystallographic planes.

An approximate measure of the surface energy is the quantity of free bonds per unit of the surface. According to some estimations [17], the maximum quantity of such bonds in the plane (0001) is 6.6; in the plane $(10\bar{1}0)$ it is 5.2. Therefore, the plane (0001) has the lowest corrosion resistance. In the direction of the most closely packed row of the lattice, the work necessary for escape of the atoms out of the plane is the least and the process of destruction is the fastest [127]. Another origin of an abnormally low strength of the basal plane is revealed while examining flat nets composed of aluminum and oxygen ions.

In the planes (0001) and $(10\bar{1}0)$ such nets are formed by the atom O–Al–Al–O–Al–Al–O and Al–O–Al–O, respectively. The nets $(10\bar{1}0)$ are electrostatically neutral. In the plane $(11\bar{2}0)$ Al– and O– nets alternate with each other and form "packages." The boundaries of these "packages" are located between the flat nets formed by oxygen atoms.

Thus, the nets Al–Al lie only in the basal planes. The bond Al–Al is weaker than Al–O not only chemically, but also mechanically. While examining the surface

bonds of the last layer and of some previous layers in the semiendless lattice, it is established [14] that the chipping energy of the plane (0001) is the lowest in the Al layer. The energy of Al_2O_3 lattice is high enough (152 eV). The total contribution of Al^{3+} to the potential ion energy exceeds the one of O^{2-}, but the contribution of the van der Waals energy for O^{2-} (−1.3 eV) essentially exceeds that for Al^{3+} (−0.1 eV) [7]. Therefore, aluminum atoms from the nets Al–Al enter into the reaction more readily.

So, as concerns the technological factors, the most essential influence on the corrosion resistance of sapphire belongs to mechanical treatment. Rough lapping lowers the resistance of the crystal surface more than by two times. Crystallographic factors make a decisive contribution to the corrosion resistance. The resistance to aggressive media of different crystallographic planes differs by several times.

Interaction with tungsten is of great interest, because tungsten is one of a few constructional materials used at the growth and annealing of sapphire. The reaction proceeds according to the equations:

$$W + Al_2O_3 = 1/3(WO_3)_3 + 2Al \tag{2.27}$$

$$W + Al_2O_3 = 1/4(WO_3)_4 + 2Al \tag{2.28}$$

The results of the calculations of the isobar–isothermal potential ΔG_T for these reactions per one gram-atom of W and the temperature dependence of the rate of the interaction between W and Al_2O_3 are shown in Tables 2.32 and 2.33.

Loss of tungsten weight is expressed by the linear time dependence

$$d\Delta P/d\tau = K_i \tag{2.29}$$

where K_i is the interaction rate constant. This constant is practically independent of the mass of Al_2O_3 and the area of contact of the reagents (see Table 2.33). The time dependence of the specific weight loss ΔP is shown in Fig. 2.107.

The constant of the rate of the interaction at 2,473–3,473 K (Fig. 2.107b) is described by the equation:

$$K_i = 9.5 \times 10^2 \exp(-70,000/RT) \tag{2.30}$$

Table 2.32 Change of the isobar-isothermal potential of W + Al_2O_3 reaction

	Change in ΔG_T (cal/g at. W)	
T (K)	For reaction (2.25)	For reaction (2.26)
2,100	+157.00	+157.10
2,300	+147.00	+147.10
2,500	+139.00	+139.10
2,700	+131.00	+131.15
2,900	+124.00	+124.15
3,100	+116.00	+116.20
3,300	+107.00	+107.20
3,500	+99.00	+99.25

Table 2.33 Temperature dependence of the rate of interaction between W and Al_2O_3 in vacuum (10^{-4} mHg) [126]

T (K)	Area of contact (cm²)	$K \cdot 10^3$ g/(cm² min) at different masses (g)		
		0.3	0.7	1.0
2,073	2	–	0.056	–
	4	0.055	0.055	0.057
2,273	2	–	0.21	–
	4	0.20	0.21	0.22
2,473	1	–	0.8	–
	2	0.7	0.9	0.8
2,673	1	–	2.1	–
	2	2.4	2.0	2.1
2,873	1	–	5.6	–
	2	5.4	5.5	5.5
3,073	1	9.2	9.1	9.1
3,273	1	25.0	24.9	25.2
3,373	1	47.6	50.1	52.4
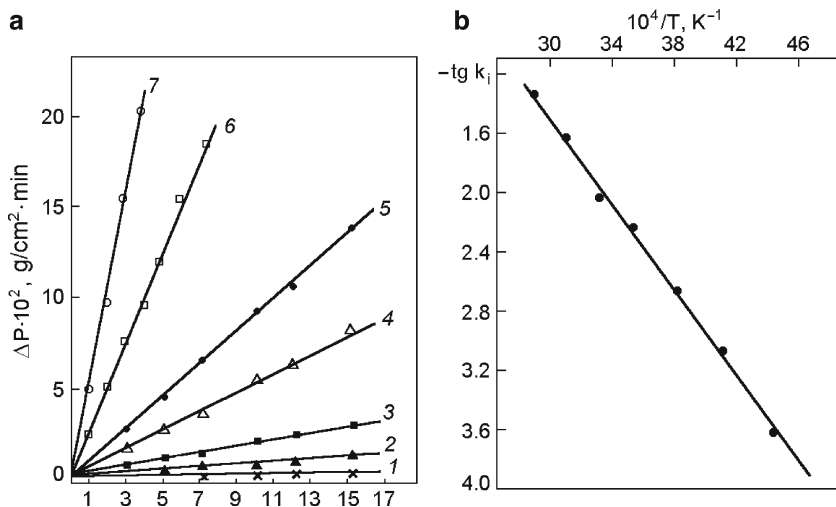
Fig. 2.107 (**a**) Kinetics of the interaction of tungsten with Al_2O_3 (time dependence of the specific weight loss ΔP). (*1*) 2,273 K; (*2*) 2,473 K; (*3*) 2,673 K; (*4*) 2,873 K; (*5*) 3,073 K; (*6*) 3,273 K; (*7*) 3,473 K. (**b**) Temperature dependence of the interaction rate K_i

As follows from Fig. 2.106, for different aggregative states of Al_2O_3, the dependence of lg K_i on $1/T$ is linear. This testifies to the fact that the interaction between W and Al_2O_3 proceeds by the same mechanism within the whole of the temperature interval.

The interaction reaction has the following stages:

• Dissociative evaporation of Al_2O_3

- Chemical adsorptive action
- Desorption and migration of the reaction products

The activation energy at the interaction of a one-atom substance with a two-atom molecule can be calculated using the empirical formula [128]

$$E_a = 1/4 D_{xy} \tag{2.31}$$

where D_{xy} is the dissociation energy of XY molecule.

Al_2O_3 molecule has the structure:

$$\begin{array}{ccc} Al & - O - & Al \\ \parallel & & \parallel \\ O & & O \end{array}$$
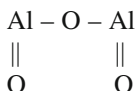
As $D_{Al_2O_3} = 740$ kcal/mol, an average energy of 123 kcal corresponds to one bond. In a first approximation the interaction energy can be presented in the following form:

$$W + Al_2O_2 = O \rightarrow (WO_3)_3 + Al \tag{2.32}$$
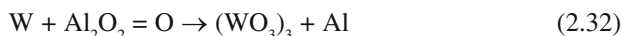
where $Al_2O_2 = O$ is the two-atom molecule consisting of an oxygen atom and Al_2O_2 "atom."

For such a molecule $D_i \sim 250$ kcal/mol. As follows from formula (2.31), $E_a \sim 63$ kcal/mol, which is in a good agreement with the experimentally defined value $E_a \sim 70$ kcal/mol [129]. Thus, it can be assumed that the limiting stage of the process is dissociative evaporation of Al_2O_3 with an activation energy of about 70 kcal/mol.

References

1. Klassen-Neklyudova M.V., Bagdasarov Kh.S. (eds.). Ruby & Sapphire: A Coll. Book. Moscow: Nauka, 1974.
2. Aldeberi P., Traverse J.P. J. Am. Ceram. Soc. 65(9), 1982, pp. 460–464.
3. Ishizawa N., Miyata T., Minato I. et al. Acta Crystallogr. 36(2), 1980. pp. 228–230.
4. Belov I.V. Structure of Ionic Crystals and Metallic Phases. Moscow: USSR Academy of Sciences, 1947.
5. Shvid'ko Yu.V., Lucht M., Gerdau E. et al. J. Synchr. Rad. 9, 2002, pp. 17–23.
6. Lucht M., Lerche M., Wille H.C. et al. J. Appl. Cryst. 36, 2003, pp. 1075–1081.
7. Dienes G.I., Welch D.O. Phys. Rev. 7, 1975, pp. 3060–3070.
8. Kislov A.N., Mazurenko V.G., Korzov K.N. et al. Fizika tverdogo tela. 45(9), 2003, pp. 1696–1699.
9. Loong C.-K. J. Eur. Ceram. Soc. 19, 1999, p. 2241.
10. Stashans A., Kotomin E.K., Calais J.L. Phys. Rev. B. 49, 1994, p. 14854.
11. Xu Yong-Nain, Gu Zhong-Quan, Zhong Xue-Fu, Ching W.Y. Phys. Rev. B. 56, 1997, p. 7277.
12. Seitz F. Modern Theory of Solid. New York: McGraw-Hill, 1940, 83pp.
13. Lagerlof K.D.P., Mitchell T.E., Heuer A.H. et al. Acta met. 32, 1984, pp. 197–105.
14. Gue J., Ellis D., Lam D. Phys. Rev. B. 45, 1992, pp. 13647–13656.
15. Gumilevskiy A.A. Watches and Watch Mechanisms. 1(131), 1962, pp. 26–29 [in Russian].
16. Wiederhorn S.M. J. Am. Ceram. Soc. 59, 1969, p. 485.
17. Hartman P. Proceedings of Mineralogical Society. Leningrad: USSR Academy of Sciences. 91(6), 1962, pp. 672–682 [in Russian].

18. Bakholdin S.I., Galaktionov E.V., Krymov V.M., et al. Izv. AN SSSR, Ser. Fiz. 58, 1994, pp. 32–41.
19. Kozlovskaya E.P. Ph.D. Thesis. Moscow: Institute for Crystallography, USSR Academy of Sciences, 1971.
20. Scheuplein R., Gibbs J. J. Am. Ceram. Soc. 47, 1964, p. 81.
21. Seong-Young Yoon, Jong-Yound Lee. J. Mat. Res. 11, 2001, pp. 221–226.
22. Antonov P.I. et al. Production of Profiled Single Crystals and Articles Therefrom. Leningrad: Nauka, 1981. p. 108.
23. Kotchik D., Tresler R., Barber D. J. Mater. Sci. 17(7), 1982, pp. 1977–1987.
24. Young S.Y., LeeJ.Y. J. Korean Association of Crystal Growth. 10(4), 2000, pp. 337–343.
25. Kuandykov L.L. Study of Sapphire Strips Growing by Stepanov Technique at Different Orientations. D. Thesis. St. Petersburg, A.F.Ioffe FTI, 2004 [in Russian].
26. Blistanov A.A. Crystals of Quantum Electronics. Moscow: MISIS, 2000 [in Russian].
27. Harris D.C. Proceedings of SPIE Conference on Window and Dome Technologies and Materials VI, 1999. 3705, 1999, pp. 2–11.
28. Harris D.C., Shmid F., Black D. et al. Proceedings of SPIE Conference on Window and Dome Technologies and Materials VII, 2001. 3050, 2001, pp.226–235.
29. Regan T.M., Harris D.C., Stroud R.M. et al. Proceedings of SPIE Conference on Window and Dome Technologies and Materials VII, 2001. 4375, 2001, pp. 31–40.
30. Hartman R., Perdok D.C. Acta Crystallogr. 8, 1955, p. 521.
31. Renaudo C., Orione P., Causa M. J. Cryst. Growth. 244, 2002, pp. 53–62.
32. Mackrodt W.C., Davey R.J., Black S.N., Docherty R. J. Cryst. Growth. 80, 1987, pp. 441–446.
33. Hartman P., Bennema P. J. Cryst. Growth. 49, 1980, p. 145.
34. Hartman P. J. Cryst. Growth. 49, 1980, p. 166
35. Jung-Hae Choi, Doh-Yeon Kim, Bernard J., Hockey et al. J. Am. Ceram. Soc. 80(1), 1997, pp. 62–68.
36. Kitayama M., Glaeser A.M. J. Am. Ceram. Soc. 88(12), 2005, pp. 3492–3500
37. Jung-Hae Choi, Doh-Yeon Kim, Bernard J., Hockey et al. J. Am. Ceram. Soc. 85(7), 2002, pp. 1841–44.
38. Chuhrov F.V. Minerals: A Reference Book, Vol.2. Moscow: Nauka, 1965, p.65.
39. Galmarini S., Aschauer U., Bowen P., Parker S.C. Poster, Switzerland, 2005. Lausanne, Bath.
40. Kanevsky V.S., Krivonosov E.V., ALitvinov L., Tkachenko S.A. Funct. Mater.. 6, 1999, pp. 370–373.
41. Kanevsky V.S, Krivonosov E.V., Lytvynov L.A.,Tkachenko S.A. Funct. Mater. 7, 2000. p. 156.
42. Belustin A.V. IKAN SSSR Trans. 8, 1953, pp. 247–252.
43. Borodenko Yu.A. Ph.D. Thesis. Kharkov: Institute For Single Crystals. 1986, 148pp.
44. Tkachenko S.A. Ph.D. Thesis. Kharkov: Institute For Single Crystals. 2000, 190pp.
45. Nicoara J., Nicoara D., Sofonea V. J. Cryst. Growth. 104, 1990, pp. 169–174.
46. Dobrovinskaya E.R., Litvinov L.A., Pishchik V.V. Encyclopaedia of Sapphire. Kharkov, 2004, 500pp [in Russian].
47. Malitson I.H. Opt. Soc. Am. 52, 1962, p. 1377.
48. Thomas M.E., Andersson S.K., Sova R.M., Joseph R.I. SPIE, 1997. 3060, 1997, p. 258.
49. Yang D., Thomas M.E., Kaplan S.G. Proceedings of SPIE, 2001. 4375, 2001, p. 53
50. Gravnak D.A., Burch D.E. JOSA. 55, 1965, p. 625.
51. Lingart Yu.K. Sci. Dr. Thesis. Moscow. 1990, 486pp.
52. Es'kov E.V., Sabelnikova M.M., Ignatov Yu.A. VI International Conference on Chemistry of Solids, Kislovodsk, Russia, 2006, p. 510.
53. Harris D. Proceedings of SPIE, 1999. 3705, 1999, p. 786.
54. Flerov V.I., Flerov A.V., Konyaev V.M et al. Kristallografia. 38(1), 1993. pp. 222–228.
55. Sirota N.N., Zhdanov E.F. Dokl. AN BSSR. 11, 1967, pp. 772–773.
56. Muminov V.A., Tursumetov M.A. Izv. AN UzbSSR, Ser. Fiz.-Math. 3, 1977, pp. 60–63.

57. Kviatkovskiy S.F., Konevskiy V.S., Krivonosov E.V., Litvinov L.A. Zh. Prikl. Spektroskopii. 51, 1989, pp. 90–94.
58. Vakhidov Sh.A., Khattamov D.R., Yangibaev M. Izv. AN UzbSSR, Ser. Fiz.-Math. 4, 1976, pp. 65–67.
59. Bayramov B.Kh., Ubaydullaev Sh.B., Khoshkhozhev Z.M. Fiz. Tverdogo Tela. 18, 1976, pp. 2019–2023.
60. Gulchuk P.F., Litvinov L.A., Chernina E.A. Zh. Prikl. Spektroskopii. 43, 1985, pp. 132–134.
61. Pugets A.N., Springis M.I., Valbis J.A. Phys. Stat. Sol. A62, 1980, pp. k85–k87.
62. Evans B.D., Stapelbrock M. Solid State Comm. 33, 1980, pp. 765–770.
63. Springis M.I., Valbis J.A. Phys. Stat. Sol. 123(b), 1984, pp. 335–343.
64. Litvinov L.A., Chernina E.A. Ukr. Fiz. Zhurn. 30, 1985, pp. 811–814.
65.   Aluker E.D., Gavrilov V.V., Konevskiy V.S. et al. Optika i Spektroskopia. 70, 1991, pp. 75–81.
66. Hughes A.E. Radiat. Eff. 97, 1986, pp. 161–173.
67. Gumenjuk A.F., Kutovyi S.Y., Grebenovych M.O. Funct. Mater. 12, 2005, pp. 72–77.
68. Voloshin A.V., Litvinov L.A. Funct. Mater. 9, 2002, p. 555.
69. Voronkova E.M., Grechushnikov V.I., Distler G.I., Petrov I.P. Optical Materials for Infrared Engineering. Moscow: Nauka, 1965, p. 268 [in Russian].
70. Butabaev Sh.M., Perelomova N.V., Smyslov I.I. Kristallografia. 14, 1972, pp. 678–679.
71. Borden M.K., Askinazi J. Proceedings of SPIE 1997. 3060, 1997, p. 246.
72. Jacoby K.T., Goodrich S.M. Proceedings of SPIE 2005. 5786, 2005, pp. 188–194.
73. Klein C.A., Schmid F. Proceedings of SPIE 2005. 5786, 2005, pp. 17.
74. Glushak B.L.et al. Study of Material Strength under Dynamic Loadings. Novosibirsk: Nauka. 1992, p. 294 [in Russian].
75. Loveridge-Smith A. et al. Phys. Rev. Lett. 86, 2001, p. 2349.
76. Glushak B.L., Novikov S.A., Ruzanov A.I., Sadyrin A.I. Failure of Strainable Media under Pulse Loadings. Nizhny Novgorod: Nizhegorodsky University, 1992, 192pp [in Russian].
77. Dobrovinskaya E.R., Litvinov L.A., Pishchik V.V. Sapphire and Other Corundum Crystals. Kharkov: Institute of Single Crystals, Folio Publ, 2002, p. 300.
78. Krzhizhanovskiy R.E., Shtern Z.Yu. Thermal-Physic Properties of Non-Metal Materials. Leningrad: Energia, 1973, p. 333.
79. White G.K., Roberts R.B. High Temp. High Pressure. 15, 1983, p. 321.
80. Tolmachev A.M., Kiryanova E.A., Litvinov L.A. Kristallografia. 39, 1994, p. 150.
81. Kompan T.N., Korenev A.S., Lunin A.Ya. et al. Izmeritelnaya Tekhnika, 8, 1999, pp. 38–42.
82. Votinova V.V., Ignatov D.V. Transactions of A.A. Baykov Institute for Metallurgy, Moscow, USSR Acad. of Sciences Publ. 1961. 8th Issue. P. 263–268.
83. Reedy K.P.R., Cooper A.B. J. Am. Ceram. Soc. 65, 1982, p. 634.
84. Reed D., Wuensch B., Bowen H. Annual Report M.J.T. Research in Materials. 1978, p. 241.
85. Frishchat A.N. Ber. Dent. Keram. Aes. 44, 1971, p. 441 [in German].
86. Masataka Ohkubo, Tansumi Hioki, Jun-ichi Kawamoto. J. Appl. Phys. 60(4), 1986, pp. 1325–1335.
87. Compbell N.E. (ed.), High TEmperature Engineering Misscow: IL Publ. 1959, P. 75 [Russian Translated Edition is cited]
88. Papis J., Kingary W.D. J. Am. Ceram. Soc. 44, 1961, p. 459.
89. Kitazawa K.R.L. Coble Am. Ceram. Soc. 57, 1974, pp. 245–250.
90. Abdukadirova I.Kh. The Fifth International Conference on Modern Problems of Nuclear Physics, Samarkand, 2003, pp. 161–162.
91. Abdukadirova I.Kh Pis`ma Zh. Tekhn. Fiz. 26, 2003, p. 17.
92. Abdukadirova I.Kh. Superhard Mater. 1, 2004, p. 12.
93. Urusov V.S., Kravchuk I.F. Geokhimia. 8, 1976, p. 1204.
94. Litvinov L.A. Ruby: Production and New Application Fields. Moscow: NIITEKHIM, 1978, p. 73 [in Russian].
95. Litvinov L.A. Everything About Ruby. Kharkiv: Prapor. 1991, p. 150 [in Russian].

96. Kulagin N.A., Sviridov D.T. Electron Structure Calculation Methods for Free and Impurity Ions. Moscow: Nauka, 1986, p. 202 [in Russian].
97. Bartran R.H., Swenberg C.E., Fournier J.T. Phys. Rev. A139(3), 1965, pp. 941–948.
98. Smite R. J. Biomed. Mater. Res. 21, 1987, p. 917.
99. Voloshin A., Lytvynov L. Funct. Mater. 9, 2002, p. 554.
100. Litvinov L., Druzenko T., Potapova V., Blank A. Crystallogr. Rep. 46, 2001, p. 346.
101. Wolff G.A., Frawley J.J., Heitanen J.R. J. Electrochem. Soc.111, 1964, pp. 22–27.
102. Lavizzari G. Nouveaux phenomenes des corps cristallises, Lugano, 1865.
103. Izmailova V.N., Yampolskaya G.P., Summ B.D. Surface Phenomena in Protein Systems. Moscow: Khimia, 1988 [in Russian].
104. Heimann R.B. Aufloesung von Kristallen. Springer, Wien. New York, 1975.
105. Siesmayer B. Diss. Freie Universitat Berlin. – 1973.
106. Ardamatsky A.L. Diamond Treatment of Optical Elements. Leningrad: Mashinostroenie, 1978 [in Russian].
107. Siesmayer B., Heimann R., Franke W., Lacmann R. J. Cryst. Growth. 28, 1975, pp. 157–161.
108. Berezhkova G.V. et al. IV All-Union Conference on Crystal Growth, Vol. 2 Erevan, 1972, p.39.
109. Liesmayer R., Heimann R., Franke W., Lacmann. J. Cryst. Growth. 28, 1975, p. 157.
110. Govorkov V.R., Smirnova A.E. Kristallografia. 24, 1979, pp. 1095–1097.
111. Rumyantsev V.N. Kristallografia. 20(4), 1975, pp. 870–872.
112. Blank A.B., Litvinov L.A., Pishchik V.V. et al. Zavodskaya Laboratoriya. 8, 1992, pp. 6–8.
113. Blank A.B. Analytical Chemistry in the Studies and Production of Inorganic Functional Materials. Kharkiv: Institute for Single Crystals Publication, 2005, 350pp [in Russian].
114. Timofeeva V.A. Crystal Growth from Solutions—Melts. Moscow: Nauka, 1978, p. 77.
115. USA Patent 3, 753, 775, 1973.
116. Osinskiy V.I., Goncharenko T.I., Lyakhova I.N. PSE. 1, 2003, pp. 93–99 [in Russian].
117. Champion J.A., Clemence M.A. J. Mater. Sci. 2, 1967, p. 153.
118. Japan Patent 4,011,099, 1977.
119. Ryabov A.N., Kiseleva T.I., Kulikova L.B. Zh. Prakt. Khimii. 48, 1975, pp. 407–408.
120. Krasheninnikov A.A. Thesis. Leningrad: LTI, 1973.
121. Batygin V.I., Kulikov V.I., Kulikova S.V. et al. Fizika i Khimia Obrabotki Materialov. 2, 1978, pp.126–130.
122. Sidelnikova N.S., Adonkin G.T., Budnikov A.T. et al. Funct. mater. 4, 1997, pp. 92–96.
123. Beletskiy A.S., Litvinov L.A., Chernina E.A. USSR Inventor's Certificate 1522805, 1989 [in Russian].
124. Voytsekhovskiy V.N. Kristallografia. 13, 1968, pp. 563–565.
125. Konevskiy V.S., Krivonosov E.V., Litvinov L.A. Izv AN SSSR, Neorganicheskie Materialy. 25, 1989, p. 1486.
126. Goryachkovskiy Yu.G., Kostikov V.I., Mitin B.S. et al. Fizika i Khimia Obrabotki Materialov. 4, 1978, pp. 70–74.
127. Tamman G., Botschwar A.A. Z. Anorg. Allg. Chem. 146, 1925, p. 420.
128. Glesston C., Leidler K., Eyring G. Theory of Absolute Reaction Rates. Moscow: IL, 1948, 583pp [Rusisan Translated Edition is Cited].
129. Hart P.B. Br. J. Appl. Phys. 18, 1967, p. 1389.
130. Kingary W.D., Bowen H.K., Uhlmann D.R. Introduction to Ceramics, 2nd ed. 1976, New York: Willey.
131. Bond W.L.. Crystal Technology. Wiley, New York,1980.
132. Handbook of Optics, Vol 2, Ch. 33, McGraw-Hill, 1995.

Appendix

Table 2.34 Coordinates of ions of two molecules in the rhombohedral unit cell α-Al$_2$O$_3$, α = 5,124 Å. Origin of coordinates is in the rhombohedron vertex [7]

Ion	Type	x	y	z
1	Al	0	0	0.3750
2	O	−0.2457	−0.1418	0.6334
3	O	0.2457	−0.1418	0.6334
4	O	0	0.2837	0.6334
5	Al	0	0	0.8918
6	Al	0	0	0.3750
7	O	0.2457	0.1418	−0.6337
8	O	−0.2457	0.1418	0.6337
9	O	0	−0.2837	−0.6337
10	Al	0	–	−0.8918

Table 2.35 Interplanar distances in α-Al$_2$O$_3$. Cu-radiation

d	I/I_0	(hkl)	$(hkil)$	θ	2θ
3.479	75	012	01$\bar{1}$2	11°32′	23°4′
2.552	90	104	10$\bar{1}$4	15°50′	31°40′
2.379	40	1110	11$\bar{2}$0	17°1′	34°2′
2.165	<1	006	0006	18°45′	37°31′
2.085	100	113	11$\bar{2}$3	19°30′	39°
1.964	2	202	20$\bar{2}$3	20°15.5′	40°31′
1.74	45	024	02$\bar{2}$4	23°35′	47°10′
1.601	80	116	11$\bar{2}$6	25°46′	51°32′
1.546	4	211	21$\bar{3}$1	26°46′	53°32′
1.514	6	122	12$\bar{3}$2	27°22.5′	54°45′
1.51	8	018	01$\bar{1}$8	27°27′	54°54′
1.404	30	124	12$\bar{3}$4	29°43′	59°26′
1.374	50	030	03$\bar{3}$0	30°26′	60°52′
1.337	2	124	12$\bar{3}$5	31°22′	62°44′
1.276	4	208	20$\bar{2}$8	33°4′	66°8′
1.239	16	1.0.10	1.0.$\bar{1}$.10	34°11′	68°22′
1.2343	8	119	11$\bar{2}$9	34°20′	68°40′
1.1898	8	220	22$\bar{4}$0	35°49′	71°38′
1.16	<1	306	30$\bar{3}$6	36°52′	73°44′
1.147	6	223	22$\bar{4}$3	37°17.5′	74°35′
1.1382	2	311	31$\bar{4}$1	37°42′	75°24′
1.1255	6	312	31$\bar{4}$2	38°12′	76°24′
1.1246	4	128	12$\bar{3}$8	38°14.5′	76°29′
1.0988	8	0.2.10	0.2.$\bar{2}$.10	39°18.5′	78°37′
1.0831	4	0.0.12	0.0.0.12	39°59.5′	79°59′
1.0781	8	134	13$\bar{4}$4	40°13′	80°26′
1.0426	14	226	22$\bar{4}$6	41°53′	83°46′
1.0175	2	402	40$\bar{4}$2	43°10′	86°20′

Table 2.35 (continued)

d	I/I_0	(hkl)	$(hkil)$	θ	2θ
0.9976	12	1.2.10	$1.2.\bar{3}.10$	44°15′	88°30′
0.9857	<1	1.1.12	$2.2.\bar{4}.12$	44°55.5′	89°51′
0.9819	4	404	$40\bar{4}4$	45°9′	90°18′
0.9431	<1	321	$32\bar{5}1$	47°34′	95°8′
0.9413	<1	1.2.11	$1.2.\bar{3}.11$	47°42′	95°24′
0.9345	4	318	$31\bar{4}8$	48°9′	96°18′
0.9178	4	229	$22\bar{4}9$	49°20′	98°40′
0.9076	14	324	$32\bar{5}4$	50°5′	100°10′
0.9052	4	0.1.11	$0.1.\bar{1}.11$	50°16′	100°32′
0.8991	8	410	$41\bar{5}0$	50°44′	101°28′
0.8884	<1	235	$23\bar{5}5$	51°35′	103°10′

Table 2.36 Parameters of sapphire crystal lattice in 4.5 ... 375 K temperature interval

T (K)	a (Å)	c (Å)	T (K)	a (Å)	c (Å)
4.5	4.7562786	12.9819485	312.533	4.759636	12.992930
100.0	4.7563553	12.9823018	322.359	4.759884	12.993740
150.0	4.7566469	12.9834100	332.184	4.760158	12.994581
200.0	4.7572561	12.9854463	342.010	4.760427	12.995414
250.0	4.7581322	12.9883093	351.836	4.760705	12.996261
286.143	4.758977	12.990872	361.661	4.760976	12.997130
286.968	4.758998	12.990932	371.339	4.761251	12.998000
287.125	4.759001	12.990946	374.000	4.761310	12.998155
288.108	4.759020	12.991024	375.000	4.761341	12.998241

Table 2.37 Parameters of sapphire crystal lattice in 593–2,170 K temperature interval

T (K)	a (Å)	c (Å)	T (K)	a (Å)	c (Å)
593	4.767 ± 0.001	13.008 ± 0.003	1043	4.785 ± 0.001	13.054 ± 0.004
713	4.772 ± 0.001	13.021 ± 0.003	1253	4.794 ± 0.001	13.082 ± 0.004
883	4.775 ± 0.001	13.037 ± 0.004	2170	4.844	13.27

Table 2.38 Contributions of ions occupying different positions of sapphire crystal lattice, to the potential energy (eV) [7]

Ion and its position	Madelung energy	Repulsion energy	van der Waals energy	Total energy
Al^{3+} in the lattice	−109.8	19.5	−0.1	−90.4
O^{2-} in the lattice	−52.8	13.0	−1.3	−41.1
Al^{3+} in the octahedron interstice	−8.9	16.0	0.1	7.0
O^{2-} in the octahedron interstice	5.9	9.4	−3.6	11.7

Table 2.39 Parameters characterizing sapphire crystal lattice

Radius of Al^{3+}	0.51 Å
Area of Al^{3+}	$0.9 \cdot 10^{-16}$ cm^2
$2Al^{3+} + 3O^{2+}$ occupy	$19.9 \cdot 10^{-16}$ cm^2
Oxide formation heat	1,680 J/(g mol), 580 J/at.
Lattice energy	3,663–3,708
	(3,708–theoretical) kcal/mol
Covalent interaction energy	314 kcal/mol
Effective ion energy	381 kcal/mol
Atomization energy (experimental)	731 kcal/mol
Madelung constant	
Referred to the interatomic distance	$A_R = 25.155$
Referred to the rhombohedral cell parameter	$A_a = 66.92486$
Repulsion coefficient	1,941Å^{-1}
Compressibility coefficient	$0.32 \cdot 10^{-3}$ kbar^{-1}
Contact angle	
Angle of wetting with water	Sapphire (0001) – 84°
	Sapphire ($10\bar{1}2$) – 79°
	Sapphire ($10\bar{1}0$) – 78°
	Sapphire ($11\bar{2}0$) – 74°
	Ruby 0.1 Cr (0001) – 73°
Angle of wetting with glycerin	Sapphire (0001) – 73°
	Ruby 0.1 Cr (0001) – 63°
Energy of the surface (0001)[a]	4.83 J·m^2
Average surface energy at 2120 K[b]	0.9 J·m2

[a] Calculated by Hartman [34]
[b] Ref [132]
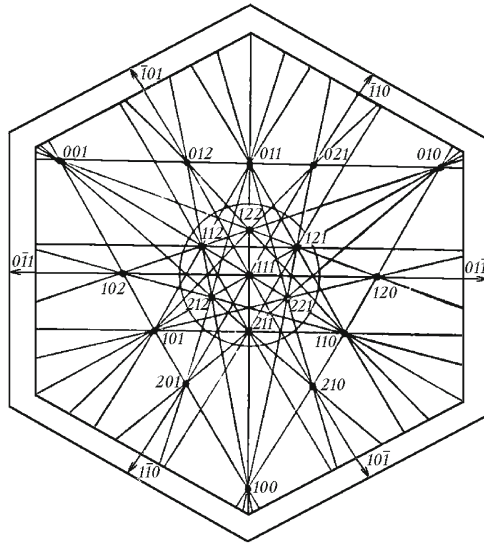
Fig. 2.108 Gnomonic projection of corundum that shows all F facets and zones parallel to chains with intense bonds

Table 2.40 Symbols of crystallographic planes in morphological and structural units

Hexagonal symbols of planes in unit		Rhombohedral symbols of planes in structural unit
Morphological	Structural	
$\{0001\}$	$\{0001\}$	$\{111\}$
$\{11\bar{2}0\}$	$\{11\bar{2}0\}$	$\{10\bar{1}\}$
$\{10\bar{1}0\}$	$\{10\bar{1}0\}$	$\{\bar{2}11\}$
$\{10\bar{1}1\}$	$\{10\bar{1}2\}$	$\{011\}$
$\{02\bar{2}1\}$	$\{10\bar{1}1\}$	$\{100\}$
$\{01\bar{1}2\}$	$\{10\bar{1}4\}$	$\{\bar{2}11\}$
$\{22\bar{4}3\}$	$\{11\bar{2}3\}$	$\{210\}$
$\{11\bar{2}3\}$	$\{11\bar{2}6\}$	$\{321\}$
$\{20\bar{2}5\}$	$\{10\bar{1}5\}$	$\{122\}$
$\{40\bar{4}1\}$	$\{\bar{2}021\}$	$\{\bar{1}11\}$
$\{21\bar{3}1\}$	$\{12\bar{3}2\}$	$\{21\bar{1}\}$
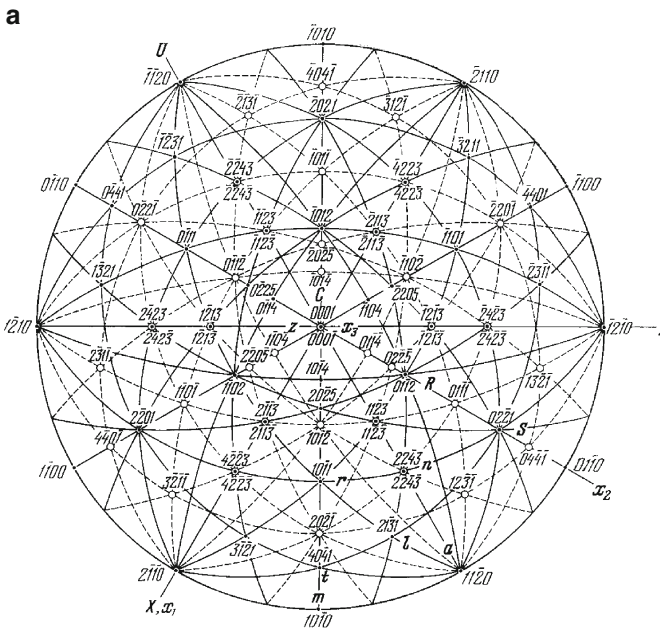
Fig 2.109 Stereographic projections of sapphire crystal lattice: (**a**) complete projection centered with respect to the basal plane (0001); (**b–f**) centering with respect to the planes of the negative rhombohedron $S(02\bar{2}1)$, the second-kind prism $a(11\bar{2}0)$, other negative rhombohedron $R(01\bar{1}2)$, the positive rhombohedron $(101\bar{1})$ and the first-kind prism $m(10\bar{1}0)$, respectively

b

c
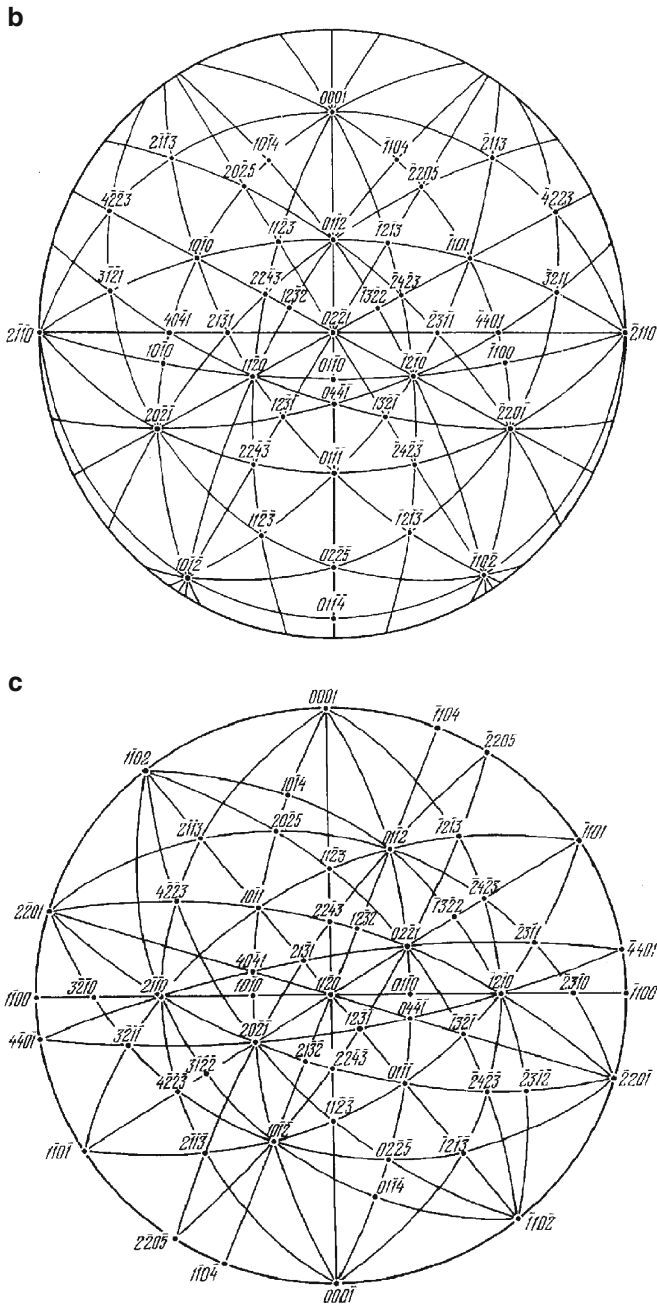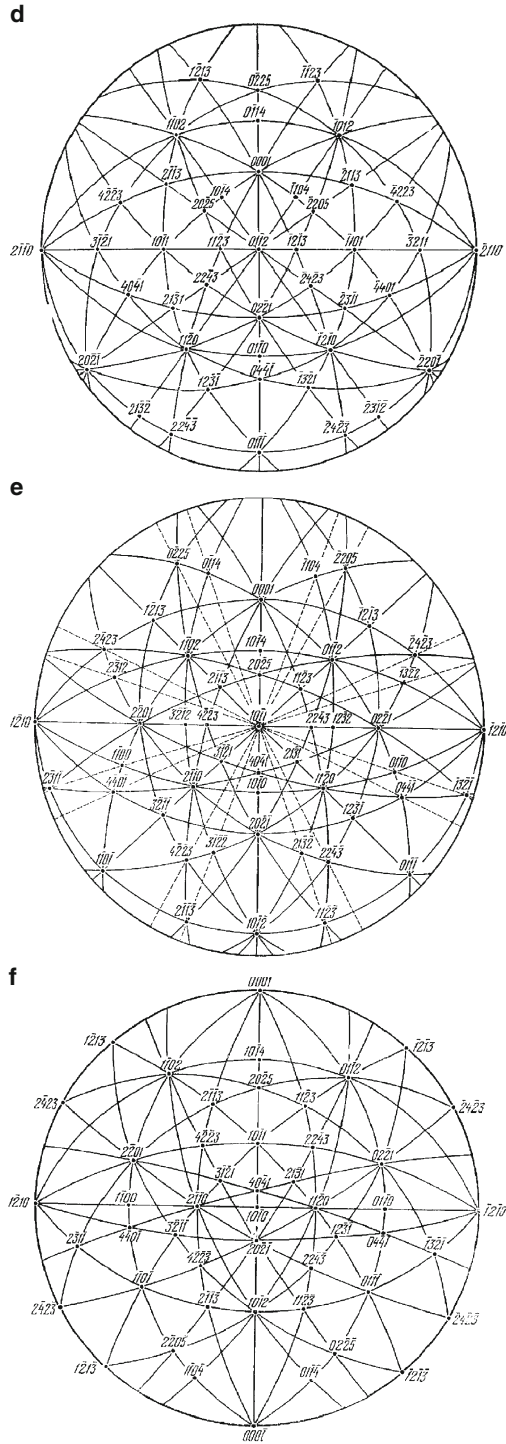
Fig 2.109 (continued)

Fig 2.109   (continued)

Table 2.41 Wulff-Bragg's angles for some planes[a]

Symbol of plane	Interface distance (Å)	Order reflections	Angle (θ)
$\{10\bar{1}1\}$	3,479	1	12°48′
		2	26°17′
$\{01\bar{1}2\}$	2,552	1	17°35′
		2	37°09′
$\{11\bar{2}0\}$	2,379	1	18°54′
		2	40°22′
$\{0001\}$	2,165	3	20°51′
		6	45°26′
$\{02\bar{2}1\}$	1,964	1	26°06′
		2	54°42′
$\{11\bar{2}3\}$	1,601	1	28°46′
$\{21\bar{3}1\}$	1,514	1	30°36′
$\{10\bar{1}4\}$	1,510	1	30°41′
$\{10\bar{1}0\}$	1,374	3	34°07′
$\{20\bar{2}5\}$	1,0988	1	44°31′
$\{22\bar{4}3\}$	1,0426	1	47°40′

[a] Symbols of plane correspond to a morphological elementary cell. The angles are calculated by the interplane distances (Nat.Bat. Standarts US 1959.9.#539). Cu-radiation $K_{\alpha 1}$

θ angles for some planes of rhombohedral sapphire cell, $R\bar{3}c$ Cu-radiation

hkl	θ	I
01·2	12°48′	74
10·4	17°35′	92
X 11·0	18°55′	42
Z 00·6	20°50′	< 1
11·3	21°43′	100
02·4	26°19′	43
11·6	28°47′	81
21·1	29°56′	3
01·8	30°40′	7
21·4	33°19′	32
Y 03·0	34°11′	48

I is the intensity of X-rays passing through the crystal [133]

Table 2.42 Crystallographic planes of sapphire lattice and their spherical coordinates

Usual forms							
		φ	ρ			φ	ρ
c	0001	–	0°00′	k	7.7. $\bar{1}$4.6	30°00′	72°33′
a	11$\bar{2}$0	30°00′	90°00′	υ	44$\bar{8}$3	30°00′	74°38′
m	10$\bar{1}$0	60°00′	90°00′	X	5.5. $\bar{1}$0.3	30°00′	77°36′
s	02$\bar{2}$1	0°00′	72°24′	u	11.11. $\bar{2}\bar{2}$.3	30°00′	78°41′
δ	10$\bar{1}$3	60°00′	27°41′	z	22$\bar{4}$1	30°00′	79°37′
d	10$\bar{1}$2	60°00′	38°12′	λ	7.7.$\bar{1}\bar{4}$.3	30°00′	81°05′
r	10$\bar{1}$1	60°00′	57°36′	υ	8.8.$\bar{1}\bar{6}$.3	30°00′	82°11′
n	22$\bar{4}$3	30°00′	61°13′	E	33$\bar{6}$1	30°00′	83°02′
ξ	7.7.$\bar{1}\bar{4}$.9	30°00′	64°47′	v	44$\bar{8}$1	30°00′	84°46′
w	11$\bar{2}$1	30°00′	69°53′	ω	14.14. $\bar{2}\bar{8}$.3	30°00′	85°31′

rr (10$\bar{1}$1):($\bar{1}$101) = 93°58′	rc (10$\bar{1}$1):(0001) = 57°36′	ra (10$\bar{1}$1):(11$\bar{2}$0) = 43°02′
nn (22$\bar{4}$3):(4$\bar{2}\bar{2}$3) = 51°58′	nc (22$\bar{4}$3):(0001) = 61°13′	rn (10$\bar{1}$1):(22$\bar{4}$3) = 26°00′
zz (22$\bar{4}$1):(4$\bar{2}\bar{2}$1) = 58°55′	zc (22$\bar{4}$1):(0001) = 79°37′	rz (10$\bar{1}$1):(22$\bar{4}$1) = 35°32′

Rare forms					
e 52$\bar{7}$0	p 50$\bar{5}$1	P 05$\bar{5}$1	j 10.10. $\bar{2}$0.3	τ 41$\bar{5}$3	φ 32$\bar{5}$1
f 71$\bar{8}$0	q 70$\bar{7}$1	o 22$\bar{4}$5	ε 11.11. $\bar{2}\bar{2}$.3	ξ 31$\bar{4}$2	T 11.8. $\bar{1}$9.3
γ 10$\bar{1}$5	R 01$\bar{1}$2	π 11$\bar{2}$3	ψ 7.4. $\bar{1}\bar{1}$.9	l 21$\bar{3}$1	χ 2.4.$\bar{6}$.1
x 30$\bar{3}$2	η 01$\bar{1}$2	M 11$\bar{2}$2	ρ 2.8. $\bar{1}$0.9	σ 20.5. $\bar{2}\bar{5}$.9	
α 50$\bar{5}$2	A 05$\bar{5}$2	B 44$\bar{8}$5	D 28.4. $\bar{3}\bar{2}$.27	L 12$\bar{3}$1	
b 70$\bar{7}$2	β 07$\bar{7}$2	Y 10.10. $\bar{2}$0.9	H 16.4. $\bar{2}$0.15	Σ 5.20. $\bar{2}\bar{5}$.9	

The spherical coordinates ρ and φ fix the direction and plane; ρ corresponds to the polar distance from the Wulff net center; φ corresponds to the geographic longitude and is measured from the Wulff net circumference

Table 2.43 Angles between the normals to sapphire facets (planes)

Facet	c 0001	m 10$\bar{1}$0	a 11$\bar{2}$0	q 20$\bar{2}$5	r 10$\bar{1}$1	t 40$\bar{4}$1	01$\bar{1}$2	R 10$\bar{1}$2	02$\bar{2}$1	S 20$\bar{2}$1	p 11$\bar{2}$3	n 22$\bar{4}$3	21$\bar{3}$1 l	31$\bar{2}$1	12$\bar{3}$1
m 10$\bar{1}$0	90,0														
a 11$\bar{2}$0	90,0	30,0													
q 20$\bar{2}$5	32,2	57,8	57,8												
r 10$\bar{1}$1	57,6	32,4	43,0	25,4											
t 40$\bar{4}$1	81,0	9,0	31,2	48,8	23,4										
01$\bar{1}$2	38,2	–	57,6	33,9	47,0	–									
R 10$\bar{1}$2	–	51,8	–	–	84,2	–	–								
02$\bar{2}$1	72,4	–	34,4	59,3	55,6	58,8	34,2	–							
S 20$\bar{2}$1	–	17,6	–	75,4	50,0	–	–	–	–						
p 11$\bar{2}$3	42,3	–	47,7	20,5	27,3	–	19,6	–	38,8	–					
n 22$\bar{4}$3	61,2	–	28,8	–	26,0	–	32,0	–	30,5	–	18,9				
21$\bar{3}$1 l	–	–	17,3	–	25,7	19,2	50,4	–	39,5	–	–	18,4			
31$\bar{2}$1	–	–	–	–	–	–	–	–	–	–	53,0	–	–		
12$\bar{3}$1	–	–	–	–	–	–	–	–	36,4	–	–	–	–	–	
w 11$\bar{2}$1	69,9	–	–	–	–	–	–	–	49,1	–	21,7	42,1	29,9	–	–

Table 2.44 Refractive index in partial transparency region

λ (µm)	T (K)					
	297	1473	1773	1873	1973	2293
0.5	1.774	1.805	1.814	1.817	1.820	1.830
0.75	1.762	1.799	1.802	1.805	1.808	1.818
1.00	1.756	1.785	1.794	1.797	1.800	1.810
1.25	1.751	1.781	1.790	1.793	1.793	1.806
1.50	1.747	1.784	1.787	1.790	1.793	1.803
1.75	1.743	1.777	1.787	1.789	1.792	1.802
2.00	1.738	1.775	1.784	1.787	1.790	1.800
2.25	1.732	1.769	1.778	1.781	1.784	1.794
2.50	1.726	1.761	1.770	1.773	1.776	1.786
2.75	1.718	1.753	1.762	1.765	1.768	1.778
3.00	1.712	1.745	1.754	1.757	1.760	1.770
3.25	1.703	1.738	1.747	1.750	1.753	1.763
3.50	1.696	1.731	1.740	1.743	1.746	1.756
3.75	1.686	1.723	1.732	1.735	1.738	1.748
4.00	1.675	1.715	1.724	1.727	1.730	1.740
4.25	1.664	1.704	1.713	1.716	1.719	1.729
4.50	1.651	1.691	1.700	1.703	1.706	1.716
4.75	1.638	1.680	1.689	1.692	1.695	1.706
5.00	1.624	1.665	1.674	1.677	1.680	1.690
5.25	1.608	1.648	1.657	1.660	1.663	1.673
5.50	1.592	1.627	1.636	1.639	1.642	1.652
5.75	1.566	1.603	1.612	1.615	1.618	1.628
6.00	1.540	1.575	1.584	1.587	1.590	1.600

Refractive index (n_0)

λ (nm)	n_o	λ (nm)	n_o
206.7	1.834	1014.0	1.75547
265.2	1.8336	1033.0	1.755
284	1.82427	1129.0	1.75339
296.7	1.81595	1378.0	1.749
313.0	1.80906	1550.0	1.746
346.6	1.79815	1693.0	1.74368
354.3	1.796	2067.0	1.736
365.0	1.79358	2480.0	1.726
404.7	1.785592	2564.0	1.723
546.0	1.77078	2703.0	1.719
579.1	1.76871	2778.0	1.716
643.9	1.76547	2857.0	1.714
706.5	1.76303	2941.0	1.712
894.4	1.75796	3303.0	1.70231

Sellmeier equation*

$$n_0^2 = 1 + \frac{1.4313493\lambda^2}{\lambda^2 - (0.0726631)^2} + \frac{0.65054713\lambda^2}{\lambda^2 - (0.1193242)^2} + \frac{0.53414021\lambda^2}{\lambda^2 - (18.0228251)^2}$$

$$n_e^2 = 1 + \frac{1.5030759\lambda^2}{\lambda^2 - (0.07402288)^2} + \frac{0.55069141\lambda^2}{\lambda^2 - (0.1216529)^2} + \frac{6.5927379\lambda^2}{\lambda^2 - (20.072248)^2}$$

*Ref [134]

Table 2.45 Refractive index in opaque region

λ (μm)	T (K) 293	T (K) 1773	λ (μm)	T (K) 293	T (K) 1773	λ (μm)	T (K) 293	T (K) 1773
6.2	1.51	1.56	10.5	0.6	1.0	21.5	0.3	2.7
6.4	1.48	1.54	11.0	0.25	0.8	22.0	0.1	2.1
6.6	1.46	1.52	11.5	0.05	0.5	22.7	14.5	1.8
6.8	1.44	1.50	12.0	0.05	0.4	23.0	11,0	2.0
7.0	1.41	1.48	13.0	0.05	0.3	23.5	7.3	2.5
7.2	1.39	1.45	14.0	0.05	0.4	24.0	5.8	3.4
7.4	1.36	1.43	15.0	0.1	0.45	24.5	4.9	4.9
7.6	1.33	1.41	15.5	0.2	0.5	25.0	4.6	5.7
7.8	1.31	1.38	15.9	2.1	0.5	25.5	4.8	5.6
8.0	1.28	1.35	16.2	0.4	0.7	26.0	5.3	5.3
8.2	1.24	1.33	16.5	0.4	0.8	26.3	5.8	5.0
8.4	1.21	1.30	17.0	0.6	1.2	27.0	5.0	4.5
8.6	1.18	1.29	17.5	12.2	1.4	27.5	4.5	4.7
8.8	1.15	1.24	18.0	8.0	2.0	28.0	4.2	5.0
9.0	1.12	1.20	18.5	5.2	3.3	28.5	4.0	5.0
9.2	1.08	1.18	19.0	4.0	5.1	29.0	3.9	4.8
9.4	1.05	1.15	19.2	3.8	5.4	30.0	3.8	4.4
9.6	1.00	1.12	20.0	2.5	4.5	31.0	3.6	4.2
9.8	0.96	1.09	20.5	1.3	3.9	32.0	3.5	4.1
10.0	0.90	1.06	21.0	0.6	3.3	33.0	3.4	4.0

Table 2.46 Absorption coefficient for ruby

Wave	λ (μm)	k_λ (cm^{-1})	λ (μm)	k_λ (cm^{-1})	λ (μm)	k_λ (cm^{-1})
Ordinary	0.555	18,000	0.410	24,400	0.260	38,400
Extraordinary	0.550	18,200	0.400	25,000	0.260	38,400
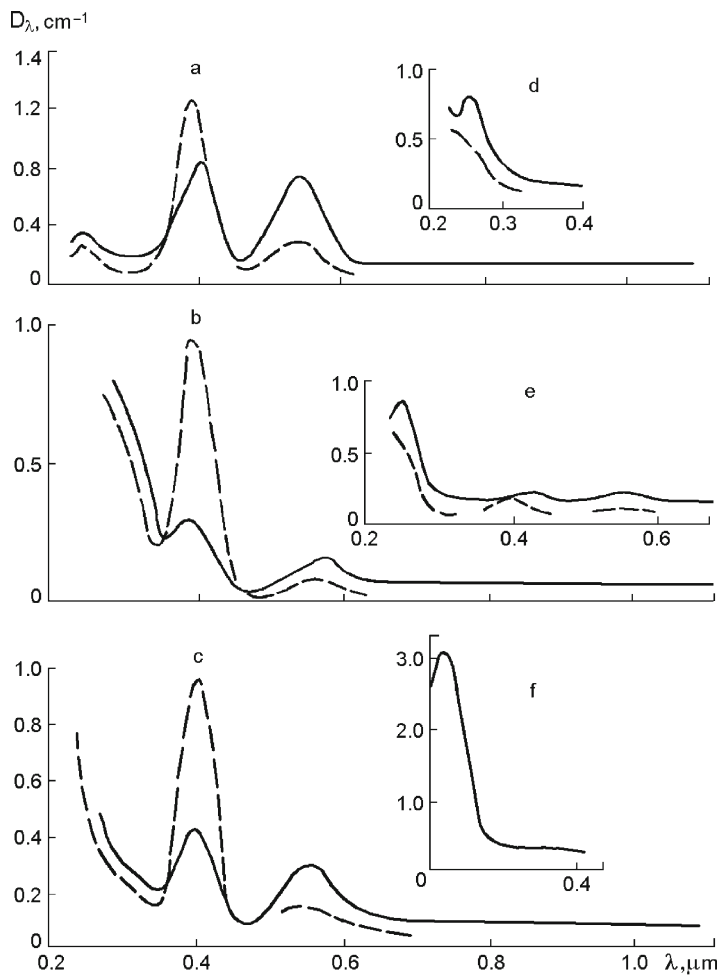
Fig 2.110 Spectral absorption curves for corundum crystals with impurities: (**a**) chromium (ruby); (**b**) vanadium; (**c**) vanadium and chromium; (**d**) iron; (**e**) iron and chromium; (**f**) titanium; (**g**) iron and titanium (blue sapphire); (**h**) cobalt; (**i**) cobalt and chromium; (**j**) nickel; (**k**) manganese; solid lines – ordinary wave, dashed lines – extraordinary wave; in the spectra (**f**) and (**k**) the samples are perpendicular to the optical axis, in the other spectra the samples are parallel to it
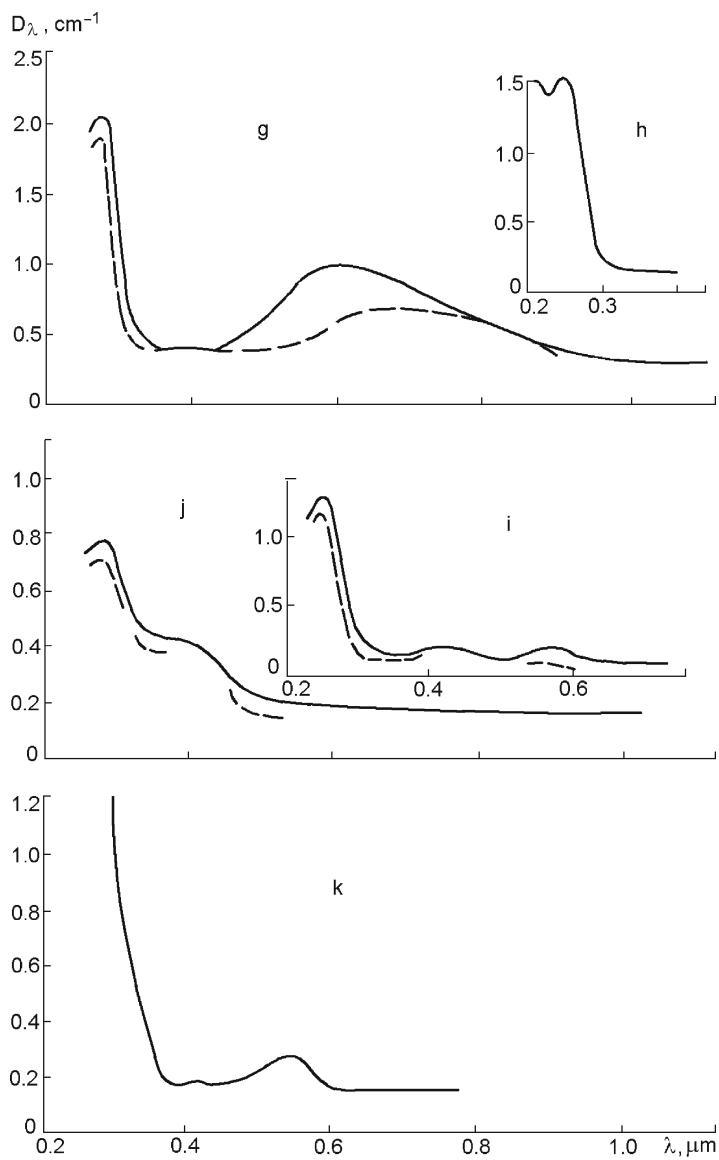
Fig 2.110 (continued)

Table 2.47 Absorption coefficient depending on temperature (cm^{-1})

λ (μm)	T (K)										
	300	500	700	900	1100	1300	1500	1700	1900	2100	2300
1	2	3	4	5	6	7	8	9	10	11	12
0.5	0.0049	0.0069	0.0088	0.012	0.014	0.019	0.024	0.039	0.23	0.34	0.39
0.6	0.0041	0.0061	0.0081	0.010	0.013	0.016	0.022	0.035	0.21	0.31	0.36
0.7	0.0035	0.0055	0.0072	0.0090	0.011	0.014	0.020	0.032	0.19	0.29	0.33
0.8	0.0031	0.0049	0.0065	0.082	0.010	0.013	0.018	0.029	0.18	0.27	0.30
0.9	0.0027	0.0045	0.0061	0.0075	0.0092	0.012	0.016	0.026	0.16	0.24	0.27
1.0	0.0025	0.0041	0.0056	0.0068	0.0083	0.011	0.015	0.024	0.15	0.23	0.25
1.1	0.0024	0.0038	0.0051	0.0063	0.0076	0.0097	0.014	0.022	0.14	0.21	0.23
1.2	0.0022	0.0035	0.0046	0.0058	0.0070	0.0088	0.013	0.020	0.13	0.19	0.22
1.3	0.0021	0.0032	0.0042	0.0054	0.0065	0.0082	0.011	0.018	0.12	0.18	0.20
1,4	0.0020	0.0029	0.0037	0.0050	0.0061	0.0076	0.011	0.017	0.11	0.17	0.19
1.5	0.0019	0.0026	0.0035	0.0046	0.0058	0.0071	0.010	0.016	0.10	0.16	0.18
1.6	0.0018	0.0025	0.0032	0.0042	0.0054	0.0066	0.009	0.015	0.099	0.15	0.17
1.7	0.0018	0.0023	0.0030	0.0039	0.0051	0.0062	0.0085	0.014	0.091	0.14	0.16
1.8	0.0017	0.0022	0.0028	0.0037	0.0047	0.0058	0.0079	0.013	0.086	0.13	0.15
1.9	0.0016	0.0021	0.0027	0.0035	0.0044	0.0056	0.0076	0.012	0.081	0.13	0.14
2.0	0.0016	0.0020	0.0026	0.0033	0.0042	0.0053	0.0074	0.012	0.076	0.12	0.13
2.1	0.0015	0.0019	0.0025	0.0032	0.0039	0.0052	0.0071	0.012	0.071	0.12	0.13
2.2	0.0015	0.0019	0.0024	0.0030	0.0037	0.0050	0.0069	0.012	0.068	0.11	0.12
2.3	0.0015	0.0018	0.0023	0.0030	0.0036	0.0049	0.0069	0.012	0.065	0.11	0.12
2.4	0.0014	0.0018	0.0023	0.0029	0.0035	0.0048	0.0069	0.012	0.064	0.11	0.12
2.5	0.0014	0.0018	0.0023	0.0028	0.0035	0.0048	0.0069	0.012	0.063	0.11	0.12
2.6	0.0014	0.0018	0.0023	0.0028	0.0035	0.0049	0.0070	0.013	0.063	0.11	0.12
2.7	0.0014	0.0018	0.0023	0.0029	0.0036	0.0051	0.0074	0.015	0.064	0.11	0.12
2.8	0.0014	0.0018	0.0024	0.0031	0.0039	0.0055	0.0078	0.017	0.067	0.11	0.12
2.9	0.0014	0.0018	0.0025	0.0033	0.0044	0.0061	0.0087	0.020	0.069	0.12	0.13
3.0	0.0015	0.0019	0.0026	0.0037	0.0050	0.0071	0.010	0.024	0.075	0.12	0.14
3.1	0.0016	0.0021	0.0029	0.0042	0.0061	0.0088	0.014	0.030	0.084	0.13	0.15
3.2	0.0017	0.0022	0.0033	0.0050	0.0082	0.013	0.020	0.040	0.097	0.15	0.17
3.3	0.0019	0.0025	0.0039	0.0067	0.012	0.021	0.034	0.057	0.12	0.17	0.20
3.4	0.0021	0.0030	0.0050	0.0096	0.019	0.036	0.057	0.087	0.15	0.21	0.25
3.5	0.0026	0.0040	0.0076	0.016	0.034	0.062	0.090	0.13	0.20	0.27	0.32
3.6	0.0034	0.0061	0.013	0.028	0.061	0.097	0.14	0.18	0.26	0.37	0.43
3.7	0.0052	0.011	0.024	0.049	0.091	0.14	0.20	0.26	0.36	0.49	0.58
3.8	0.010	0.020	0.046	0.081	0.14	0.20	0.28	0.37	0.52	0.68	0.78
3.9	0.021	0.036	0.064	0.12	0.20	0.29	0.40	0.54	0.70	0.91	1.06
4.0	0.034	0.055	0.094	0.17	0.27	0.39	0.55	0.71	0.95	1.18	1.46
4.1	0.051	0.082	0.13	0.23	0.36	0.52	0.74	0.97	1.24	1.68	1.98
4.2	0.076	0.12	0.18	0.32	0.49	0.71	0.97	1.28	1.63	2.04	2.47
4.3	0.12	0.17	0.26	0.43	0.65	0.97	1.28	1.66	2.10	2.63	3.21
4.4	0.16	0.24	0.36	0.50	0.86	1.30	1.66	2.15	2.67	3.34	4.04

Table 2.47 (continued)

λ (μm)	T (K)										
	300	500	700	900	1100	1300	1500	1700	1900	2100	2300
1	2	3	4	5	6	7	8	9	10	11	12
4.5	0.23	0.32	0.47	0.77	1.17	1.63	2.15	2.75	3.47	4.23	5.09
4.6	0.30	0.43	0.62	0.97	1.42	2.03	2.71	3.52	0.430	5.25	6.36
4.7	0.40	0.53	0.79	1.20	1.76	2.47	3.31	4.30	5.33	6.51	7.94
4.8	0.51	0.68	1.00	1.49	2.19	2.97	4.14	5.25	6.51	7.82	9.70
4.9	0.64	0.86	1.24	1.82	2.67	3.60	4.97	6.31	7.94	9,70	11.50
5.0	0.78	1.06	1.51	2.19	3.19	4.43	5.98	7.47	9.40	11.50	13.8
5.1	0.96	1.30	1.86	2,65	3.86	5.41	7.24	9.12	11.5	13.8	16.8
5.2	1.17	1.57	2.26	3.26	4.64	6.51	8.71	11.0	13.6	16.3	19.8
5.3	1.44	1.96	2.75	3.98	5.67	7.82	10.4	13.1	16.1	19.3	23.3
5.4	1.74	2.44	3.31	4.86	6.81	9.55	12.4	15.6	19.0	22.9	27.1
5.5	2.12	2.97	4.04	5.84	8.58	11.7	14.9	18.6	22.6	27.1	32.1
5.6	2.51	3.55	4.90	7.02	10.3	14.1	17.8	22.2	26.5	31.6	37.4
5.7	2.94	4.23	5.98	8.58	12.0	16.8	21.2	25.9	30.7	36.9	44.0
5.8	3.41	4.93	7.36	10.3	14.2	20.3	25.1	30.7	35.7	43.0	50.5
5.9	3.86	6.03	8.84	12.4	17.1	24.0	30.2	36.0	42.3	50.1	58.4
6.0	4.79	7.82	11.1	16.3	21.9	28.4	35.2	42.3	50.1	58.4	67.1
6.1	6.81	9.77	13.4	19.9	26.3	33.6	41.4	49.7	57.5	66.6	77.6
6.2	9.62	12.0	16.6	24.2	31.6	39.8	47.9	57.5	66.1	75.9	87.8
6.3	12.6	15.4	20.6	29.3	37.7	47.1	55.8	66.1	75.9	87.1	100
6.4	16.3	19.6	25.9	34.7	44.7	54.9	65.1	75.9	87.1	98.5	112
6.5	20.4	24.4	31.1	41.1	52.5	63.1	75.3	87.8	100	113	123
6.6	25.1	30.2	38.0	48.6	60.7	73.0	87.1	100	113	128	142
6.7	30.4	35.8	44.7	56.7	70.2	83.2	99.2	114	128	142	158
6.8	36.3	43.0	52.5	65.1	80.7	94.0	113	130	144	160	176
6.9	43.0	50.9	62.1	74.7	92.6	108	128	144	161	179	196
7.0	50.1	61.2	73.6	85.8	105	124	142	161	181	199	219

Table 2.48 Elastic constants

Rigidity, $c_{ij} \cdot 10^{10}$ Pa	Compliance, $S_{ij} \cdot 10^{-11}$ Pa^{-1}
$c_{11} = 49.68$	$S_{11} = 0.2353$
$c_{33} = 49.81$	$S_{33} = 0.2170$
$c_{44} = 14.74$	$S_{44} = 0.6940$
$c_{12} = 16.36$	$S_{12} = 0.0716$
$c_{13} = 11.09$	$S_{13} = 0.0364$
$c_{14} = 2.35$	$S_{14} = 0.489$

Table 2.49   Temperature dependence of compliance (×10⁻¹¹ Pa⁻¹)

T (K)	S_{11}	S_{33}	S_{44}	S_{12}	S_{13}	S_{14}
0	0.2326	0.2151	0.6765	−0.0693	−0.0362	0.0465
373	0.2326	0.2152	0.6776	−0.0695	−0.0363	0.0467
423	0.2330	0.2154	0.6802	−0.0698	−0.0364	0.0471
473	0.2336	0.2158	0.6841	−0.0704	−0.0365	0.0477
523	0.2344	0.2163	0.6889	−0.0710	−0.0366	0.0483
573	0.2353	0.2169	0.6942	−0.0716	−0.0368	0.0491
623	0.2364	0.2176	0.700	−0.0723	−0.0369	0.0500
673	0.2375	0.2183	0.7061	−0.0731	−0.0370	0.0509
723	0.2386	0.2191	0.7126	−0.0740	−0.0370	0.0519
773	0.2399	0.2200	0.7193	−0.0748	−0.0371	0.0530
823	0.2412	0.2209	0.7263	−0.0757	−0.0372	0.0541
873	0.2425	0.2218	0.7334	−0.0766	−0.0372	0.0552
923	0.2438	0.2228	0.7407	−0.0775	−0.0373	0.0564
973	0.2453	0.2237	0.7482	−0.0784	−0.0373	0.0576
1023	0.2467	0.2247	0.7559	−0.0796	−0.0374	0.0587
1073	0.2482	0.2258	0.7638	−0.0808	−0.0374	0.0600
1123	0.2497	0.2268	0.7719	−0.0820	−0.0374	0.0613
1173	0.2512	0.2279	0.7803	−0,0832	−0.0375	0.0626

Table 2.50   Accurate values of relative elongation and differential temperature coefficient of linear expansion (α)

T (K)	Relative elongation, $dL/L \cdot 10^6$	$\alpha = dL/L$ $\cdot 10^6$ K⁻¹	T (K)	Relative elongation, $dL/L \cdot 10^6$	$\alpha = dL/L$ $\cdot 10^6$ K⁻¹
93	−622.162	0.283	573	1887.723	7.752
73	−492.952	2.795	673	2684.375	8.159
273	−99.998	4.911	773	3516.39	8.470
293	0	5.234	1073	6172.19	9.217
373	464.467	6.279	1273	8062.719	9.686
473	1139.9	7.166	1773	13185.68	10.806

Table 2.51   Temperature dependence of $\lambda_T(T)$ for ruby (W/m K)

T (K)	λ_T	T (K)	λ_T	T (K)	λ_T	T (K)	λ_T	T (K)	λ_T
5.0	170	28.0	920	50	850	100	140	205	108
6.0	206	30.8	950	51.6	700	102	130	209	120
6.6	303	31.0	970	51.7	680	108	120	210	109
7.2	295	34.0	990	55.4	515	116	110	215	130
7.3	299	35.0	1020	55	500	130	130	220	110
8.4	207	35.0	1070	57	450	138	120	225	100
9.0	200	38.4	1050	60.8	308	144	120	230	105
9.1	300	40.8	1060	63	300	150	120	235	210
9.2	350	41.0	1180	64	310	158	110	240	105

(continued)

Table 2.51 (continued)

T (K)	λ_T	T (K)	λ_T	T (K)	λ_T	T (K)	λ_T	T (K)	λ_T
9.2	360	42.4	1090	66.3	260	162	120	248	102
9.8	425	43.8	1130	70.0	250	167	120	251	105
10.4	258	44.8	1130	75	200	171	115	255	110
12.0	443	47.4	1140	76	190	173	110	261	110
14.4	625	47.6	1110	77	190	180	110	268	100
14.5	520	48.4	1060	80	170	184	110	274	120
14.9	540	48.5	1100	82.0	163	187	120	278	100
16.6	625	49.7	845	83	154	190	105	255	100
18.9	750	51.6	700	85	160	192	100	290	100
19.0	780	50	1100	86	130	195	110	295	95
25.0	880	50	1050	90	150	197	120	300	85
25.0	940	50	900	95	140	201	111		

Table 2.52 Temperature dependence of specific heat c_p (J/kg/K)

T (K)	c_p	T (K)	c_p	T (K)	c_p
5.0	0.2	38.8	7.67	40.1	16.5
9.0	0.5	30.0	8.31	43.4	16.5
18.3	2.37	33.0	9.00	46.6	20.87
21.0	3.18	36.8	9.84	49.3	24.66
26.7	4.96	38.8	11.79	51.5	29.20
53.9	32.3	133.0	290.0	216.0	725.0
56.6	39.41	136.0	310.0	223.0	740.0
58.7	49.95	140.0	325.0	226.0	745.0
59.8	42.31	145.0	350.0	231.0	750.0
61.0	45.81	147.0	375.0	233.0	760.0
65.1	50.85	152.0	413.0	237.0	770.0
70.2	60.74	156.0	425.0	243.0	780.0
73.8	65.82	165.0	475.0	247.0	778.0
80.0	98.0	167.0	500.0	253.0	790.0
88.0	100.0	170.0	510.0	260.0	800.0
90.5	110.7	175.0	540.0	263.0	810.0
97.5	130.0	177.0	560.0	267.0	810.0
98.0	134.0	180.0	575.0	269.0	810.0
100.0	145.0	185.0	600.0	272.0	815.0
105.0	164.0	187.0	610.0	276.0	820.0
108.0	170.0	192.0	640.0	278.0	825.0
115.0	200.0	195.0	684.0	284.0	830.0
120.0	225.0	200.0	675.0	286.0	840.0
123,0	240.0	203.0	680.0	290.0	845.0
128.0	255.0	205.0	690.0	295.0	850.0
130.0	275.0	212.0	710.0	298.0	842.0

Table 2.53 Temperature dependence of sound absorption in ruby k_λ at 9,400 MHz frequency (db/cm)

T (K)	k_λ	T (K)	k_λ	T (K)	k_λ
4.2	0	90	0.3	152	10.5
10	0.1	95	3.6	163	11.4
15	0.1	98	3.8	166	11.4
17	0.15	100	4.8	167	11.8
22	0.16	101	4.5	170	12.0
30	0.3	105	4.5	177	12.5
34	0.25	107	5.2	180	12.07
37	0.45	110	5.5	185	13.0
40	0.5	112	6.0	190	13.4
50	0.7	115	6.2	192	13.5
55	0.75	117	6.4	200	13.8
58	0.8	118	6,7	205	14.0
60	0.9	120	7.0	210	14.2
63	1.0	124	7.4	220	14.4
65	1.0	125	7.7	222	14.5
70	1.5	126	7.6	225	14.7
71	1.3	127	8.0	230	14.5
73	1.5	130	8.2	335	14.7
78	1.8	130	7.8	240	14.7
80	2.2	132	8.2	250	14.8
81	2.2	140	9.5	252	14.8
85	2.5	144	9.5	253	15.0
87	2.7	150	10.5	270	15.0
				300	15.3

Table 2.54 Thermodynamic properties

	$H_T - H_{298}$		S_T		ΔH_T		ΔF_T	
T (K)	kJ/mol	kcal/mol	kJ/mol K	kcal/mol K	kJ/mol	kcal/mol	kJ/mol	kcal/mol
298	–	–	50.91	12.16	−1,676,000	−400,300	−1,583,000	−378,000
400	9,211	2,200	77.38	18.48	−1,676,500	−400,400	−1,550,000	−370,000
500	19,260	4,600	99.78	23.83	−1,676,000	−400,300	−1,519,000	−362,800
600	30,230	7,220	119.7	28.60	−1,675,600	−400,200	−1,488,000	−355,300
700	41,830	9,990	137.6	32.86	−1,674,400	−399,900	−1,456,000	−347,800
800	53,760	12,840	153.5	36.67	−1,673,500	−399,700	−1,425,000	−340,400
900	65,940	15,750	167.8	40.08	−1,672,700	−399,500	−1,394,000	−332,900
1000	78,340	18,710	181.0	43.22	−1,693,200	−404,400	−1,362,000	−325,209
1100	90,900	21,710	192.9	46.07	−1,691,500	−404,000	−1,328,000	−317,200
1200	103,600	24,740	203.9	48.71	−1,690,000	−403,600	−1,298,000	−309,400
1300	116,400	27,790	214.2	51.15	−1,688,000	−403,200	−1,262,000	−301,500
1400	129,200	30,850	223.7	53.42	−168,600	−402,800	−1,230,000	−293,500
1500	142,000	33,920	232.5	55.54	−168,500	−402,500	−1,198,000	−286,100
1600	154,900	37,000	240.8	57.52	−163,600	−402,000	−1,164,000	−278,100
1700	167,900	40,090	248.7	59.39	−162,600	−401,700	−1,133,000	−270,600
1800	180,800	43,190	256.1	61.17	−1,680,000	−401,300	−1,102,000	−263,100

Table 2.55 Thermodynamic properties at low temperatures

	c_p		S_T		$H - H_0$		$(H - H_0)/T$		$-(F - H_0)/T$	
T (K)	kJ/ kmol K	kcal/ mol K	kJ/ kmol K	kcal/ mol K	kJ/ kmol K	kcal/ mol	kJ/ kmol K	kcal/ mol K	kJ/ kmol K	kcal/ mol K
17	0.067	0.016	0.017	0.0041	0.218	0.052	0.013	0.0031	0.004	0.0010
25	0.163	0.039	0.056	0.0133	1.063	0.254	0.043	0.0102	0.013	0.0031
50	1.465	0.350	0.457	0.1092	1.734	4.142	0.347	0.0828	0.110	0.0264
75	5.686	1.358	1.721	0.411	98.82	23.601	1.318	0.147	0.404	0.0964
100	12.88	3.075	4.279	1.022	325.4	77.705	3.253	0.7770	1.025	0.2448
125	21.96	5.245	8.093	1.933	757.3	180.86	6.058	1.4469	2.037	0.4865
150	31.99	7.640	12.98	3.100	1431.0	341.74	9.539	2.2783	3.440	0.8217
175	42.03	10.038	18.66	4.457	2398.0	572.62	13.70	3.2721	4.961	1.1848
200	51.25	12.240	24.88	5.943	3524.0	841.55	17.22	4.2078	7.267	1.7356
225	59.45	14.198	31.40	7.500	4909.0	1172.5	21.82	5.2110	9.584	2.2891
250	66,95	15.990	38.06	9.089	6489.0	1549.9	25.96	6.1997	12.10	2.8895
275	74,04	17.683	44.78	10.694	8253.0	1971.2	30.01	7.1680	14.76	3.5260
298	79,92	19.089	50.94	12.165	1003.0	2396,4	33.65	8.0373	17.28	4.1276
300	80,35	19.190	51.50	12.299	1018.0	2432,6	33.95	8.1087	17.54	4.1900

Table 2.56 Enthalpy $H_T - H_{273}$ of aluminum oxide

Temperature (K)	$H_T - H_{273}$	Temperature (K)	$H_T - H_{273}$
400	81.98/19.58	1,400	1,251/298.80
500	178.70/42.67	1,500	1,379.00/329.80
600	284.70/68.00	1,600	1,505.00/360.00
700	396.40/94.68	1,700	1,638.00/391.10
800	512.00/122.28	1,800	1,769.00/422.40
900	631.00/150.62	1,900	1,901.00/454.10
1,000	752.00/179.56	2,000	2,035.00/486.00
1,100	875.00/208.96	2,100	2,170.00/518.20
1,200	1,000.00/238.75	2,200	2,305.00/583.20

Table 2.57 Physical properties

Mechanical properties	Density	3.97–3.99 g/cm^3
	Hardness	
	Mohs	9
	Knoop	$\parallel$C 1525–1,800 kg/mm^2; $\perp$ C 1900–2,100 kg/mm^2
	Vickers (9.8N)	$\parallel$C 16–17 GPa; $\perp$ C 18–20 GPa
	Young's modulus	345–494 GPa (most often used values are 345–470 GPa)
	Tensile strength	298 K, 400 MPa
		770 K, 275 MPa
		1,000 K, 335 MPa
	Compressive strength	2–2.9 GPa
	(Balk modulus)	
	Flexural strength	$\parallel$C 1.03 GPa; $\perp$ C 1.54 GPa
	Compression modulus	250 GPa
	Rigidity modulus	145–175 GPa
	Rupture modulus (MOR)	350–690 MPa
	Elasticity modulus	$3.6 \cdot 105$ N/mm^2
	Poisson's ratio	0.27–0.30
	Jet abrasion resistance (acc. to Mackensen)	0.12 mm

Thermal characteristics	Melting point	2,323 K (2050 °C)	
	Boiling point	3,253 K (2980 °C)	
	Thermal expansion coefficient ($\times 10^{-6}$ K^{-1})	293–323 K $\parallel$C 6.6	$\perp$ C 5.0
		310–670 K $\parallel$C 7.0	$\perp$ C 7.7
		1,270 K $\parallel$C 9.03	$\perp$ C 8.31
		60° to C-axis:	
		293–323 K 5.8	
		1,270 K 8.4	
		1,770 K 9.0	
	Thermal conductivity	30 K 10,000 W/m K	
		298 K $\parallel$C 32.5 W/m K	$\perp$ C 30.3 W/m K
		670 K 12.56 W/m K	
		1,500 K 4 W/m K	
	Specific heat	19 mK 159 pJ/K	
		12 mK 41.7 pJ/K	
		9 mK 16.1 pJ/K	
		293 K 181–187 cal/g K	
		1,273 K 0.300 cal/g K	

Electrical characteristics	Resistivity	293 K $\parallel$C $(1.2–2.9) \cdot 10^{19}$ Ω cm, $\perp$ C $5 \cdot 10^{18}$ Ω cm	
		573 K 10^{11} Ω cm	
		1,270 K 10^{9} Ω cm	
		1,770 K 10^{5} Ω cm	
		2,270 K 10^{3} Ω cm	
	Dielectric constant	293 K (20°C) $\perp$ C 9.35	$\parallel$C 11.53
		370 K $\perp$ C 9.43	$\parallel$C 11.66
		570 K $\perp$ C 9.66	$\parallel$C 12.07
		770 K $\perp$ C 9.92	$\parallel$C 12.54
		970 K $\perp$ C 10.26	$\parallel$C 13.18
		293 K, $10^{3}–10^{9}$ Hz $\parallel$C 11.5	$\perp$ C 9.3
	Dielectric tangent loss	293 K, 10^{10} Hz $\parallel$C $8.6 \cdot 10^{-5}$	$\perp$ C $3.0 \cdot 10^{-5}$
	Dielectric strength	48×10^{6} V/m	